

GEOLOGY, MINERALIZATION, ALTERATION, AND STRUCTURAL EVOLUTION OF
THE ZAOZIGOU AU-SB DEPOSIT, WEST QINLING OROGEN, CHINA

by

Duncan C. McIntire

Copyright by Duncan C. McIntire 2021

All Rights Reserved

A thesis submitted to the Faculty and Board of Trustees of the Colorado School of Mines in partial fulfillment of the requirements for the degree of Master of Science (Geology).

Golden, Colorado

Date _____

Signed: _____

Duncan C. McIntire

Signed: _____

Dr. Richard Goldfarb
Thesis Advisor

Golden, Colorado

Date _____

Signed: _____

Dr. Wendy Bohrson
Professor and Head
Department of Geology and Geological Engineering

ABSTRACT

The world-class Zaozigou Au-Sb deposit is the largest gold deposit in the West Qinling Orogen. Despite an endowment of nearly 3.8 Moz Au and 0.12 Mt Sb, the geological context of the Zaozigou deposit has not been comprehensively studied or described. New surface and underground mapping of geology, structure, alteration, and mineralization presented here establishes a geological framework with which to evaluate the Zaozigou deposit.

The structural evolution of the Zaozigou deposit followed a progressive evolution and rotation of regional stresses related to multiple stages of accretion and ocean-closing within the Qinling Orogen. The tectonic regime at Zaozigou likely initiated as NE-SW compression which developed a fold-and-thrust belt with an axial plane striking roughly 330° . Coincident with the development of the fold-and-thrust belt, fault surface lineations indicate the formation of NE-SW right-lateral strike-slip faults. Many faults and joints of this orientation were sites of emplacement of Triassic porphyry dikes of quartz dacite to diorite composition. The dikes caused extensive contact metamorphism of the surrounding Permian to Triassic clastic sediments of the Gulangdi Formation, thus converting local interbedded flysch carbonate-siltstone meta-sediments to an interbedded marble-hornfels together referred to as slate hornfels. The relative strength of the slate hornfels likely increased the overall competency of the rocks at Zaozigou, allowing for the buildup of higher pore fluid pressures. Pore fluid pressures overcame the strength of the rock package causing fault ruptures as high-angle reverse faults and low-angle extensional veins. Fault-valve fluid pressure cycling is interpreted to continue over an extended period while the dynamic tectonic evolution of the West Qinling Orogen caused a counterclockwise rotation of the principal stress axis. Late-stage faulting crosscuts mineralization and moderately dismembers the deposit.

Two main orientations of ore-hosting faults are present at Zaozigou. 1) High angle reverse fault-hosted orebodies are labelled using the “Au” prefix. 2) Low angle fault-hosted extensional vein orebodies are labelled using the “M” prefix. The “Au” orebodies are typified by the Au1 and Au9 orebodies, which trend NE-SW. Field relationships suggest they initiated as right lateral strike slip faults and were reactivated as high angle reverse faults which host multiple generations of cataclastically deformed quartz-stibnite veins, fault gouge, and frictional breccias. “M” orebodies are typified by the M4, M6, M7, and M9 orebodies, which are low angle laminated quartz-stibnite extensional veins. “Au” and “M” orebodies have broad sericitic alteration haloes which host disseminated auriferous arsenopyrite and pyrite. The quartz-stibnite fault-fill and extensional are high grade orebodies up to 56521 ppb Au. Sericite-pyrite-arsenopyrite mineralization precipitated through sericitization of host rocks, and sulfidation of Fe-rich phases. Wall rock hosted disseminated ore is of lower grade, averaging 2936 ppb Au in altered slate hornfels and averaging 4420 ppb Au in altered quartz dacite porphyry dikes. Hydrothermal alteration follows a spatial zonation pattern identified through SWIR from most proximal NH₄-illite, to distal illite-chlorite alteration. NH₄-illite was only identified in samples taken within the most proximal 10m sericitic alteration haloes around both “Au” and “M” orebodies. Stibnite micro-inclusions observed within wall rock disseminated arsenopyrite crystals indicate that stibnite and arsenopyrite precipitated from a common ore fluid.

TABLE OF CONTENTS

ABSTRACT.....	iii
LIST OF FIGURES	viii
LIST OF TABLES.....	xii
ACKNOWLEDGEMENTS.....	xiii
CHAPTER 1	1
1.1 Introduction.....	1
1.2 Analytical Methods.....	5
1.3 Regional Setting.....	8
1.4 Local Geology.....	13
1.5 Lithologies at Zaozigou	18
1.5.1 Slate Hornfels.....	21
1.5.2 Quartz Dacite Porphyry	25
1.5.3 Diorite Porphyry	26
1.6 Metamorphism at the Zaozigou gold deposit	28
1.7 Structural Evolution of the Zaozigou gold deposit.....	30
1.7.1 Early Folding and faulting (1).....	33
1.7.2 Contact metamorphism (2)	35
1.7.3 Development of main ore-bearing fault generations (3) and protracted cyclical development of faults and veins (4)	36
1.7.4 Late crosscutting faults (5).....	41

1.8	Mineral Grain Deformation	42
1.8.1	Stibnite deformation.....	42
1.8.2	Quartz deformation	48
1.9	Hydrothermal Alteration.....	50
1.9.1	Hydrothermal alteration of slate hornfels	52
1.9.2	Hydrothermal alteration of quartz dacite porphyry	58
1.10	Bulk Rock Geochemistry	63
1.10.1	Elemental Correlations	69
1.11	Ore Mineralization	70
1.11.1	Quartz-stibnite vein mineralization.....	73
1.11.2	Dolomite-ankerite-calcite low sulfide lode-style vein mineralization	78
1.11.3	Cataclastic vein brecciation mineralization	79
1.11.4	Slate hornfels-hosted disseminated sulfide wall rock alteration mineralization	80
1.11.5	Quartz dacite porphyry-hosted disseminated sulfide wall rock alteration mineralization	83
1.12	Discussion.....	89
1.12.1	Role of contact metamorphism	89
1.12.2	Peak metamorphism of host rocks at Zaozigou	90
1.12.2	Structural evolution of Zaozigou in the context of the West Qinling Orogen	91
1.12.3	Discussion of bimodal model for ore mineral precipitation	94

1.12.4	Ammonium illite as a product of hydrothermal alteration.....	97
1.12.5	An orogenic gold deposit?	99
1.13	Conclusions.....	101
1.14	Recommendations for future work	103
REFERENCES	105
APPENDIX A	SUMMARY TABLE OF SIGNIFICANT GLOBAL AU-SB DEPOSITS..	111
APPENDIX B	SUPPLEMENTAL FILES.....	113
APPENDIX C	STIBNITE SOLUBILITY AND AQUEOUS SPECIATION	114
APPENDIX D	STRUCTURAL CROSS SECTIONS	120
APPENDIX E	ANALYTICAL METHODS	124

LIST OF FIGURES

Figure 1.1	Tectonic position of Zaozigou in the context of the Qinling Orogen.	7
Figure 1.2	N-S cross sections of the Qinling Orogen showing the tectonic evolution of the orogen through geologic time.	10
Figure 1.3	Regional geological map of the Xiahe-Hezuo mineralized zone in the context of the West Qinling Orogen.	11
Figure 1.4	Schematic diagram of the Au1 fault-hosted ore body.	15
Figure 1.5	Schematic diagram of the M4 orebody.	17
Figure 1.6	Map of the surface geology of Zaozigou.	18
Figure 1.7	Discrimination plots for terrigenous sedimentary rocks.	23
Figure 1.8	Outcrops of Gulangdi slate.	24
Figure 1.9	Photographs and photomicrograph of quartz dacite porphyry from Zaozigou.	26
Figure 1.10	Photo and photomicrograph of diorite dike.	27
Figure 1.11	Diorite and quartz dacite porphyry dikes cross cut by mineralized quartz-stibnite veins.	28
Figure 1.12	Metamorphic reactions in host rocks at Zaozigou.	29
Figure 1.13	Stereographic projections of major ore-hosting reverse faults.	33
Figure 1.14	Schematic diagram describing steep reverse fault-related drag folds.	34
Figure 1.15	A pre-ore reverse drag fold preserved in slate hornfels.	35
Figure 1.16	Stress-strain diagram indicating conditions for elastic, plastic, and brittle deformation of slate and hornfels.	37
Figure 1.17	Multiple generations of extensional quartz-stibnite vein produced in “M” style orebodies.	39

Figure 1.18	Schematic outcrop of the Au1 fault zone observed at locations 26, 115	40
Figure 1.19	Fault-delineated oxide horizon	44
Figure 1.20	Photomicrographs of deformed stibnite found within quartz-stibnite veins...	46
Figure 1.21	Plane polarized and cross polarized photomicrographs of quartz crystals	49
Figure 1.22	Stacked SWIR reflectance spectra	51
Figure 1.23	Peak position of al-oh absorption bands measured in illites and NH ₄ -illites .	53
Figure 1.24	Al-OH (2200 nm) absorption peak positions.....	54
Figure 1.25	Quartz-sulfide selvage mantling a quartz-stibnite vein.	55
Figure 1.26	Spatial plots of dominant and secondary alteration minerals identified by SWIR.....	56
Figure 1.27	Histogram of alteration-related minerals in slate hornfels samples	57
Figure 1.28	Arsenopyrite replacement of biotite in quartz dacite	59
Figure 1.29	Histogram of alteration-related minerals in quartz dacite samples.....	60
Figure 1.30	Spatial variation of hydrothermal minerals identified through SWIR.....	61
Figure 1.31	QEMSCAN mineral maps of two vein and disseminated mineralization hosting samples.....	72
Figure 1.32	Typical quartz-stibnite veinlets.....	73
Figure 1.33	FE-SEM scans of sample ZZG18-056.....	74
Figure 1.34	SEM/EDS scans of sample ZZG18-041.	75
Figure 1.35	The Au9 dolomite lode vein.	78
Figure 1.36	Sample photos of ZZG18-070	81
Figure 1.37	Thin section photomicrographs of hydrothermally altered slate hornfels	83

Figure 1.38	Grade-distance diagram.	84
Figure 1.39	Photomicrograph and electron microscope scans of sample ZZG18-056	85
Figure 1.40	Photomicrographs of iron sulfides replacing biotite along cleavage planes..	86
Figure 1.41	Representative ore sample photographs from Zaozigou.....	87
Figure 1.42	Schematic diagram of the relationship between “Au” and “M” style orebodies at Zaozigou in a fault-valve model.....	93
Figure C.1	Phase diagram of aqueous Sb species in hydrothermal fluids	119
Figure D.1	Cross section A-A’.....	120
Figure D.2	Cross section B-B’	121
Figure D.3	Cross section D-D’	122
Figure D.4	Cross section G-G’	123
Figure E.1	Observable gold grains in hand-panned high-grade Au-Sb ore.....	129

LIST OF TABLES

Table 1.1	Major and trace element concentrations from surface and underground transects at Zaozigou	64
Table 1.2	Pearson correlation coefficients of bulk rock geochemistry values of common Au-associated elements	70
Table 1.3	Summary chart of main ore style characteristics at Zaozigou Au-Sb deposit	71
Table A.1	Summary table of significant global Au-Sb deposits.....	111

ACKNOWLEDGEMENTS

Many thanks are due to many people. I would first like to recognize the mentorship, friendliness, and patience of my advisor, Prof. Richard Goldfarb. Thank you and Mary for giving me the opportunity to take care of Charlee and Henry. A sincere thank you to my advisory committee members. Thank you, Prof. Zhaoshan Chang, for your assistance in the field and in the interpretation of SWIR spectra, and thank you and Joy for hosting so many dinners at your house. Thank you, Dr. Elizabeth Holley, for your input on the contents of this thesis and for being a kind and engaging teacher.

I would like to thank my colleagues at the Chinese University of Geosciences in Beijing. Thanks to Kunfeng Qiu for formulating this project, and for all the help at every stage of the project. Thanks to Haocheng Yu and Zongyang Gou for their assistance and friendship during fieldwork and afterwards. Zhiming Yang is thanked for lending the use of the ASD Terraspec utilized during this project.

I would like to thank Dr. Katharina Pfaff for her knowledge, guidance, training, and patience with me while using the FE-SEM and QEMSCAN. I would also like to thank Jae Erickson for preparing the thin sections used in this thesis, and for giving me an amazing job in the thin section lab.

I would like to thank all my fellow classmates who I met during my extended tenure at CSM. I thank the Banquet Breakfast Club, SEG student chapter, Pokemon Go pals, Wisconsinites, GSA Portland, ME 2019, BE225, Natasha Galvez & George Dunne, Kyle, Lexi, and Lissa Hameister.

I would lastly like to thank my family for being unconditionally supportive of me over the past 4 years. An enormous thank you to my beautiful wife, YingJie Liu, for constantly

pushing me to be a better version of myself, for not accepting my excuses, and for believing in me at times where it was difficult to believe in myself.

This research was financially supported by the National Natural Science Foundation of China (41702069), and the Fundamental Research Funds for the Central Universities China (292018125, 292018141).

CHAPTER 1
GEOLOGY, MINERALIZATION, ALTERATION, AND STRUCTURAL EVOLUTION OF
THE ZAOZIGOU AU-SB DEPOSIT, WEST QINLING OROGEN, CHINA

Duncan C. McIntire

1.1 Introduction

The Zaozigou Au-Sb deposit is one of the largest deposits in the West Qinling Orogen, with a gold endowment variably reported as 142 tons at an average grade of 2.69 g/t (Chen et al., 2011), or 118 tons Au at an average grade of 3.42 g/t and >0.12 Mt Sb averaging 0.99% Sb (Liang et al., 2016). Most ore at the deposit is hosted by contact metamorphosed interbedded siltstone-carbonate sandstones and a series of Triassic quartz dacite porphyry dikes. Gold is hosted by fault bound quartz-stibnite±carbonate veins, veinlets, and their associated phyllic alteration haloes that are typified by ore mineral assemblages of disseminated (arsenian) pyrite and arsenopyrite. The most important ore minerals are stibnite, arsenopyrite, and pyrite.

Zaozigou was first discovered and mined by open-pit as an oxide gold deposit. Due to environmental reasons and the discovery of higher-grade lode veins, the operation went underground, and the pit was reclaimed (mine geologist Rui Zhu, personal communication, 2018). English language literature describing the mine prior to underground operations is lacking. At the time of the current investigation, the Zaozigou gold mine comprised 13 underground levels accessed by three separate lifts and an access decline used by light and heavy vehicles. The previously mined open pit had already been reclaimed by soil infilling, mulching, and seeding. Very little surface disturbance was noted, with unfettered access given to local nomadic Tibetan tribes of the Gannan Autonomous Prefecture. In the underground mine,

orebodies are accessed by variations on standard room and pillar, and open stoping mining methods. The tunnels in the mine are navigated by electric ore carts.

The deposit style and ore fluid source at Zaozigou has been classified in the literature under various genetic models. Early work describes the mineralization at Zaozigou to be Carlin-like, based on bulk geochemistry, host rock and mineral assemblages, and the early identification of invisible gold within disseminated fine grained arsenopyrite and (arsenian) pyrite (Sanogo et al., 2008; Liu et al., 2011; Cao et al., 2012). Zaozigou was recently classified as a Carlin-style gold deposit by Du et al. (2021) based on $\delta^{34}\text{S}$ isotopes and trace elemental composition of auriferous pyrite grains. Magmatic-hydrothermal models have also been proposed; however, there is little definitive supporting evidence. Researchers proposed a porphyry model based on interpretation of hydrogen and oxygen isotope values of granodiorite-hosted quartz, porphyritic dike textures, and U-Pb ages of diorite dikes emplaced at ca. 215.5 ± 2.1 Ma, 216.6 ± 2.4 Ma (Liu et al., 2012). Arguments for an epithermal model suggest that fluid mixing of a post-magmatic hydrothermal fluid with meteoric water was a trigger for ore mineralization (Jiang et al., 2010), while Tang et al. (2019) calculate ore formation temperatures in the range of 148-304°C based on the Au content in arsenopyrite, and they suggest that fluid inclusions and C-H-O isotopes indicate an epithermal environment. Sui et al. (2018; 2020) argue that Zaozigou should be classified as a reduced intrusion related gold system (RIRGS) based on an interpretation of local granodiorite dikes as causative intrusions. They indicate that these dikes are ilmenite-series. They analyzed U-Pb ages of granodiorite and late diorite dikes at 248.9 ± 1.4 Ma to 244.8 ± 1.4 Ma and 237.5 ± 1.4 Ma, respectively. These dates are taken to bracket the age of Au mineralization at Zaozigou based on field relationships. $^{40}\text{Ar}/^{39}\text{Ar}$ dates of sericite separates were also calculated to suggest a plateau age of 245.6 ± 1.0 Ma to 242.1 ± 1.0 Ma age of hydrothermal mineralization.

These dates are roughly coeval with formation ages of nearby Au-Cu skarns in the eastern zone of the Xiahe-Hezuo district, notably the Dewulu skarn, which is situated roughly 50 km to the northeast of Zaozigou. Sui et al. 2018 argue that the similar ages between igneous host rocks at Zaozigou and causative intrusions at Dewulu and similar Au-Cu skarns in the region suggest a contemporaneous district-wide mineralizing event genetically linking gold mineralization and magmatism. Recently a case has been made that Zaozigou should be classified as an orogenic gold deposit (Yu et al., 2019; Qiu et al., 2020).

Qiu et al. (2020) and Sui et al. (2020) measured $\delta^{34}\text{S}$ S isotopes of ore related stibnite, pyrite, arsenopyrite, chalcopyrite, and marcasite. Both groups found similar values that range from -12.0 to -5.5 ‰. Sui et al. (2020), who propose a RIRGS model for the formation of the Zaozigou deposit, interpret these sulfur isotopes as evidence that the Triassic dikes assimilated sedimentary material during emplacement. Qiu et al. (2020) suggest that the sulfur isotopes are consistent with sulfur carried by metamorphic fluids such as those which form orogenic gold deposits. Additionally, Qiu et al., (2020) found that the sulfur isotopes of ore sulfides at Zaozigou are inconsistent with local established magmatic-hydrothermal deposits, which range from ~ -5.0 to $+6.0\%$. They found that hydrothermal monazites had calculated $^{206}\text{Pb}/^{238}\text{U}$ ages of 211.1 ± 3.0 Ma. This is interpreted to indicate that the Zaozigou Au-Sb deposit formed from metamorphic fluids 30 m.y. after magmatism. Earlier reported zircon U-Pb ages of mineralization are based on observed relative timing relationships of intrusions in drill core. These relationships were not substantiated in the present study, and field observations are presented that directly contradict previously described timing relationships. This highlights the necessity of a coherent geological framework for evaluating the Zaozigou Au-Sb deposit.

Sui et al. (2018: Fig. 4F) describe an unaltered diorite porphyry intrusion within a sericitized quartz diorite (identified as quartz dacite porphyry in the present study) as field evidence that the diorite at Zaozigou occurs post-mineralization, and thus brackets the age of gold mineralization. However, the figure does not show any indication of ore mineralization other than several wispy quartz-sericite veinlets. Additionally, their local geologic map clearly shows ore-hosting faults and fracture zones to be crosscutting all generations of dikes including quartz diorite porphyry dikes, granodiorite dikes, and diorite porphyry dikes (Sui et al., 2018 Fig. 3). My present field observations show clear and obvious evidence that the diorite porphyry dikes at Zaozigou do not bracket the age of gold mineralization, but do bracket an early, barren generation of quartz±sericite veinlets (Figure 1.11). This relationship strongly suggests that the quartz dacite porphyry dikes at Zaozigou could not have been causative intrusions. During fieldwork for the present study, nowhere within the 5 km² surface quadrangle, nor in the 13 visited mine sublevels that were mapped in detail, have any of the identified Triassic intrusions been conclusively observed to crosscut any orebody.

All existing literature is consistent in asserting that the orebodies at Zaozigou are explicitly structurally controlled by faults, which are at or near the contacts between Triassic dikes and Gulangdi sediments. However, there has been very little new mapping or structural analysis since Chen et al., (2013), who mapped structures at the surface, and was the first researcher to attempt to quantify the correlation between structures and mineralization. Little context for the structural, lithological, and hydrothermal alteration has been given in previous studies that present the results of U-Pb dating, stable isotope analyses, and other analytical methods. Additionally, the Gulangdi sedimentary host rocks are consistently referred to in the

literature as being Triassic in age, however it is probable that they are at least Permian, as intrusions have been dated to at least 248.9 ± 1.1 Ma (Sui et al., 2018).

The lack of a definitive deposit model with which to classify Zaozigou has led many researchers to focus on the area in high detail. This influx of higher-level geological work has been conducted largely without associated advancements in our fundamental understanding of the geological and tectonic context of the Zaozigou deposit. This thesis aims to more clearly define the sequence of events and processes which led to the formation of the Zaozigou deposit. The characteristics of the host rocks, structural features, hydrothermal alteration, and ore mineralization assemblages are described. A logical evolutionary history is interpreted based on relationships observed in the field and laboratory. A fundamental framework with which to evaluate the Zaozigou Au-Sb deposit is proposed.

1.2 Analytical Methods

Evaluation of the Zaozigou deposit was conducted both in the field, and in the laboratory. The fieldwork portion of this research was conducted during a three-month period on-site at the operating Zaozigou mine in the summer of 2018. The laboratory portion of this study was conducted from the Autumn of 2018 through the summer of 2020. On-site field investigation focused on mapping the spatial distribution of host rocks, structures, orebodies, and hydrothermal alteration packages. Laboratory evaluation through the application of Shortwave Infrared (SWIR) spectrometry, petrography, bulk rock geochemistry, scanning electron microscopy, and gravitational mineral separation focused on describing the occurrence of ore and alteration minerals, and their relationships with the host rocks and structures in which they are found. Full method details are explained in Appendix E.

Field investigation of Zaozigou consisted of mapping the surface and underground mine levels of the Zaozigou Gold Mine. There were no prior geological plan maps of the underground workings, but mine plan surveys were available. Mapping focused on the geology, structure, alteration, and mineralization of the gold-hosting structures and orebodies. In total 132 field samples were collected and their locations recorded.

Shortwave Infrared Spectrometry was conducted during the fieldwork season. Each sample collected was analyzed in three spots for 3-20 seconds per analysis. The SWIR spectra data were interpreted using The Spectral Geologist™ and ViewSpec Pro™ software. The identification of hydrothermal alteration minerals using SWIR was used to determine alteration assemblages and map the assemblages' spatial zonation.

Following field work, select rock samples were chosen to prepare petrographic polished thin sections. A total of 61 sections were cut and polished at the Colorado School of Mines thin section lab. Thin sections were observed using petrographic microscope in transmitted, reflected, and polarized light. Ore mineral assemblages, hydrothermal alteration assemblages, host rock composition, and mineral reactions were observed and recorded. Relationships observed in petrographic thin sections informed the later selection of samples chosen for bulk rock geochemistry and scanning electron microscopy.

Bulk rock geochemical samples (31 total) were selected and sent to Bureau Veritas Minerals in Vancouver for analysis. The selected analytical package was an ultra-trace reconnaissance level analysis which included 70 analytes including gold by Pb collection fire assay, major oxides by Li-borate fusion, and trace elements by ICP-MS. The bulk rock geochemical analysis provides further context for analysis of ore and alteration mineral reactions, ore and alteration mineral assemblages, and geochemical zonation profiles.

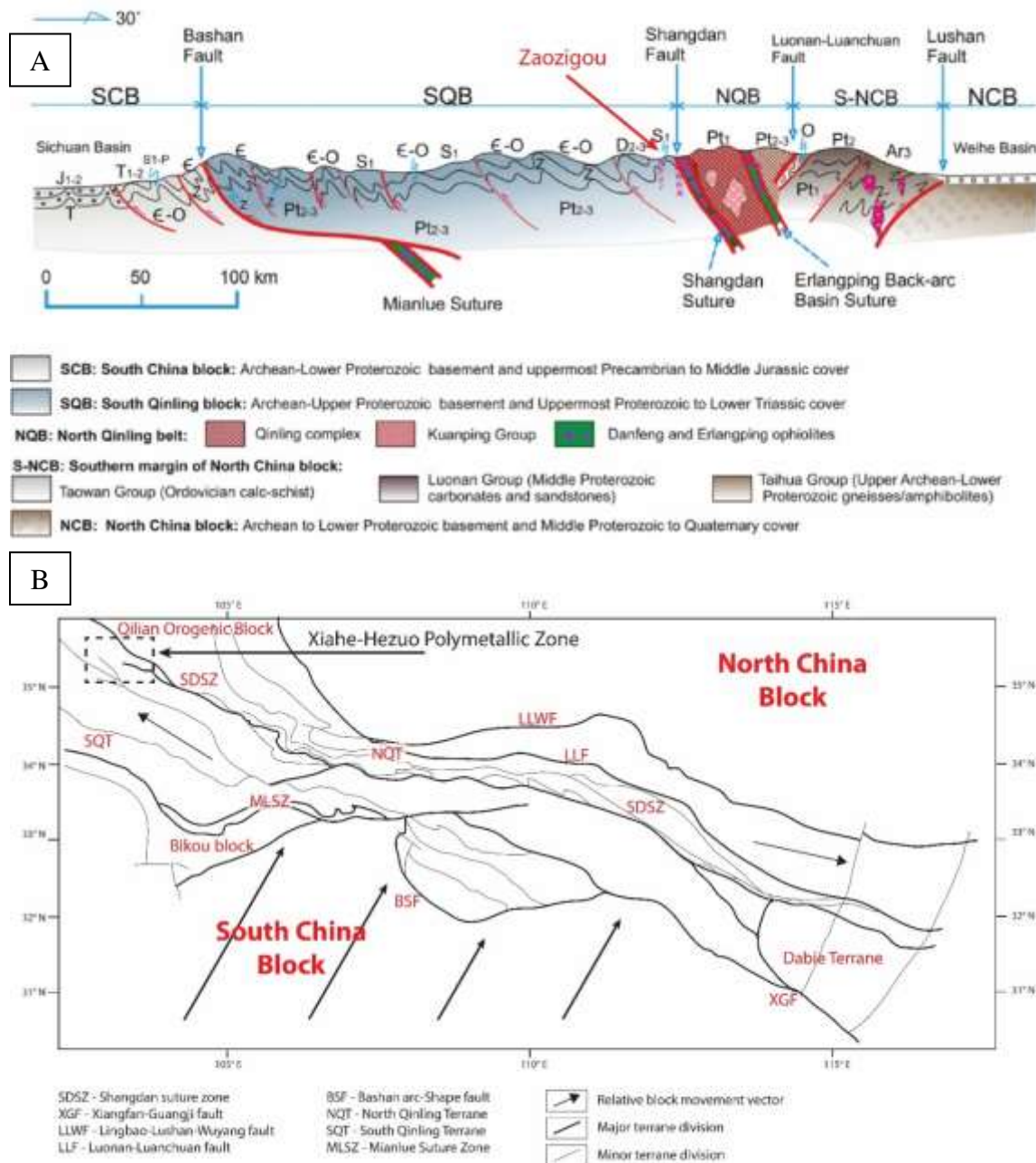


Figure 1.1 Tectonic position of Zaozigou in the context of the Qinling Orogen. Modified after Dong et al., (2011). A.) is a 30° cross section through the center of the Qinling Orogen. The relative position of Zaozigou is highlighted south of the Shangdan Suture zone in Proterozoic to Lower Triassic cover sequence which has been extensively folded through compressional orogenesis. B) is a plan view map of the tectonic units comprising the Qinling Orogen, with the location of the Xiahe-Hezuo Polymetallic Zone highlighted.

Investigation by field emission scanning electron microscope (FE-SE), energy dispersive X-ray spectrometry (EDS), and quantitative evaluation of materials by scanning electron microscope (QEMSCAN) was performed on 6 selected carbon-coated petrographic thin sections which were earlier observed using petrographic microscope. Mineral replacement reactions were observed and the composition of ore minerals was analyzed.

High grade samples following bulk rock geochemistry were investigated by primitive gravitational separation methods (gold panning crushed samples with a standard gold pan). Gold panning crushed samples is a quick and inexpensive way to investigate the presence of coarse free gold in samples. Samples were crushed by hand using a mortar and pestle, and the crushed material was panned until gold grains were liberated.

1.3 Regional Setting

The Qinling orogen is an orogenic belt that stretches E-W across central China (Figure .1b). The Qinling orogen evolved through a series of terranes accreting onto the North China Block. The history of the Qinling orogen in the Precambrian is not well understood. Proterozoic ophiolites, granitoids and back-arc basin volcanic rocks are taken as evidence of a Proterozoic Grenvillian orogen in the southern region of the North China Block ca. 978 to 859 Ma (Dong et al., 2008; Dong et al., 2011). At the start of the Paleozoic the North China Block and South China Block were separated by the Shangdan Ocean (Figure 1.2a). Subduction of Shangdan oceanic lithosphere led to the development of the North Qinling island-arc terrane which was separated from the North China Block to the north by the Erlangping back-arc basin and to the south by the Shangdan Ocean (Figure 1.2b). Through further subduction, the Erlangping back-arc basin began to close and the North Qinling Terrane accreted to the North China Block at the Erlangping Back-Arc basin suture (Figure 1.2d). Northward plate movement

of the South China Block had initiated rifting in the south, leading to the separation of the South China Block and South Qinling Block, which continued its movement to the north, resulting in the closure of the Shangdan Ocean, accreting to the North Qinling Block along the Shangdan suture likely in Late Devonian (Figure 1.2e). The rifting in the south between the South China Block and South Qinling Block developed into the Mianlue Ocean in the early Carboniferous (Figure 1.2f). Northward plate movement of the South China Block initiated subduction in the Permian and Triassic of the South China Block beneath the South Qinling Block, resulting in the accretion of the South China Block and South Qinling Block along the Mianlue Suture (Figure 1.2g,h). Accretion and continental collision continued into the Cretaceous (Dong et al., 2011).

The Qinling Orogen hosts three generations of granitoid and gabbroic intrusions clustered around the early Paleozoic, early to mid-Triassic, and Jurassic-Cretaceous. In the northwestern part of the Qinling Orogen, south of the Shangdan Suture Zone and in the area hosting Zaozigou, intrusions are primarily Triassic in age and intrude clastic rocks reportedly from the early to mid-Triassic Gulangdi Formation. Detrital zircon ages in the Gulangdi Formation have a dominant peak ca. 440 Ma and minor peak at ca. 277 Ma (Yan et al. 2019, 2σ and 95% confidence and error not reported). The timing of the reliably dated quartz dacite porphyry intrusions at 248.9 ± 1.4 Ma (Sui et al., 2018) suggest that the (meta)-sedimentary host rocks at Zaozigou were deposited early than the Triassic and may in fact be Permian or earlier. It may also be possible that the uplift and overturning experienced within the Xiahe-Hezuo district has exposed deeper Paleozoic accretionary sediments.

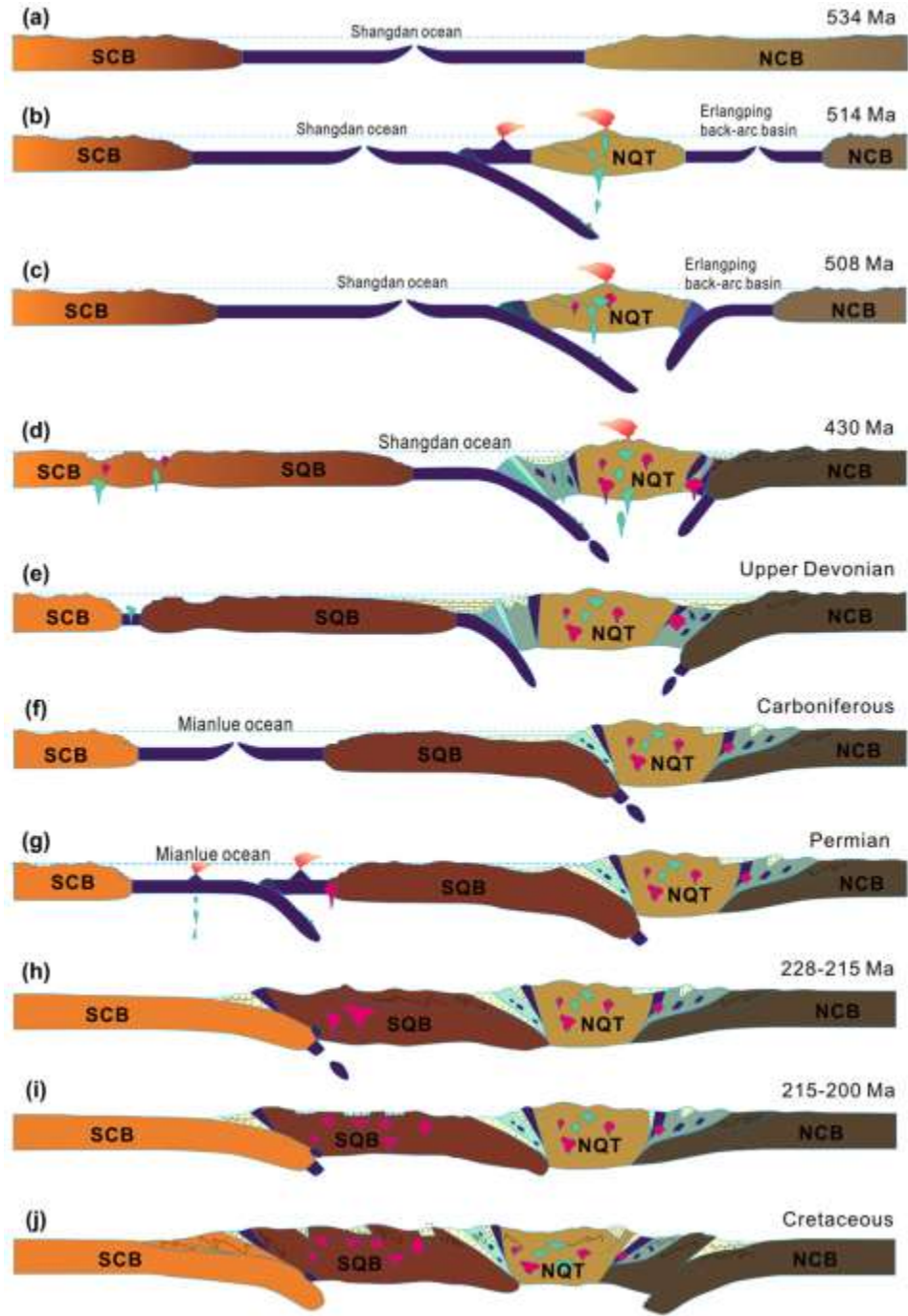


Figure 1.2. N-S cross sections of the Qinling Orogen showing the tectonic evolution of the orogen through geologic time. Significant events included the closing of the Shangdan and Mianlue oceans in the upper Devonian and Permian-Triassic, respectively. From Dong et al., (2011).

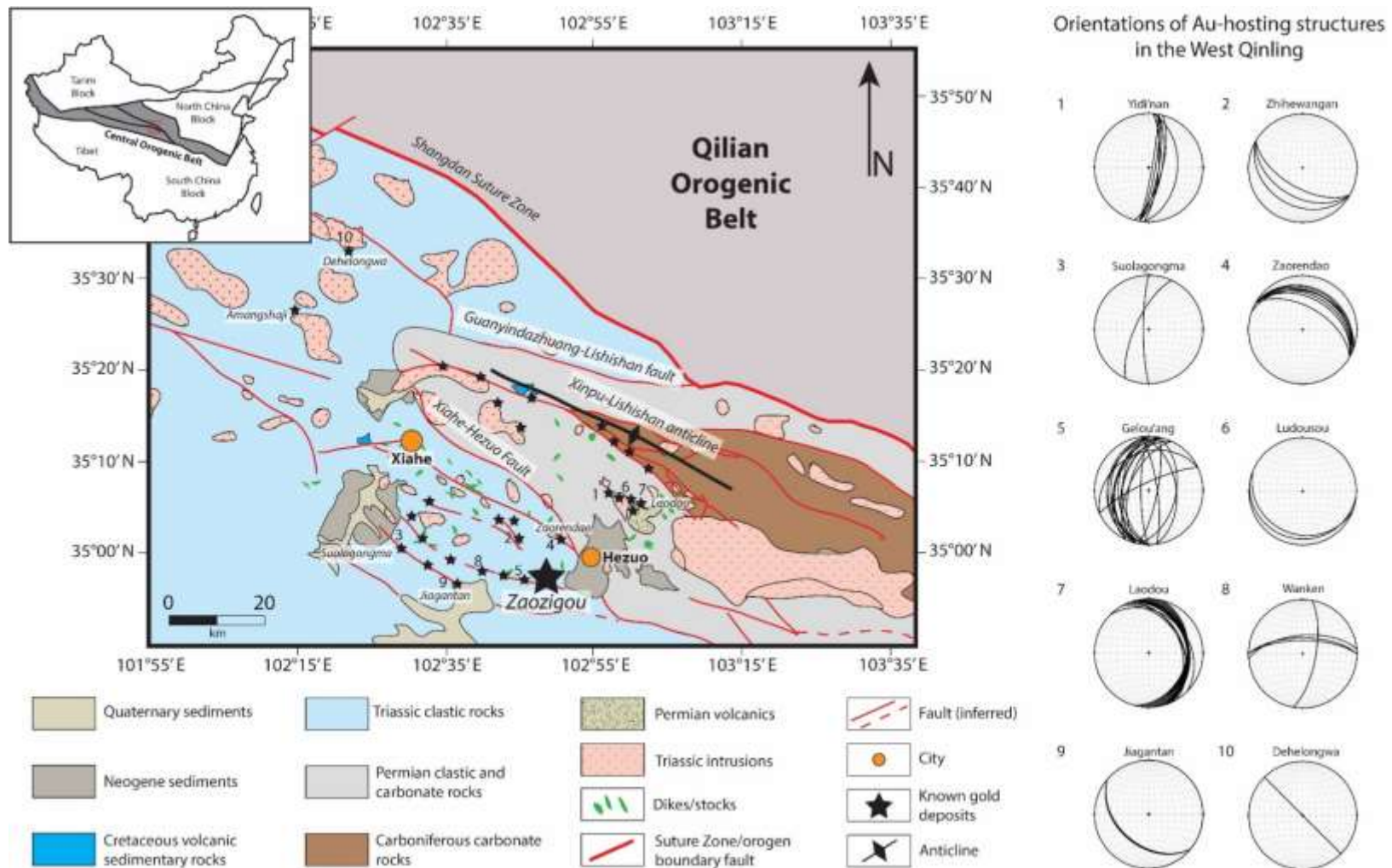


Figure 1.3. Regional geological map of the Xiahe-Hezuo mineralized zone in the context of the West Qinling Orogen. Orientations of planar Au-hosting structures at known gold deposits in the Xiahe-Hezuo Polymetallic zone are represented by stereonet. 1. Yidi'nan, 2. Zhihewangan, 3. Suolagongma, 4. Zaorendao, 5. Gelou'ang, 6. Ludousou, 7. Laodou, 8. Wanken, 9. Jiagantan, 10. Dehelngwa. Figure modified after Qiu et al., (2020). Structural orientations of deposits from: Yu et al., 2020 a; Yu et al., 2020 b; Technical Report, Silk Road Resources 2008; Gou et al., 2019; Dou et al., 2012; Jin et al., 2017; Zhou 2011; Dai et al., 2016; personal communication

The Xiahe-Hezuo polymetallic zone, which hosts numerous gold, copper, antimony, and tungsten deposits, is spatially associated with a series of interpreted second order NW-trending regional faults possibly related to the compressional orogeny which produced the Shangdan Suture Zone and Lishishan Anticline (Figure 1.3). These faults have not been directly mapped.

Orientations of the known orebodies within deposits of the Xiahe-Hezuo polymetallic zone are variable (Figure 1.3). The orebody orientations tend to be either subparallel to the interpreted Shangdan Suture Zone, such as the case at Jiagantan (9), Zaorendao (4), Zhihewangan (2), Ludousou (6), and Dehelongwa (10), or at high angle or oblique to the Shangdan Suture Zone, such as at Gelou'ang (5), Suolagongma (3), Yidi'nian (1), and Wanken (8) (Figure 1.3). The stereonet shown in Figure 1.3 are approximations based on the best available data, but these smaller deposits are not widely studied or published in the literature, so a substantial amount of estimation has been made to represent them, including measurement of dips and azimuths from maps and cross sections. The style of orebodies at these smaller deposits are also not well characterized. Most are described as veins or fault hosted orebodies. It is inferred that the orebodies reported are fault-fill vein styles similar to Zaozigou.

The known deposits within the Xiahe-Hezuo polymetallic zone are strongly associated with the lower order faults that have orientations sympathetic to the Shangdan Suture Zone and are primarily Triassic in age, although caution is advised prior to placing high confidence in these ages due to the relatively under-studied nature of these deposits and lack of a cohesive regional geological framework within the Xiahe-Hezuo region.

Regional Metamorphism in the West Qinling follows the tectonic evolution of the orogenic belt. The Proterozoic evolution included subduction related Grenvillian metamorphism (Dong et al., 2008), including ophiolitic sequences of highly metamorphosed ultramafic and

mafic rocks. Paleozoic metasedimentary rocks, including flysch turbidites from the Devonian, Carboniferous, and Permian, achieved greenschist to amphibolite facies metamorphism during continental accretion related to the closure of the Shangdan Ocean and suturing along the Shangdan fault zone, mostly around the late Carboniferous (Zhai et al. 1998). The metasedimentary rocks are related to the subducting fore-arc accretionary wedge which was thickened during subduction and accretion related to Shangdan suturing in a Barrovian-style metamorphic sequence (Mao et al. 2017). The fore-arc accretionary wedge sediments were metamorphosed and exhumed from ca. 330 Ma to 250 Ma (Dong et al. 2011). Sedimentation of clastic turbidite and flysch sequences continued in the forearc and backarc of the South Qinling Block during the Permian to Triassic subduction of the Mianlue oceanic crust. Entering the Triassic through Jurassic, regional metamorphism in the West Qinling Orogen was mostly low-grade metamorphism. Triassic sedimentary rocks are generally dominated by slates and greywackes deposited in ocean basins. They exhibit low grade metamorphism or are unmetamorphosed.

1.4 Local Geology

The Zaozigou gold deposit is hosted by the sedimentary Gulangdi Formation and several generations of Triassic porphyritic dikes of intermediate to felsic composition. The porphyritic dikes are aligned roughly parallel to regional NE-SW structural fabric. These dikes at Zaozigou are most commonly dacite, quartz dacite, diorite, quartz diorite, and granodiorite in composition. The Gulangdi Formation is an interbedded carbonaceous sandstone and mud/siltstone flysch. At Zaozigou in proximity to the Triassic dikes, the Gulangdi Formation interbedded carbonate sandstone-mudstones are contact metamorphosed to a hornfels unit which largely maintains the thickness and composition of the sedimentary beds of the protolith. The Gulangdi Formation is

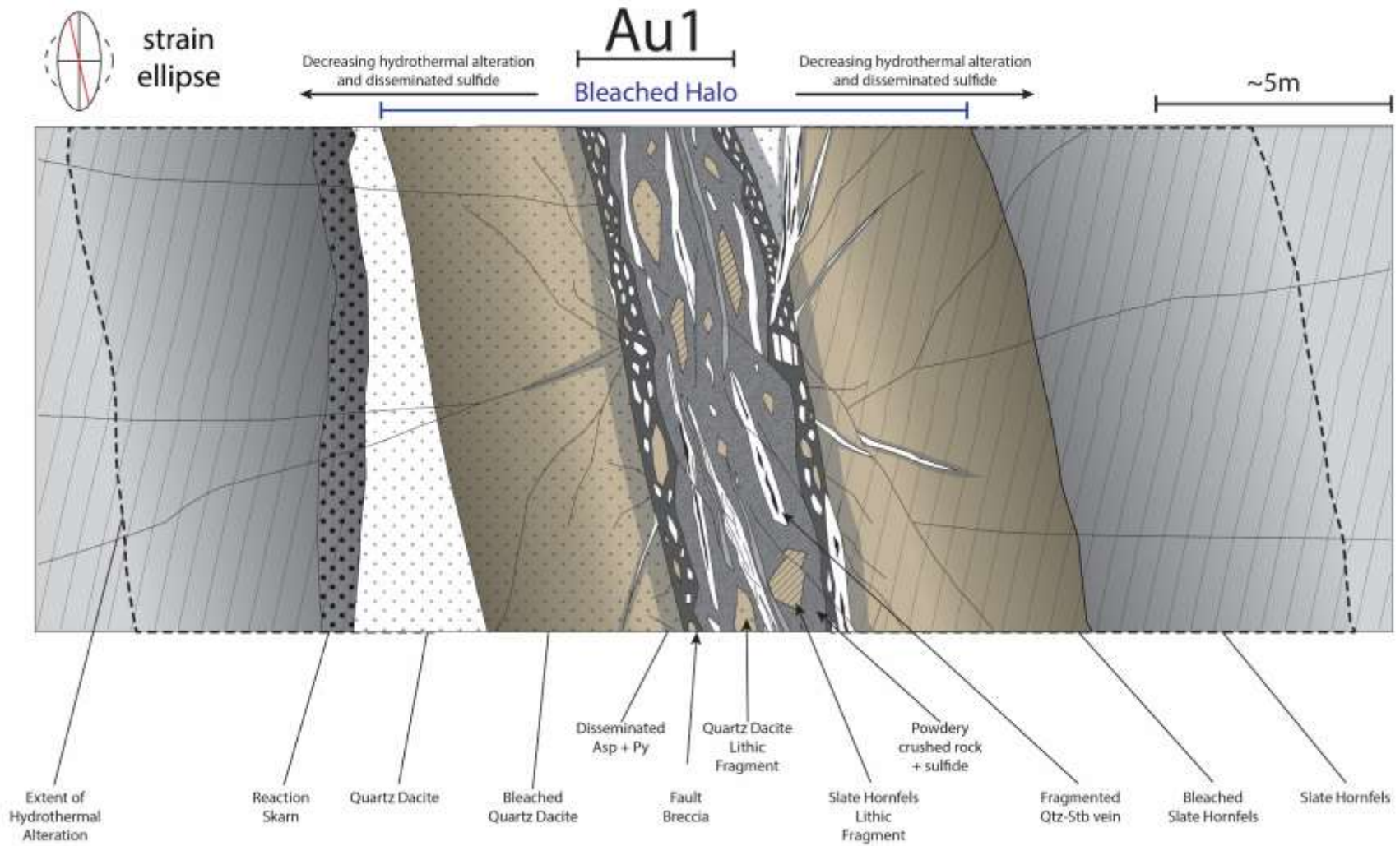
frequently referred to as being a middle Triassic slate which would suggest that the Gulangdi Formation is older than many of the Triassic intrusions which have been consistently dated to have emplaced ca. 244.8 ± 1.4 to 248.9 ± 1.4 Ma (Sui et al. 2018; Sui et al. 2020; Qiu et al. 2020). Yan et al. (2019) dated detrital zircon grains in the West Qinling Mountains, finding a youngest U-Pb peak age of ca. 273 Ma (analytical error not reported).

The Zaozigou deposit consists of orebodies which occur in two discrete orientations: steeply to subvertically dipping, and shallowly dipping. The orebody nomenclature is ascribed based on the geometries of the orebodies but is also a useful discriminator when describing mineralization style.

Orebodies with the Au prefix (eg. Au1, Au9) are the steeply dipping ($77^\circ - 85^\circ$) orebodies and outcrop at the surface. Orebodies with the “Au” prefix are brecciated and contain fragments of quartz-stibnite veins as well as hydrothermally altered wall rock fragments containing disseminated auriferous arsenopyrite and pyrite. The breccia cement is crushed wall rock and hydrothermal quartz-stibnite infill. The “Au” orebodies range in width from ~1 to 10m. The “Au” orebodies are fault-hosted and were the main conduits for hydrothermal ore fluids.

Orebodies with the “M” prefix (e.g. M4, M7) are the shallowly dipping orebodies, most of which dip between 19° to 30° . These are “blind” orebodies which are not exposed at the surface. They are discrete, laminated, quartz-stibnite veins which have quartz rims and massive stibnite centers (Figure 1.5). The “M” orebodies range from 30cm to at least 3m in thickness.

Figure 1.4. (Next Page) Schematic diagram of the Au1 fault-hosted ore body. This schematic diagram is representative of all “Au” style orebodies. “Au” style orebodies are steeply dipping, reverse fault hosted orebodies. Ore is present as quartz-stibnite veins, hydrothermal sulfide breccia infill, and sulfidation of wall rock clasts which are fragments caught up within the cataclastic fault action. The outer boundaries of the “Au” orebodies are the focus of extreme brecciation which includes brecciation of quartz-stibnite veins, wall rock fragments, and fragments of earlier breccias generated through faulting. The “Au” orebodies were reactivated multiple times, as evidenced by vein and sulfide bearing fragments being re-brecciated. Within the ore-hosting fault, the fault material is ashy in appearance and consists of fine crushed rock and vein material. The crushed rock material is strongly hydrothermally altered, similar to larger altered wall rock fragments which were broken off and incorporated during fault activation and reactivation. Hydrothermal alteration occurred during initial fault activation and reactivation. The “Au” style orebodies have wide bleached alteration haloes up to 20m. The alteration haloes are regions of sericitic alteration and associated disseminated arsenopyrite and pyrite.



M4

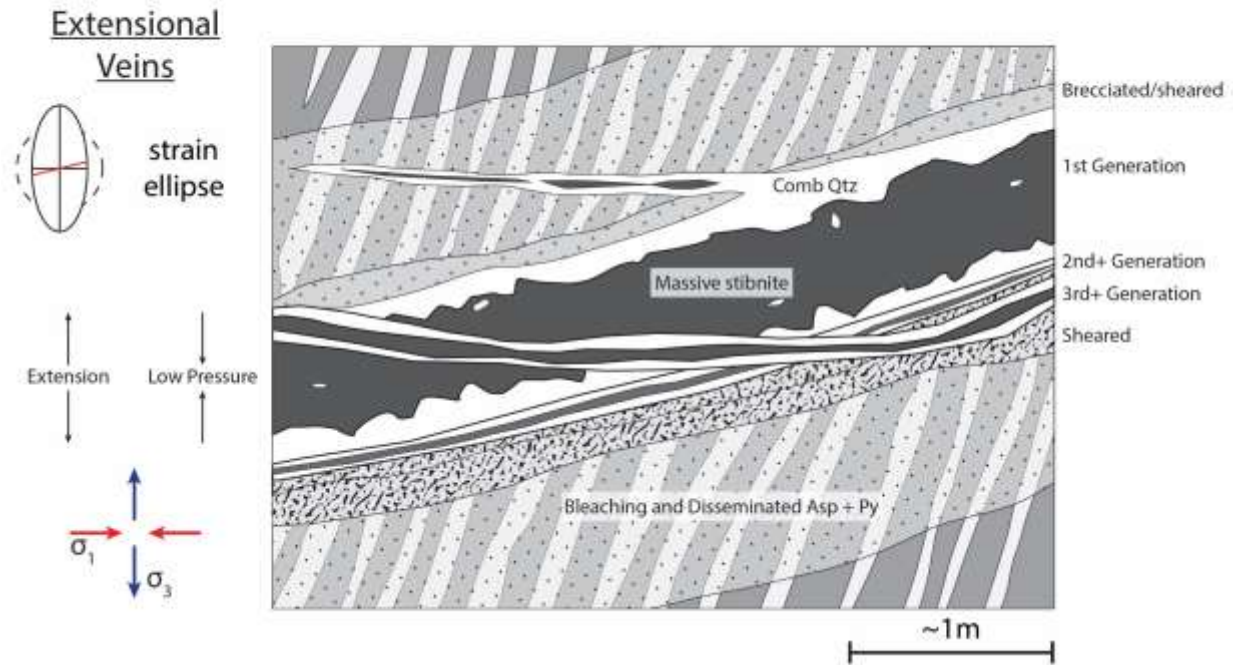


Figure 1.5. Schematic diagram of the M4 orebody. This schematic diagram is representative of all observed “M” style orebodies. The “M” style orebodies are shallowly dipping, fault hosted quartz-stibnite extensional veins. Quartz precipitates at the rims of the veins and crystal growth is oriented towards the center of the vein which is filled with massive stibnite. Several episodes of veining are present, usually later crosscutting veins are focused at the vein-wall rock contact, which is typically strongly brecciated and sheared. Bleached alteration haloes are present in the hangingwall and footwall of “M” style orebodies.

The subvertically dipping “Au” orebodies are found at the faulted margins of Triassic dikes at the contact with the metasedimentary rocks, likely because the rheological contrast localized brittle fracturing and faulting. These orebodies are typified by frictionally milled breccias which have experienced multiple episodes of reactivation. The larger Au orebodies (Au1, Au9) are fault bound, weakly competent bodies composed of relict quartz-stibnite veins/veinlets, altered crushed host rock, and lithic fragments. The Au1 and Au9 orebodies likely formed early in the deposit history, and were reactivated during each subsequent pulse of mineralization, leading to the development of low-competency, broken and widely

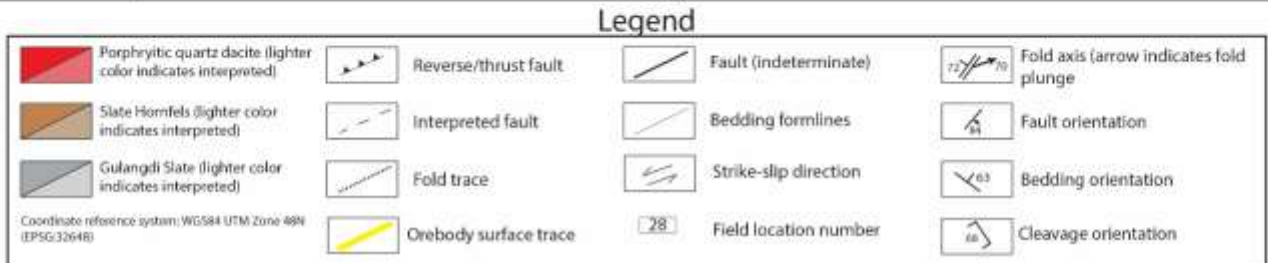
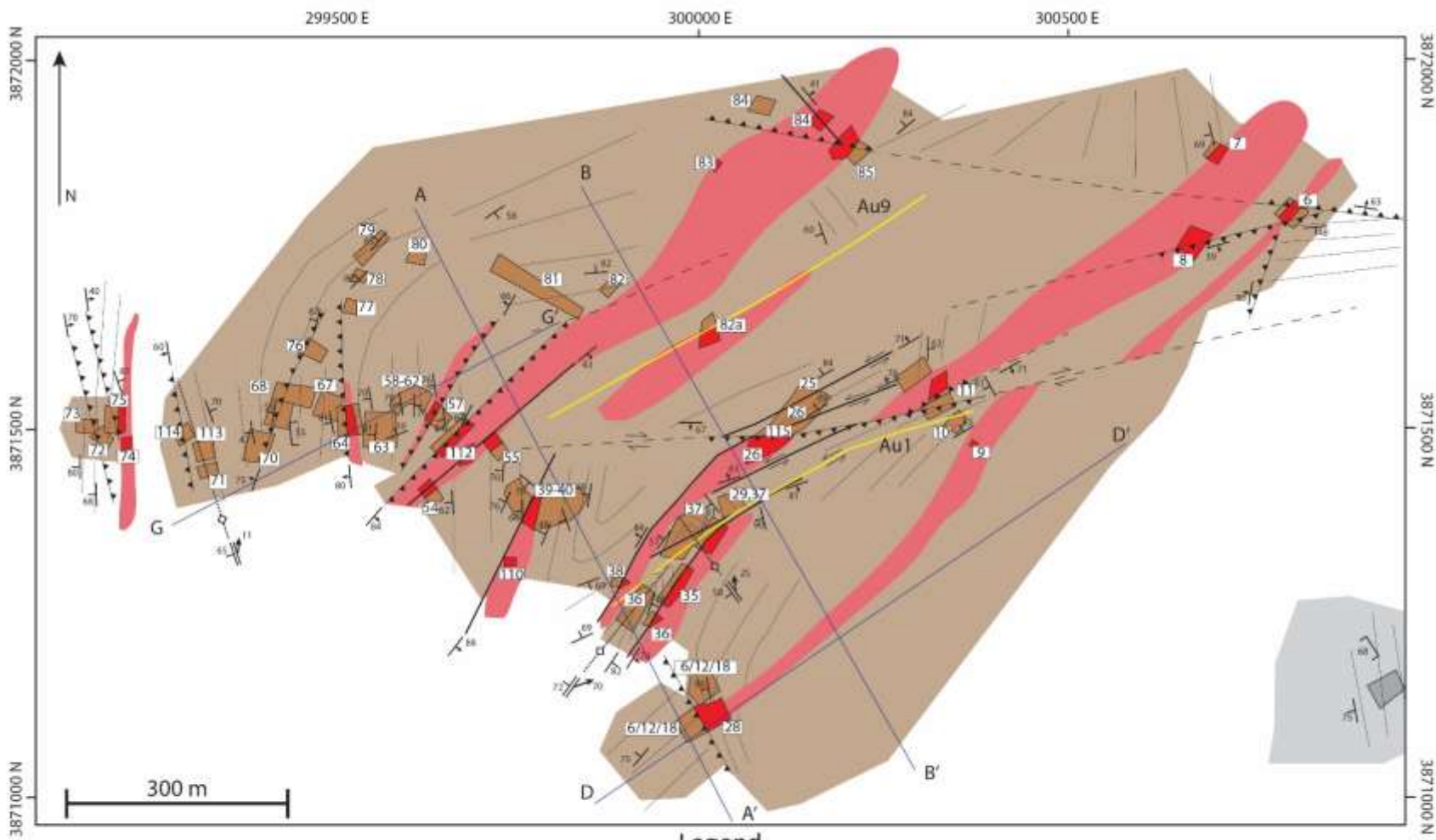
unconsolidated orebodies which are confined to the interface between fault surfaces. Bleached alteration haloes surrounding the Au1 and Au 9 which host disseminated arsenopyrite and pyrite were measured laterally up to 20m in width.

The shallowly dipping “M” orebodies do not exhibit any specific spatial relationship to the Triassic dikes. Crosscutting relationships with “Au” orebodies are cryptic and not easily observed, in part due to the nature of Zaozigou as an active mine. As such, the intersection of “Au” and “M” orebodies has not been directly observed. Spatial mapping of orebodies across the underground mine workings indicates that, generally, the structures hosting “M” orebodies crosscut and offset “Au” orebodies, which may be evidence of a timing relationship between the subvertically- and shallowly dipping orebodies. This cannot be asserted with certainty because both the “Au” and “M” orebodies are shown to have experienced multiple stages of reactivation and minor structures parallel to “Au” and “M” orebodies are observed to have mutually crosscutting relationships.

1.5 Lithologies at Zaozigou

Two lithologies are dominant at Zaozigou: a contact metamorphosed Triassic slate interpreted to be of the Gulangdi Formation and quartz dacite porphyry dikes dating to range from 248.9 ± 1.4 Ma to 244.8 ± 1.4 Ma (Sui et al., 2018; Yu et al., 2019). The emplacement of the quartz dacite porphyry dikes is responsible for the contact metamorphism of the Gulangdi slate, converting the interbedded siltstone-carbonate sandstone to a hornfels. A later generation of diorite dikes cross cuts the earlier established quartz dacite-sedimentary intrusive contact. The main lithologies are discussed in more detail below:

Figure 1.6 (Next Page) Map of the surface geology of Zaozigou. Drawn from field observation independent of previously published geological maps. Surface traces of the Au1 and Au9 orebodies are shown in yellow. Au1 and Au9 trend NE-SW. The likely initiated as left lateral strike slip faults, as evidenced by SW raking fault surface lineations. Triassic quartz dacite porphyry dikes trend parallel to the NE-SW faults which host the Au1 and Au9 orebodies. The contact between the dikes and slate hornfels is often faulted, which may be indicative that the dikes intruded along NE-SW trending faults, or that the rheological contrast between the dikes and slate hornfels focuses faulting at the margins. Early stage fold -thrust features are observed clearly at locations 37 and 71. The orientation of the axial planes of these folds are parallel with foliation measured at the southwest corner of the mapped area, where fresh slate is exposed and was sampled as ZZG18-030.



1.5.1 Slate Hornfels

The hornfels in the mine area is an interbedded black and white unit which preserves many of the primary sedimentary features of the Gulangdi Formation protolith. The layers are alternating lightly colored sandy carbonate interbedded with dark brown to black argillaceous, iron-rich, fine-grained pelitic mudstone to siltstone, collectively herein referred to as a single rock unit termed slate hornfels, which is descriptive of the protolith, texture, and degree of metamorphism experienced by the rock unit. The less metamorphosed Gulangdi slate grades into the slate hornfels in proximity of the porphyritic intrusions. An outcrop of fresh Gulangdi slate is found southeast of the mining area (Figure 1.6, Figure 1.8a). Reaction skarns are found directly abutting intrusions throughout the mine, evidenced by the growth of almandine-grossular garnet and pyroxene preferentially within the carbonaceous lighter colored layers. Additional evidence is found in the form of carbonate minerals within the darker, iron-rich layers (Figure 1.8g, h). Reaction skarn is a result of isochemical metamorphism by the metasomatic transfer of Ca and Fe across sedimentary layers of differing composition, represented in the slate hornfels by the lighter colored Ca-rich carbonaceous layers, and the darker Fe-rich hornfels for which mudstone/siltstone is the protolith. Automated mineralogy (QEMSCAN) scans of the hornfels indicates a mineralogy of quartz-feldspar-muscovite/illite group-kaolinite group-calcite-ankerite. The sample analyzed was hydrothermally altered.

The slate hornfels at Zaozigou has lost the macroscopic mineral foliation that was present in the Gulangdi slate but maintains the flysch interlayering of carbonate and mudstone-siltstone. Due to the competency increase from the contact metamorphism and recrystallization of platy minerals, the slate hornfels does not fracture along cleavage planes. Instead, the hornfels exhibits conchoidal fracturing as well as planar fractures discordant to bedding or mineral foliation.

Approximately 800m from the closest mapped intrusion, a true slate is found which is interpreted to be an outcrop of the Gulangdi formation (Figure 1.8a). It has been previously described as silt-slate, slate, argillite, conglomerates, limestone, and sandstone by Sanogo et al. (2008), as interbedded siliceous, calcareous, silty, and argillaceous slates with lesser quartzite by Liang et al. (2016), or as interbedded sandstones, siltstones, calcareous siltstones, and mudstones by Sui et al. (2018). All are consistent in the description of a flysch silty, darkly colored fine grained foliated unit interbedded with a carbonaceous, slightly coarser grained, lighter colored sedimentary unit. This report supposes that the variations in the description of the metasedimentary host rocks can be attributed to the narrow metamorphic gradient from fresh interbedded slate-carbonate sandstone to the intrusion-proximal contact metamorphosed slate hornfels.

A notable feature of the fresh Gulangdi interbedded slate-carbonate sandstone is the macroscopic mineral-defined foliation, measured in outcrop 800m east of the mine area striking 147° and dipping 68° to the SE. The foliation there is discordant to the bedding orientation which strikes 170° and dips 75° to the ESE. The slate is fissile and marked by the tendency to fracture along bedding surfaces. Younging directions can be interpreted by ripples on bedding surfaces, flame structures, load casts, and bouma sequences (Figure 1.8f).

Bulk geochemical data of samples of slate hornfels collected at Zaozigou plot as having protolithic composition typical of shales and greywackes on the Herron (1988) terrigenous sedimentary rock discrimination diagram. Samples plotted here have not been standardized by alteration percentage or sulfide content. As many of the samples collected were chosen as representatives of mineralization styles at Zaozigou, disseminated Fe-sulfides (pyrite, arsenian pyrite, and arsenopyrite) exist in the rocks in varying abundances. Since the mineralizing system

at Zaozigou is not a closed system the Fe endowment represented by Fe sulfides may thus skew the y-axis values such that samples may in fact plot closer to greywacke in combination. The samples collected for the unaltered distal slate outcrop were included in the analysis. These unaltered samples also plot within the shale field. Petrology of the Gulangdi slate here is reasonably consistent with descriptions and petrology of Gulangdi slate reported elsewhere in the West Qinling Orogen, whose sedimentary grains have interpreted provenances from regional volcanic, granitic, metamorphic, and sedimentary (chert, carbonate, mudstone) materials likely derived from eroded material of the South Qilian Belt (Yan et al., 2020).

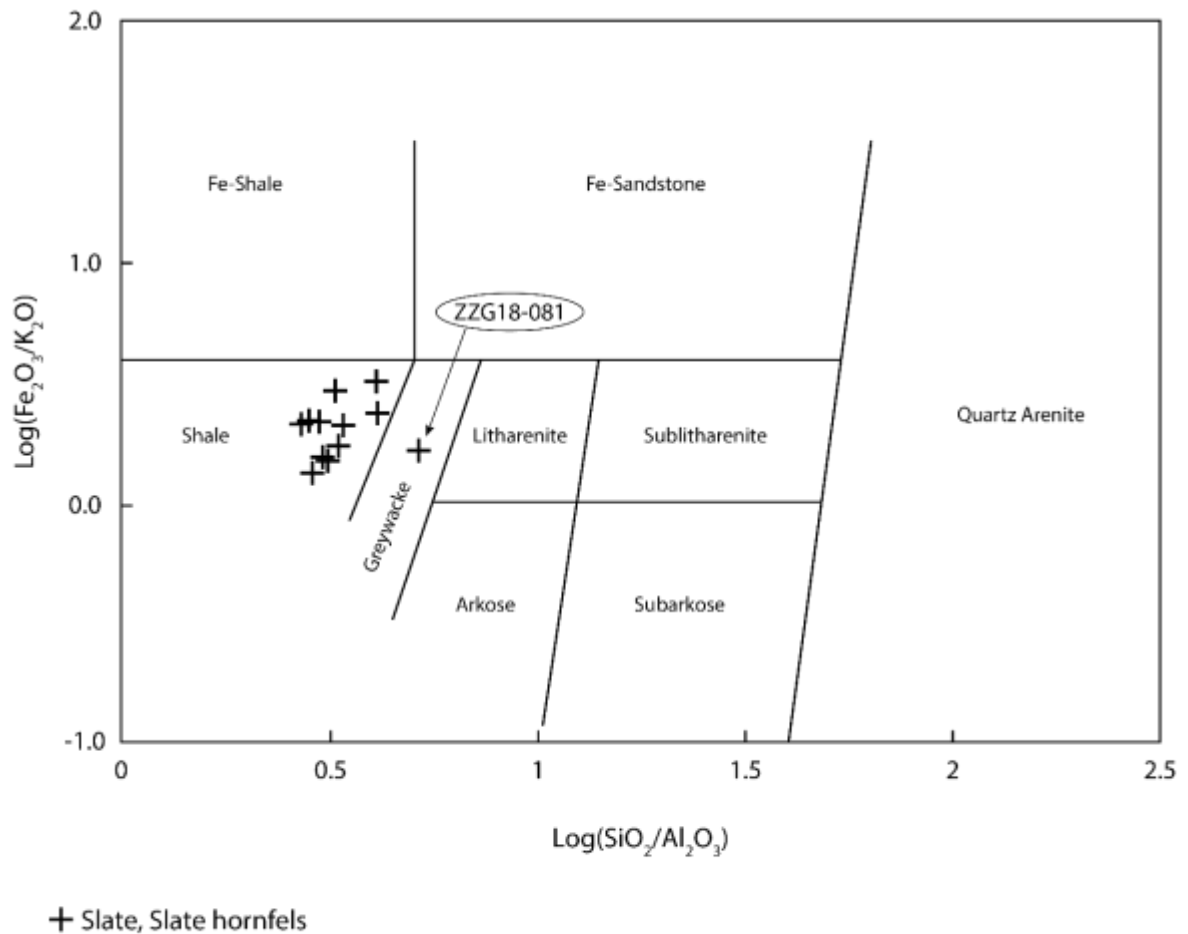


Figure 1.7. Discrimination plots for terrigenous sedimentary rocks. Bulk geochemical data plotted on axes suggested by Herron (1988).

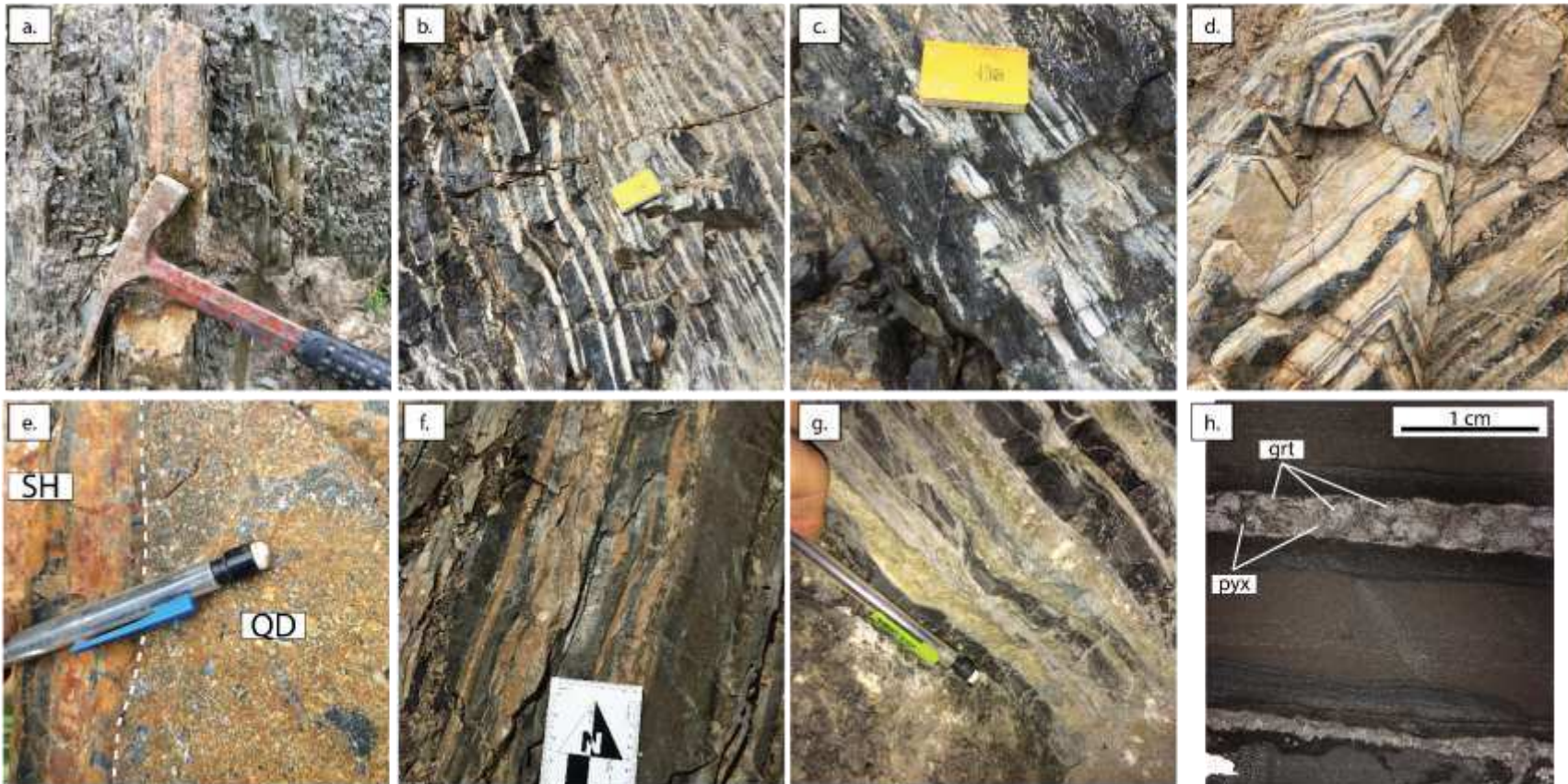


Figure 1.8. Outcrops of a.) fresh, unmetamorphosed Gulangdi slate sample ZZG18-016, found 800m east of the Zaozigou Mine area, b.-d.) Gulangdi slate hornfels which exhibit a lack of slaty cleavage or preferential fracture along bedding or mineral foliation planes e.) intrusive contact between a quartz dacite porphyry dike and slate hornfels. The quartz dacite porphyry exhibits chilled margins and iron oxide surface staining is observed on the slate hornfels, f.) moderately contact metamorphosed slate hornfels displaying preservation of primary sedimentary features, g.) proximal slate hornfels reaction skarn showing green colored Fe-calc silicates within lighter colored layers and iron carbonate mineral horizons at the contacts of marble and hornfels interbeds h.) plane polarized thin section scan of a slate hornfels. SH = slate hornfels, QD = quartz dacite porphyry, grt = garnet, pyx = pyroxene.

1.5.2 Quartz Dacite Porphyry

Quartz dacite porphyry dikes were emplaced into the Gulangdi slate ca. ~248 Ma (Sui et al., 2019; Yu et al., 2019) as dikes. The dikes are oriented subvertically, and trend NE-SW, parallel to the dominant structural trend in the Zaozigou area. The quartz dacite porphyry has phenocrysts of quartz, plagioclase, biotite, and minor hornblende and rutile in a predominantly plagioclase-quartz groundmass. Phenocrysts range in size, with quartz phenocrysts up to 1 cm typically being the largest, while plagioclase and biotite phenocrysts are usually <0.5 cm. The dikes display chilled margins where the intrusive contacts with sedimentary rocks are preserved. In places, angular slate hornfels xenoliths are found within the intrusive bodies with thermally eroded borders (Figure 1.9a), suggesting that the dikes may have been emplaced along existing faults zones or fractures with loose cataclastic sedimentary fragments. The quartz dacite porphyry dikes have been described by previous studies as granodiorites by Sui et al. (2018; 2020), and as dacites by Qiu et al. (2020). The geochemistry of these dikes plot as dacites on the Bas classification of volcanic rocks (Bas et al., 1986) with an unaltered dike sample collected at surface analyzed to contain 64.99 wt% SiO₂, 2.59 wt% Na₂O, and 3.09 wt% K₂O (Table 1.1, page 64). Due to the prevalence of the large (~0.5-1cm) quartz phenocrysts, and porphyritic texture, this unit has been termed quartz dacite porphyry.

Textural variations of the quartz dacite porphyry dikes are present but have not been mapped by the present study. The quartz dacite porphyry, which comprises the majority of the intrusive bodies, comprises <50% phenocryst by volume. There is a crystal crowded (phenocrysts >50% volume) variety of quartz dacite porphyry of the same phenocryst composition. A third variety is a quartz-phenocryst-poor dacite porphyry characterized by the notable lack of quartz phenocrysts, which maintains a similar bulk composition.

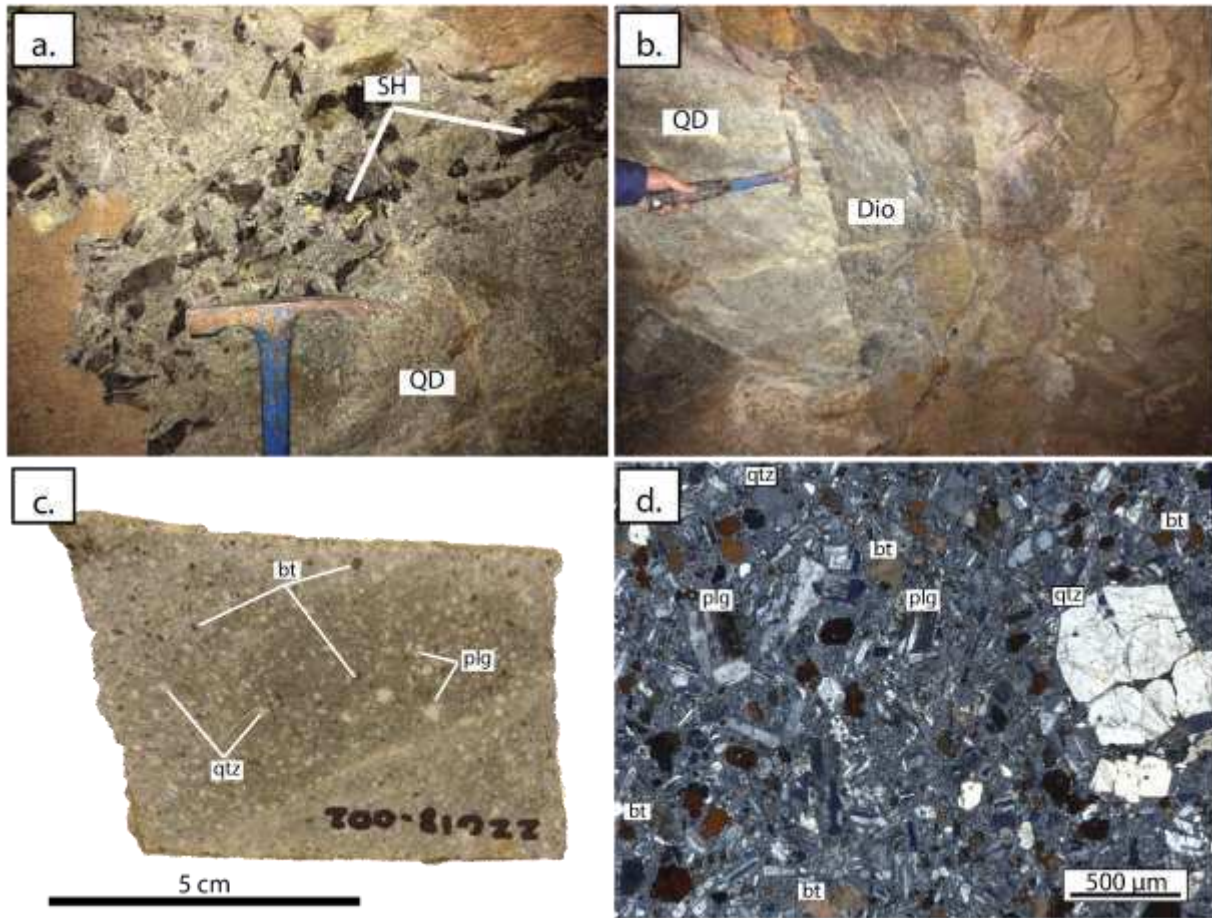


Figure 1.9. Photographs and photomicrograph of quartz dacite porphyry from Zaozigou. a.) A quartz dacite dike with angular slate hornfels xenoliths. b.) Diorite dike intruding a quartz dacite. c.) Quartz dacite porphyry hand sample. d.) Cross-polarized photomicrograph of porphyritic quartz dacite texture. SH = slate hornfels, QD = quartz dacite porphyry, Dio = diorite, qtz = quartz, bt = biotite, plg = plagioclase.

1.5.3 Diorite Porphyry

Diorite porphyry dikes intrude the hornfels and quartz dacite porphyry dikes. The dioritic dikes are volumetrically minor and are ore hosts where the dikes are crosscut by mineralized veins. Compositionally, the diorite porphyry dikes are similar to the quartz dacite porphyry dikes, however the phenocrysts are dominantly plagioclase and biotite. They are darker in color to the quartz dacite, and have higher proportions of plagioclase, biotite, and mafic minerals in the

groundmass.

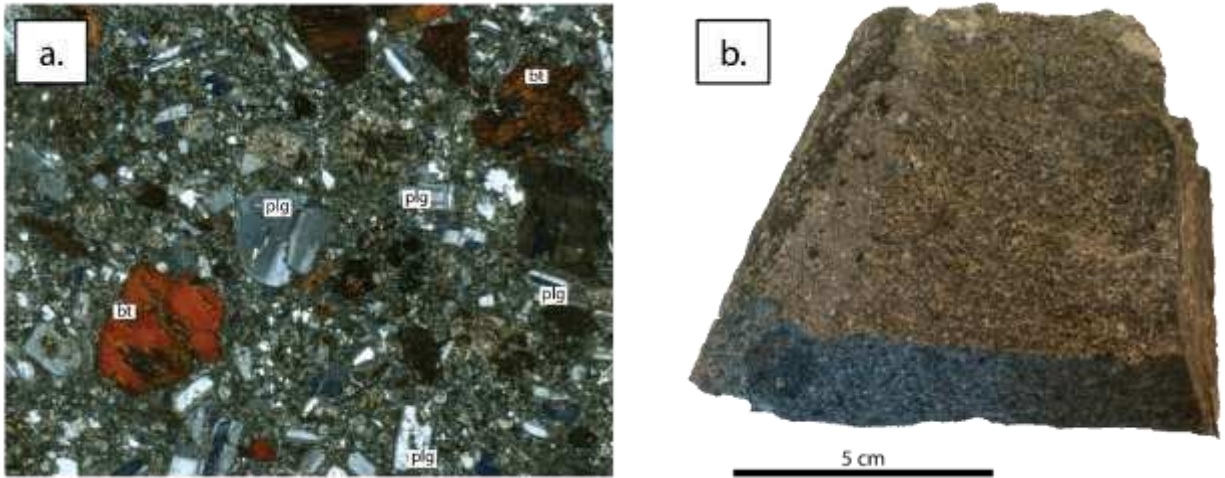


Figure 1.10. Photo and photomicrograph of diorite dike. Plg = plagioclase, bt = biotite

The bulk geochemistry of the fresh porphyritic diorite sample collected and analyzed plots as andesitic in composition, with 62.31 wt% SiO₂, 2.25 wt% Na₂O, and 2.09 wt% K₂O on the Bas classification scheme (Table 1.1, page 64) (Bas et al., 1986). In order to maintain consistency with previous publications, it has consistently been referred to as porphyritic diorite.

The diorite porphyry dikes are observed to be emplaced in the pre-ore stage. Mineralization hosted by the diorite porphyry dikes is similar to the mineralization hosted in the quartz dacite porphyry dikes. Despite field evidence of the diorite porphyry dikes predating orebody emplacement (Figure 1.11), the diorite porphyry dikes have been used by some researchers in attempts to bracket the age of mineralization. Reported ages of the porphyritic diorite dikes ranged widely from zircon LA-ICP-MS U-Pb ages of 237.5±1.5 Ma (Sui et al., 2018) to zircon SHRIMP U-Pb ages of 215.5±2.1 Ma and 216.6±2.4 Ma (Liu et al., 2012). The wide age range reported probably reflect confusion in the reported lithologies of dikes at Zaozigou, as the zircon U-Pb 237.5 ± 1.5 Ma reported by Sui et al. is concurrent with reported

magmatic monazite LA-ICP-MS U-Pb ages of 238.3 ± 2.6 Ma and zircon LA-ICP-MS U-Pb ages of 238.0 ± 1.8 Ma hosted in a dacite porphyry dike (Qiu et al., 2020). The porphyritic diorite dikes are also crosscut by mineralized veins and hydrothermally altered (Figure 1.11). Due to the observed crosscutting relationship, it is inaccurate to use the geochronology of the quartz dacite porphyry and diorite porphyry dikes at Zaozigou to bracket the age of mineralization.

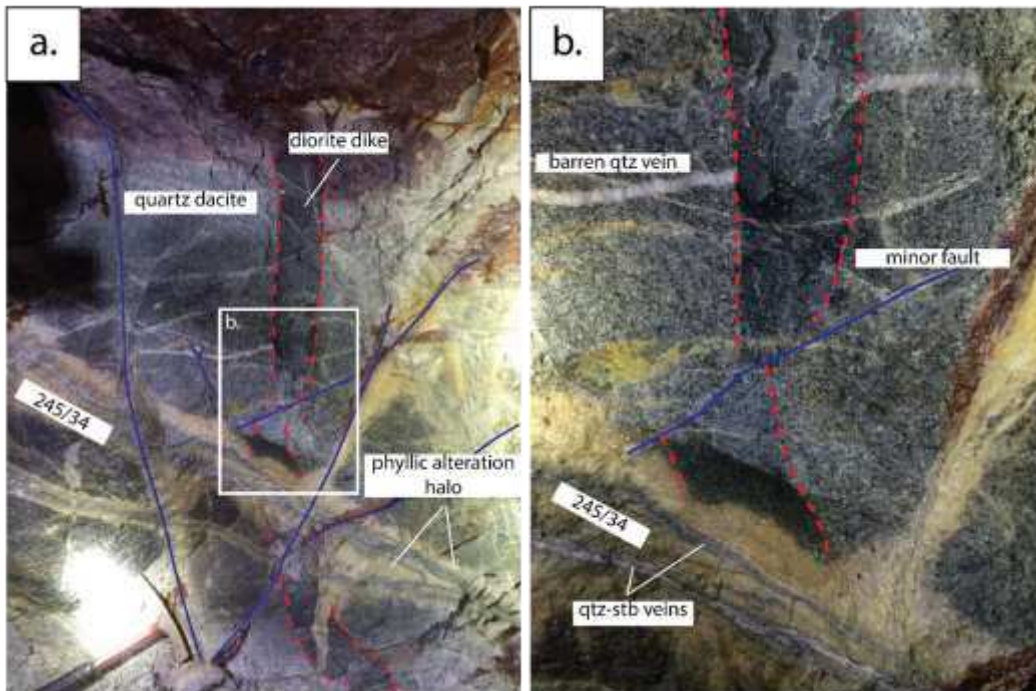


Figure 1.11. Diorite and quartz dacite porphyry dikes cross cut by mineralized quartz-stibnite veins. Tan regions are phyllic alteration haloes where biotite and plagioclase are replaced by sericite (illite and muscovite). Blue lines are minor faults, red dashed line represents the contact between quartz dacite porphyry and diorite porphyry.

1.6 Metamorphism at the Zaozigou gold deposit

Regional metamorphism in the host rocks at Zaozigou is overprinted by local contact metamorphism and hydrothermal alteration. Relatively Fresh quartz dacite porphyry samples

host phenocrysts displaying retrograde metamorphism mineral replacement reactions (Figure 1.12).

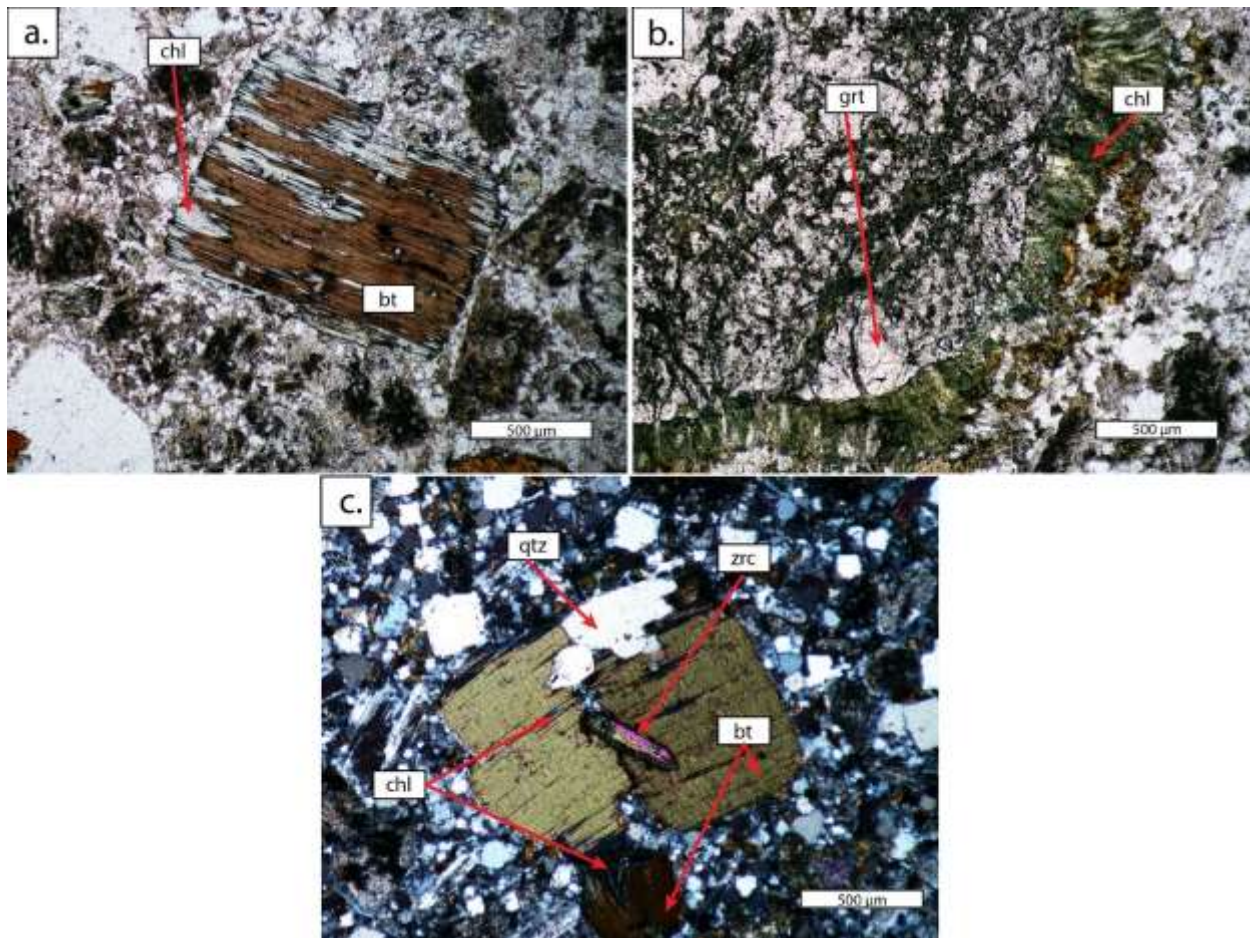


Figure 1.12. Metamorphic reactions in host rocks at Zaozigou. a.) chlorite replacement of biotite phenocryst in quartz dacite porphyry sample, observed in plane polarized light. b.) chlorite replacement of garnet rim in quartz dacite porphyry sample observed in plane polarized light. C.) quartz and chlorite replacement of biotite crystal. Zircon is liberated from biotite. Cross polarized light. Chl = chlorite, bt = biotite, grt = garnet, qtz = quartz, zrc = zircon.

Chlorite-quartz partially replaces biotite in situ (Figure 1.12a,c). This reaction is sometimes accompanied by liberation of zircon inclusions in garnet. In more strongly altered samples, this replacement reaction is overprinted and obscured by sericite replacement of chlorite and biotite. Retrograde metamorphic chlorite after biotite is not texturally destructive to

biotite grains. Retrograde chlorite after garnet is observed as chlorite rims on a garnet phenocryst (Figure 1.12b).

The regional metamorphism experience by the slate hornfels is difficult to determine due to the contact metamorphic and hydrothermal alteration overprinting regional metamorphism. Aluminosilicates sillimanite, andalusite, kyanite, and staurolite have not been observed. Garnet is observed only in reaction skarns of the slate hornfels in the most proximal aureoles around quartz dacite porphyry dikes. Samples ZZG18-016, ZZG18-023, and ZZG18-030 are fresh slates which are either not contact metamorphosed (ZZG18-016) or only weakly contact metamorphosed. All three samples are not conspicuously altered by hydrothermal fluids. Chlorite and illite are interpreted from SWIR spectra of these samples, which has been interpreted to be a distal alteration signature but may also represent the regional metamorphic grade of the slate as prehnite-pumpellyite to greenschist facies metamorphism.

1.7 Structural Evolution of the Zaozigou gold deposit

The structural evolution of the Zaozigou deposit occurred over multiple deformation events in an evolving tectonic regime. Complex geometries and kinematics developed as a result of changing rheologies and principal stress directions in a heterogeneous system. Deformation events likely occurred as series or pulses of tectonic activity, as opposed to discrete, individual events. The major events leading to the evolution of the Zaozigou deposit are summarized:

1. NE-SW (~030° azimuth) orogenic compression related to the initiation of closing of the Mianlue Ocean and subduction of oceanic crust of the South China Block under the South Qinling Terrane led to the development of local folding and thrusting of the Gulangdi Formation. Folds are oriented with axial planes striking NW-SE. At this time, the sediments developed a foliation parallel to the axial planes. These planar features

strike between 147 and 162 degrees and dip steeply to the SW. At this stage, the strata were overturned to their present subvertically dipping orientations. Continued NE-SW compression resulted in the development of numerous NE-SW trending faults which are interpreted to have initiated as dextral strike slip faults. The orientation and kinematics of these faults are highly variable as it is likely the faults developing at Zaozigou are related to the regional scale Xiahe-Hezuo Fault Zone. However, because the faults linking deposits in the Xiahe-Hezuo Polymetallic Zone are interpreted and not directly described, it is impossible to relate the faults at Zaozigou with structures of the Xiahe-Hezuo Polymetallic Zone.

2. Triassic magma intruded the local strata, utilizing existing fault structures as intrusion pathways. Resulting porphyritic and phaneritic dacite, quartz dacite, and diorite dikes; dike swarms; and sills are dominantly oriented in a NE-SW orientation (Figure 1.6). Dacite and quartz dacite porphyry dikes most likely were emplaced simultaneously, followed by the diorite dikes. These Triassic intrusions are crosscut by later ore-related faulting, veining, and alteration (Figure 1.11). Northeast-SW orogenic compression was ongoing with a NW-SE extensional axis that likely localized intrusions. Contact metamorphism and hornfelsing were spatially related to intrusion emplacement. The resulting conversion of slate to hornfels resulted in a rheological change of the local strata and a transition to more markedly brittle deformation.
3. Following the Triassic intrusive events was the main period of extensive faulting and brecciation which hosts vein and breccia related ores. Reactivation of previously developed faults occurred, most notably reactivation of the faults which host the Au1 and Au9 orebodies. This most likely occurred around the time of the closure of the Mianlue

Ocean, where it is possible that the South China Block's northeasterly progress was halted and far field stresses transitioned to a NW-SE right lateral transpressional regime. Effectively regional σ_2 represents local σ_1 at Zaozigou. Au1 and Au9 were thus reactivated as high angle reverse faults, and the first "M" orebodies began to form as extensional veins. Lower order faulting which also hosts vein and breccia ore occurred primarily at or near the contact between igneous intrusions and slate hornfels. The intrusion-metasedimentary contacts are marked by breccias and fault gouge.

4. Protracted cyclical development of faults and veins occurred as the Qinling Orogen continued to evolve. "Au" orebodies are typified by brecciated quartz veins, host rocks, and crushed rock/debris, whereas "M" orebodies occur as individual or laminated lodes, often with brecciated margins or tectonic striations or lineations indicating the "M" orebodies accommodated movement along their margins. Complicated crosscutting relationships occur in minor ore-related faults but are not directly observed in the major orebodies. Fault and vein styles are consistent with fault valve behavior (Sibson, 1988) related to the Au1 and Au9 high angle reverse faults. Rotation of the principal stress axis towards a more WNW-ESE orientation is interpreted based on observed crosscutting relationships and orientations of major orebodies (Figure 1.13).
5. Post-ore faulting and dismemberment of orebodies occurs. These faults strike NNE-SSW and are interpreted to be thrust faults (Figure 1.19), however the kinematics of these faults is unclear. The "Au" orebodies act as conduits for present-day meteoric fluids, as the network of faults and fractures that host these orebodies continue to the surface. In all levels of the underground mine, water percolates through the "Au" orebodies, and surface oxidation is observed. A post-ore fault acts as a lower boundary to oxidation at a relative

level of ca. 3100-3150m (Figure 1.19c). Hangingwall rocks above this fault are pervasively oxidized.

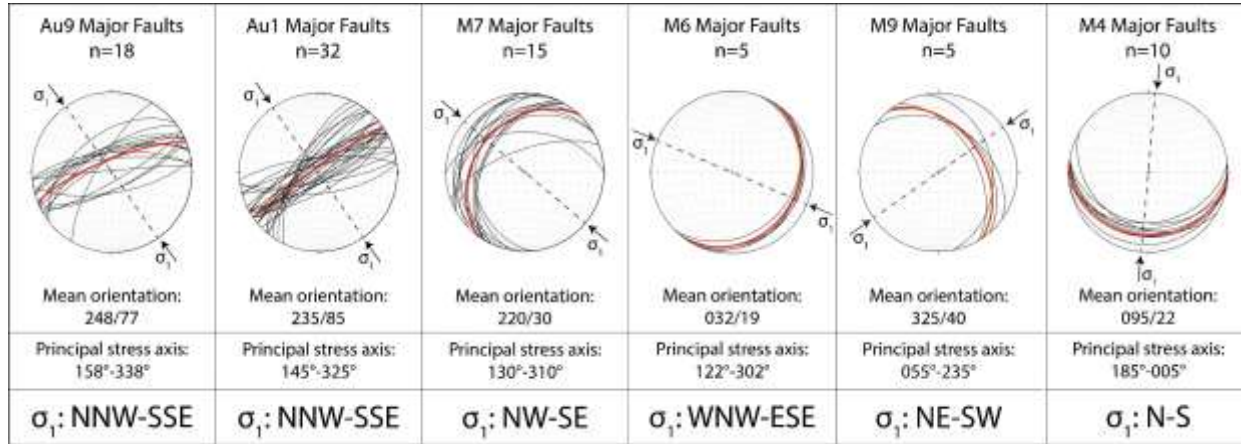


Figure 1.13. Stereographic projections of major ore-hosting reverse faults, ordered left to right from oldest to youngest. Relative timings of these structures are constrained by observed field crosscutting relationships of minor structures.

1.7.1 Early Folding and faulting (1)

Early-stage fold and thrusting at Zaozigou likely evolved in response to NE-SW compression related to the subduction of the South China Block under the South Qinling Terrane, which has been loosely constrained to the late Permian to Early Triassic. The clastic Gulangdi Slate formed as an accretionary wedge overlying the subducting slab of the SQT. Early folding and thrusting at Zaozigou occurred simultaneously, as the axial planar progression of shallowly plunging chevron folds is observed to deflect and become subparallel to NW-SE oriented reverse faults (Figure 1.14). The plunge of these structures likely occurred in response to NW-SE oriented compression which occurred later in the structural evolution of Zaozigou.

These fold and thrust structures are parallel to major regional compressional structures in the West Qinling, including the Xinpu-Lishishan anticline, Xiahe-Hezuo Fault, Guanyindazhuang-Lishishan Fault, Shangdan Suture Zone, and the western extension of the

Mianlue Suture Zone and A'nimaqen mélangé (Figure 1.3; Yan et al., 2020). These drag folds indicate fault movement in a brittle-ductile regime. Flexural slip of bedding and foliation planes leads to strain partitioning and thinning of folded strata, which then propagate into faults as the plastic limit of the rocks is exceeded.

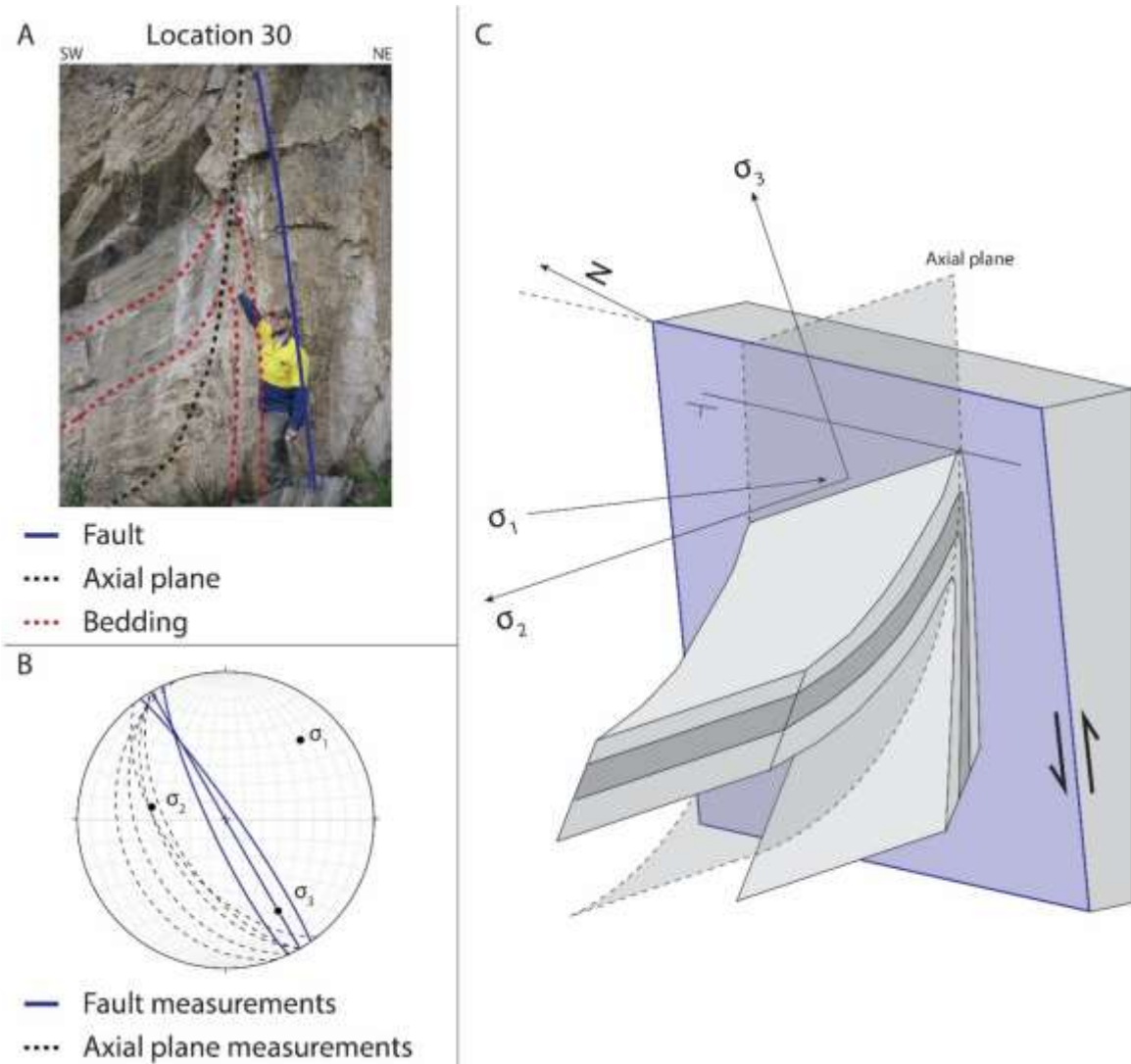


Figure 1.14. Schematic diagram describing steep reverse fault-related drag folds, which evolved under NE-SW compression. A) Location 30 photo showing traces of bedding, axial plane of drag fold, and fault. B) Stereonet projection showing orientation of measured faults, axial planes, and interpreted paleostress directions. C) Schematic cartoon diagram of the north plunging drag fold at location 30. Here σ_1 is interpreted to be shallow NW-SE compression, σ_2 extension is interpreted to be plunging $\sim 30^\circ$ west, σ_3 extension is sub-vertical.

Contact metamorphism of the slate marked a transition from ductile to brittle deformation in the immediate mine area. Folds and thrusts predating intrusion are preserved in slate hornfels (Figure 1.15). Intrusive contacts are observed where porphyry dikes intruded slates. These contacts are often not preserved and are the focus of later faulting.

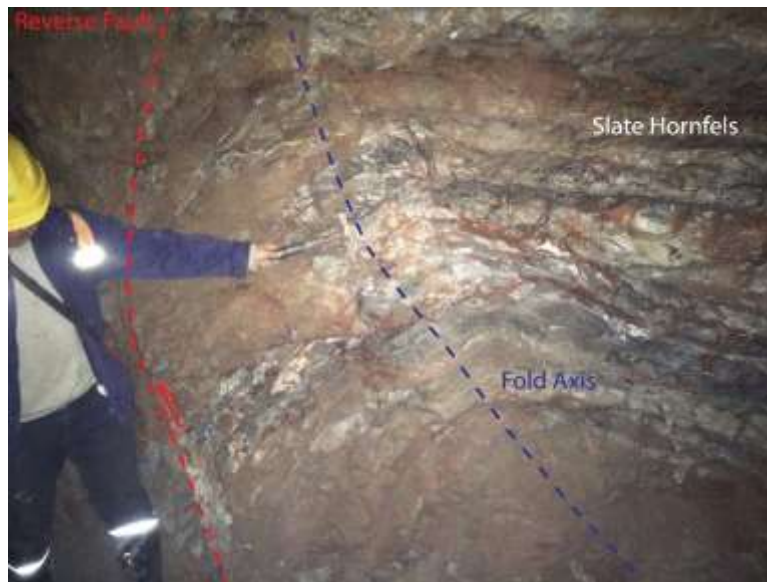


Figure 1.15. A pre-ore reverse drag fold preserved in slate hornfels.

1.7.2 Contact metamorphism (2)

The temporal development of slate hornfels caused by Triassic dacite and quartz dacite porphyry dikes marks the transition from a brittle-ductile strain regime to a brittle strain regime. The slate hornfels has lost its macroscopic foliation and fissility. Contact metamorphism caused the recrystallization of the slate's plate-like minerals. This caused an increase of the rock unit's Young's Modulus of Elasticity from an estimated ca. 30 GPa to ca. 80 GPa (based on values of typical slates and hornfels listed by Waltham, 2020).

As a direct result of contact metamorphism and conversion of the slate to a hornfels, the slate hornfels unit could accommodate more deviatoric stress, while exhibiting less strain. However, the slate hornfels is apt to rupture and fault as opposed to folding or accommodating stress through the flexural slip of bedding or foliation planes, leading the majority of ore emplacement to occur post contact metamorphism. The rocks at Zaozigou could contain higher fluid pressures approaching lithostatic pressure prior to fault rupture when supralithostatic pressures were reached. Exceeding the lithostatic pressure is associated with exceeding the plasticity of the rocks was exceeded resulting in rupturing of steep fault-fill veins, breccia zones, and shallowly dipping extensional veins. Additionally, the rheological contrast between the slate hornfels and weaker dacite and quartz dacite porphyry dikes focused faulting and vein generation at the contact between sedimentary rocks and dikes.

1.7.3 Development of main ore-bearing fault generations (3) and protracted cyclical development of faults and veins (4)

Ore-bearing faults and veins, including the “Au” and “M” structures formed or were reactivated post-intrusion of Triassic dikes. In the cases of pre-existing NE-SW trending local-scale faults, e.g. the Au1 and Au9 faults, reactivation occurred as part of a cyclical fault valve system (Sibson et al. 1988). These pre-existing faults were most likely initiated as dextral strike slip faults subparallel to NE-SW axis of compression during development of the Qinling Orogen. This is observed in the field as slickenlines or striations on quartz veins within the fault interface (Figure 1.18D). Many of these NE-SW oriented faults and fault zones have striations or slickenlines on fault surfaces which rake shallowly to the SE, such that the trend and plunge of these lineations are plunging approximately $10-20^\circ \rightarrow 240-270^\circ$ (Figure 1.18). This is observed for the Au1 and Au9 faults at surface and in mine sublevels.

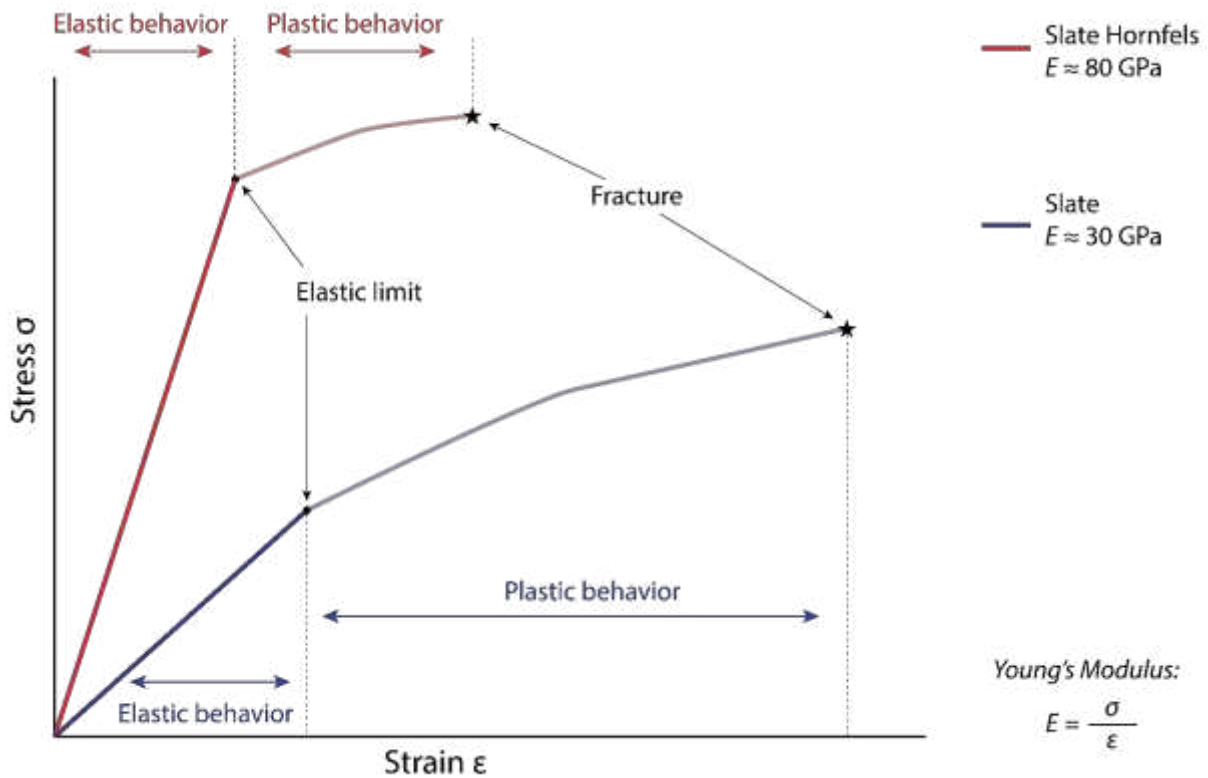


Figure 1.16. Stress-strain diagram indicating conditions for elastic, plastic, and brittle deformation of slate and hornfels. Figure is not illustrated to scale. Values for Young's modulus are from Waltham (2002).

Despite the striations and slickenlines on fault surfaces indicating NE-SW movement along the Au1 and Au9 faults, fault parallel mylonitic fabrics and internal fault structures indicate a reverse movement sense for these fault zones, which can be up to 20m wide (Figure 1.18). The kinematics of these movement indicators suggests that these high angle faults initiated as dextral strike slip faults but were reactivated as reverse faults following a change in the primary stress direction to local NW-SE compression. The change in the primary stress direction could have been related to the final closure of the Mianlue Ocean and progression of continental accretion.

During this period the tectonic regime at Zaozigou was continually evolving, with an apparent counterclockwise rotation of the primary stress axis (Figure 1.13). The contact metamorphism of slate hornfels and resultant increase of the unit's Young's Modulus raised the required stress needed to fracture the rocks. This allowed the buildup of intense fluid pressures using the high angle reverse faults Au1 and Au9 as impermeable seals in a fault valve system. When fluid pressures overcame the elevated strength of the rock, they ruptured, creating open space in a subhorizontal orientation perpendicular to the local σ_1 stress axis. Hydrothermal fluids which had been building in pressure immediately infiltrated the open space and precipitated in these "M" style. "extensional veins". The explosive release of fluid pressure simultaneously reactivates the Au1 and Au9 faults, leading to further grinding and cataclasis of breccia, rock and vein fragments, and crushed rock within the high angle reverse faults. The rupture of extensional veins leading to the propagation of "M" orebodies lowered the strength of the rock package, because following rupture of the wall rock, later reactivations of these faults would only need to overcome the strength provided by physical characteristics of the extensional veins such as the frictional force between the wall rock and extensional vein, which is dominated by the roughness of the fault surface and the angle or orientation between the primary stress axis and the fault surface. This allowed both "Au" orebodies and "M" orebodies to accommodate movement along the fault interfaces. Most "M" orebodies are observed to be laminated, shallowly dipping veins with multiple layers of coarse quartz rims and stibnite centers. Each generation of laminated quartz-stibnite vein represents a reactivation of the "M" style ore-fault (Figure 1.17).

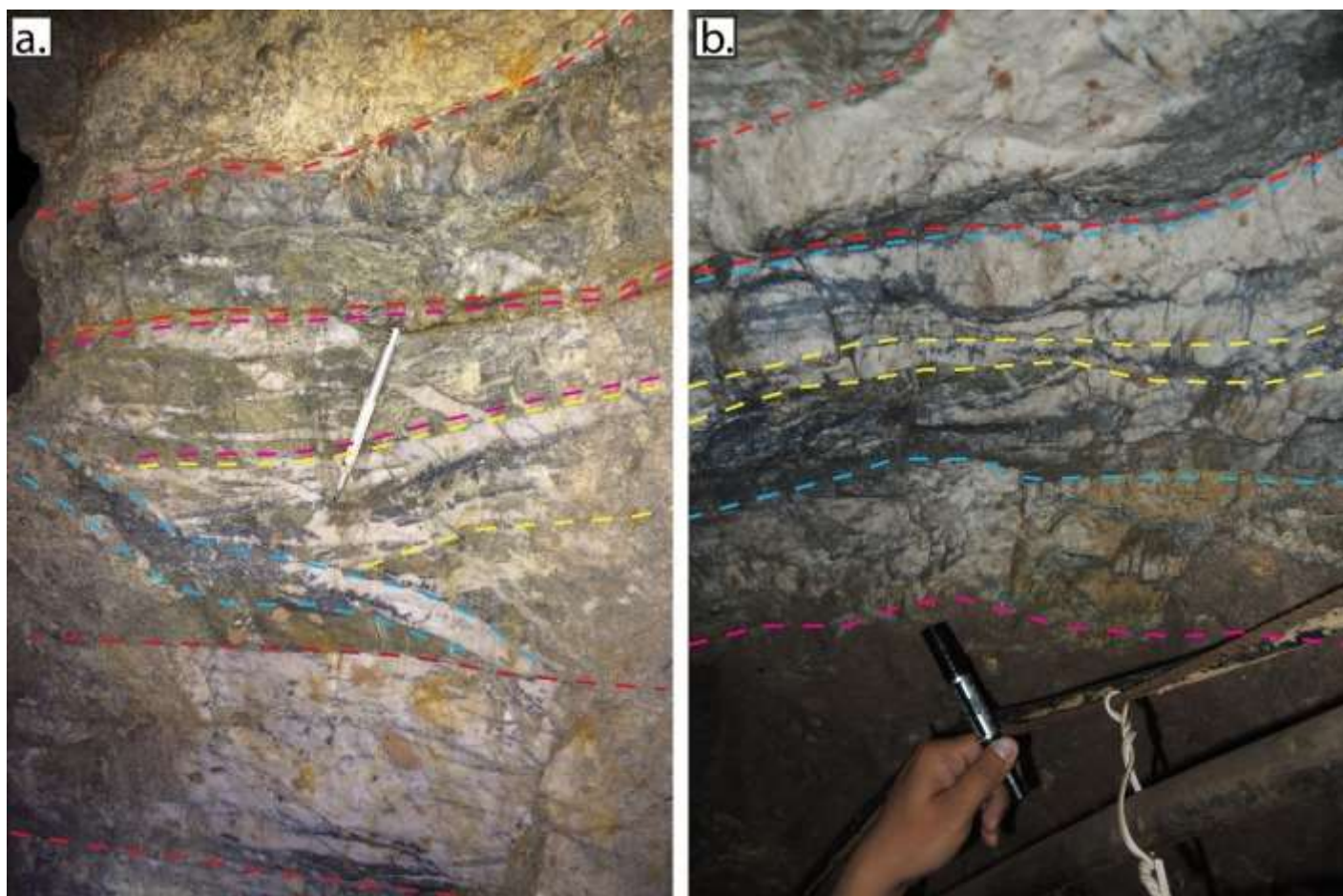


Figure 1.17. Multiple generations of extensional quartz-stibnite vein produced in “M” style orebodies. Each color dashed line represents a separate fluid pressure cycle. a.) M4 orebody photographed at mine 3146 level. b.) Au36 orebody photographed at mine 2760 level. Map shown in Figure 1.30. Au36 is perhaps mislabelled and should be characterized as a “M” style orebody, as the dip of Au36 is measured between 32 and 35 degrees, to a maximum of 40 degrees with a NE dip azimuth. The “M” style orebodies exhibit post-ore faulting and reactivation as thrust faults.

Location 26/115

A: Cross section

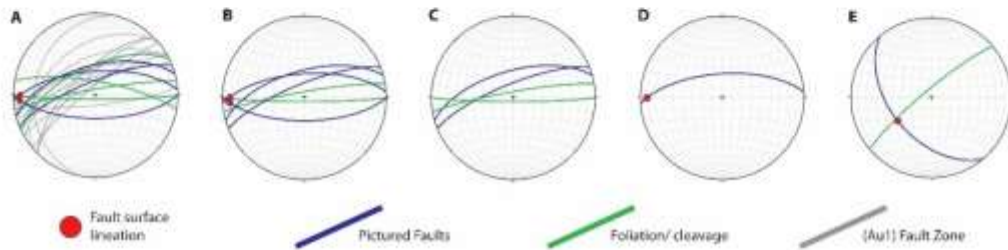
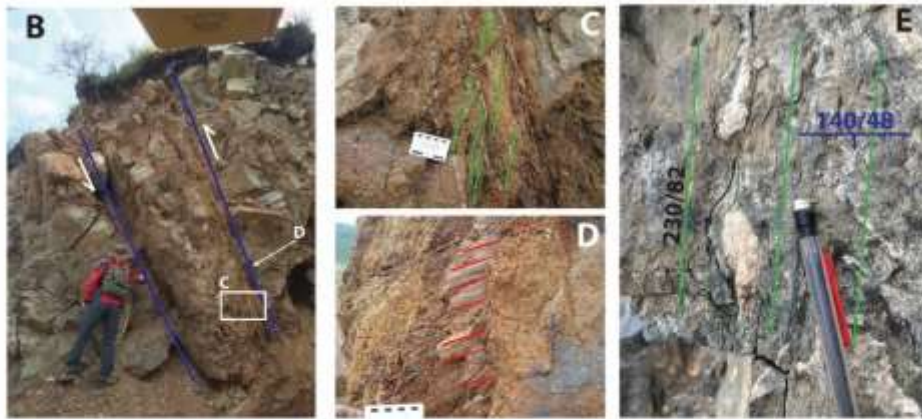
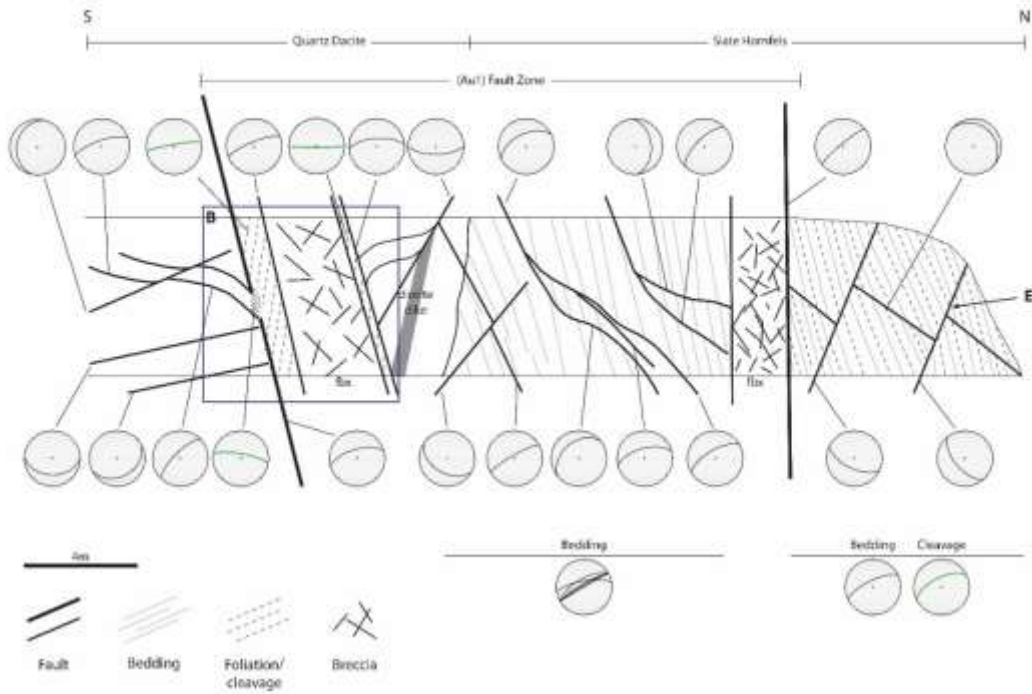


Figure 1.18. Schematic outcrop of the Au1 fault zone observed at locations 26, 115. Fault surface lineations which rake shallowly to the west on upright reverse faults indicate a period of left lateral slip. C) Fault interface proto-mylonitic foliation indicate reverse, north-up transport sense.

1.7.4 Late crosscutting faults (5)

Two significant late fault generations crosscut previously described faults, orebodies, and lithologies. At depth, a shallowly dipping series of faults is observed to crosscut and offset Au1, M9, and M6 alike. Direct observation and measurements of these structures have been made in the 2760 and 2810m level. The measurements and spatial positioning and orientation of these features is conformable across levels and assumed to be the same structure, which has a strike and dip of 193/29. Parallel structures are inferred based on similar offsets of the Au1 orebody which is also clearly evident from the underground mine plan. A separate shallow fault structure has been identified, observed, and measured in the 3146m level. This fault is oriented at 082/11 and is herein referred to as the oxide fault. Rocks in the hangingwall of the oxide fault are pervasively oxidized, whereas the footwall rocks may contain iron oxides but these occur primarily in fractures.

The deep offset faults are of unclear movement sense. Continuity of planar structures which are crosscut by the deep offset faults indicates a probable component of dextral strike slip movement. Attenuation of the Au1 orebody as observed in the 2760m level indicates a reverse component to the deep offset faults (Appendix D).

The oxide fault has been directly observed by the present study in the 3146 and 3161m levels (Figure 1.19). The oxide fault is a major thrust fault which crosscuts Au1 and Au9, transporting the hangingwall approximately 30m to the NW (Figure 1.19d). Iron oxides which stain the hangingwall of the oxide fault are primarily hematite and jarosite, suggesting that circulation of meteoric fluids late in the evolution after the emplacement of hypogene ore caused the breakdown of disseminated Fe-sulfides (pyrite, arsenian pyrite, arsenopyrite). This process

liberates refractory gold in arsenian sulfides, such as those that occur at Zaozigou (Du et al., 2020), and also generates sulfuric acid from the weathering of sulfide minerals.

1.8 Mineral Grain Deformation

The microtectonic deformation of mineral grains has been observed by petrographic microscope. Observations of stibnite crystals exhibiting deformation bands and dynamic recrystallization in “M” style orebodies show that stibnite in the quartz-stibnite extensional veins experienced post-ore tectonic stresses. Observations of quartz crystals exhibiting cataclastic deformation, microfractures, and diffusion crack healing indicate that the “M” style orebodies experienced multiple pressure cycling events. Vein quartz crystals also exhibit the development of subgrains and subgrain bulging. Calcite and dolomite crystals show type II twins. Because the microstructures developed in stibnite, quartz, and carbonate minerals occur at specific P-T conditions, the style of mineral grain deformations allow estimation of temperature of deformation at ca. 250-300°C.

1.8.1 Stibnite deformation

Where coarse grained in multi-generational reactivated quartz-stibnite veins, stibnite displays plastic microtectonic deformation fabrics. Stibnite is anisotropic under cross-polarized reflected light. This allows for observation of the crystallographic structure of stibnite. The most common features observed at Zaozigou are deformation bands. Deformation bands form during shear stress when strain is accommodated by slip along a crystal axis. Kink bands and perpendicular bands two styles of deformation band which are experimentally shown to occur in stibnite by McQueen et al. (1980). Deformation bands can be used constrain paleostress directions, and deformation bands in stibnite have been used to trace fault movement (Bellot et al., 2004). In addition to deformation bands, dynamic recrystallization of stibnite is observed at

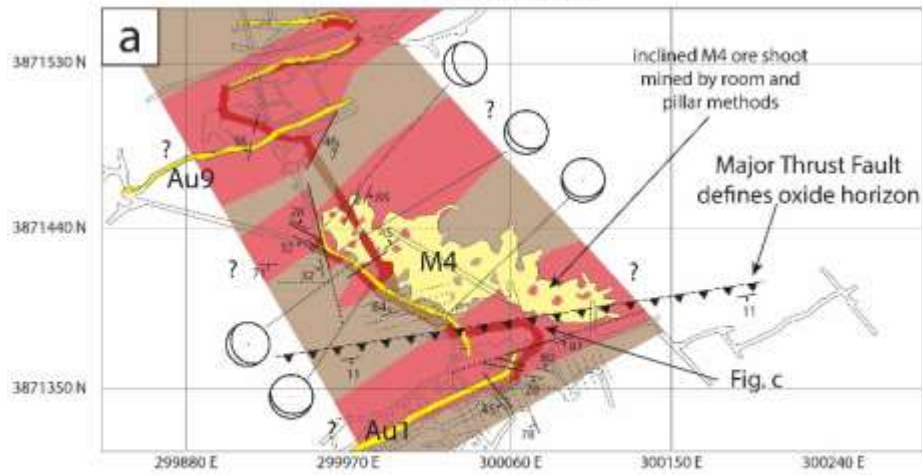
Zaozigou. Dynamic recrystallization is the process by which minerals recrystallize by the development of subgrains and the progression of grain boundary migration and subgrain rotation. In complete dynamic recrystallization, subgrains develop 120° internal angles. Dynamic recrystallization of stibnite has not been previously described in the literature. Vasil'ev (2013) describes a “granulated” stibnite occurring at the Khaidarkan Sb-Hg deposit, which may be a description of dynamic recrystallization in stibnite. Kuscu and Erler (1999) observe a similar texture, which they describe as annealing of stibnite in 120° triple junctions.

Dynamic recrystallization typically occurs during high temperature and pressure shearing. The phenomenon is most commonly used to describe recrystallized quartz and feldspar. Dynamic recrystallization can be used to constrain the pressure and temperature of recrystallization for these better-studied minerals. Experimental stibnite deformation studies have not comprehensively described the pressure and temperature conditions necessary to develop these structures. Deformation bands in stibnite have been shown to develop at temperatures $> 180^\circ\text{C}$ (Ileri, 1973), not accounting for confining pressure. Studies of other “weak” sulfides sphalerite and pyrrhotite by Clark and Kelly (1973) produced similar deformation band textures below 0.2 MPa and 300°C . Sphalerite crystals associated with stibnite in quartz veins have not been observed to display these same microtectonic features. The development of type II calcite twins further constrains the temperature of deformation to ca. $250\text{--}300^\circ\text{C}$ (Burkhard, 1993).

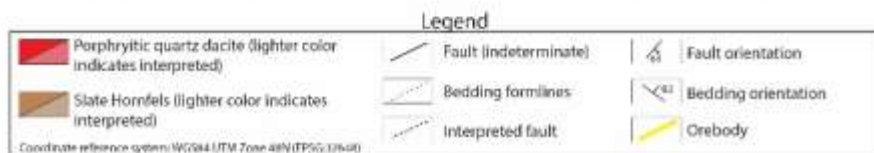
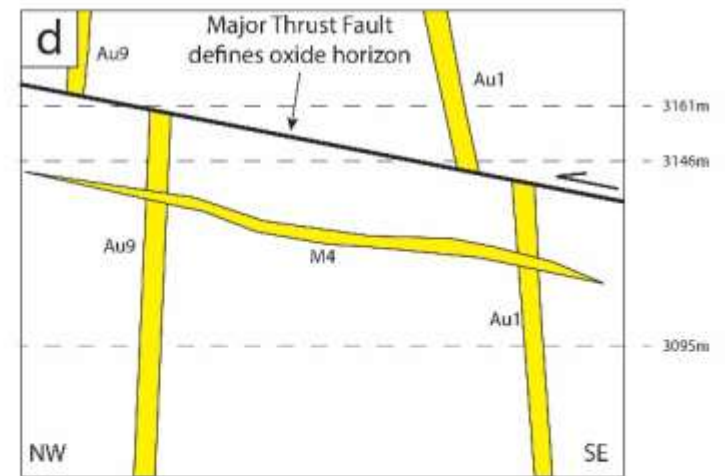
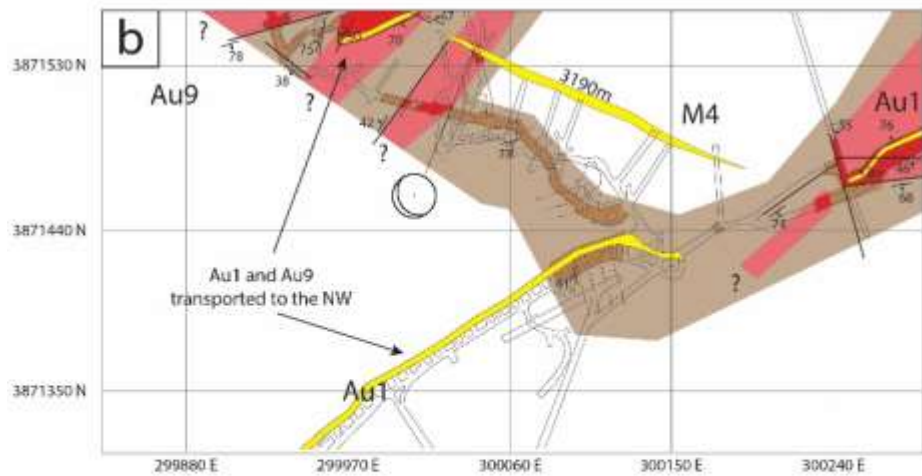
The development of deformation bands and dynamic recrystallization are syn-tectonic. Where stibnite is found with dynamic recrystallization, this is likely due to strain localization, as the regions of dynamic recrystallization of stibnite buttress quartz fragments which are relatively undeformed (Figure 1.20).

Figure 1.19 (Next Page) Fault-delineated oxide horizon is shown to be representative of a late crosscutting thrust fault which has offset Au1 and Au9 approximately 100m to the NNW. The kinematics of this fault are indicative of late NNW-SSE compression. This fault-defined oxide horizon is manifest by a plan above which country rock is pervasively stained with iron oxide. Although it has not been directly observed in this contribution, it is suspected that supergene enrichment by meteoric fluids occurred in the hangingwall of this fault, in what was originally mined at Zaozigou as an oxide gold resource.

3146m Level

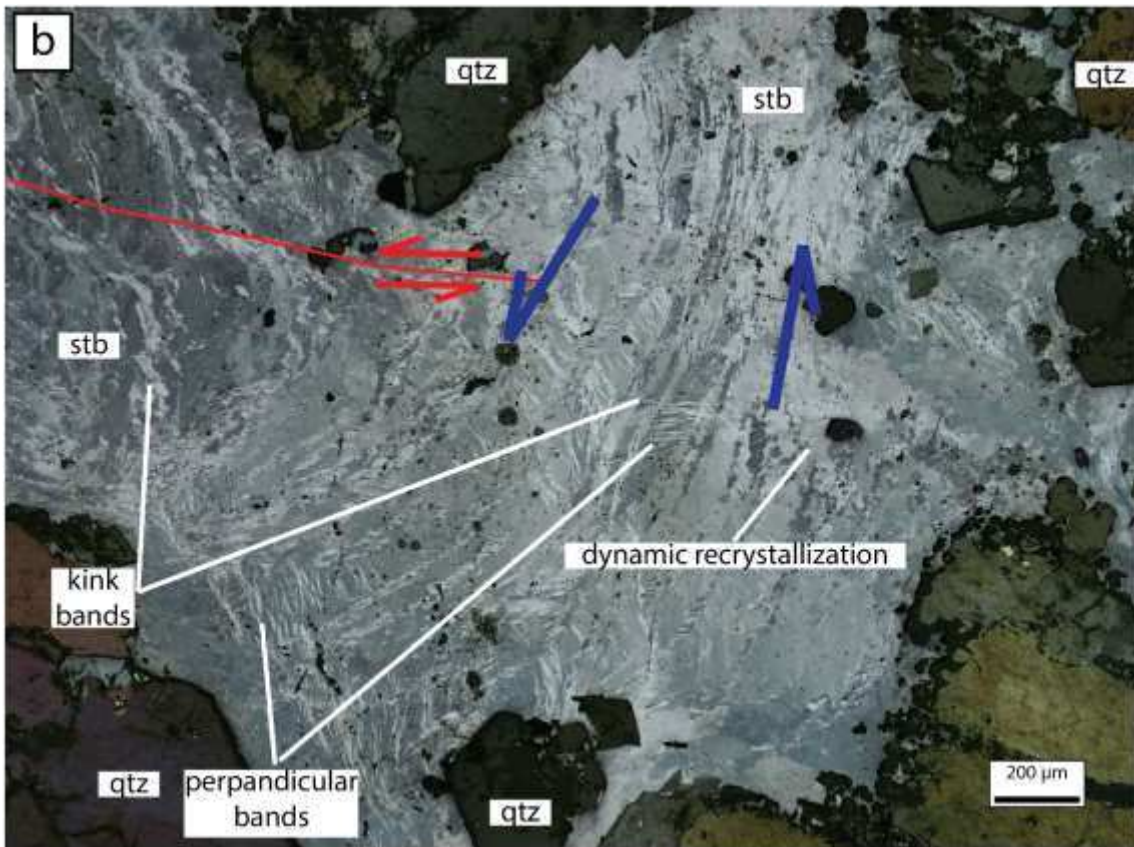


3161m Level



Schematic Cross Section Looking NE

Figure 1.20 (next page). Photomicrographs of deformed stibnite found within quartz-stibnite veins. These are reflected, polarized light images. Movement sense indicators in blue are from early generations of deformation. Red movement sense indicators indicate later deformation. Quartz fragments likely act as buttresses which promote dynamic recrystallization. Samples were not oriented. Prior to thin section preparation.



1.8.2 Quartz deformation

Quartz deformational features at Zaozigou are dominated by brittle deformation and cataclasis. Brittle deformation of quartz crystals records multiple stages of fault rupturing at Zaozigou. This is especially pronounced in “M” style quartz-stibnite vein orebodies which are associated with larger quartz crystals. Quartz crystals also developed subgrains and bulging recrystallization (Figure 1.21) which loosely constrain temperatures $>250^{\circ}$ at the time of deformation (Stipp & Kunze, 2008).

Evidence for multiple phases of quartz crystal cataclasis and following stages of fluid flow is primarily seen exhibited by the presence of healing microfractures in larger quartz crystals (Figure 1.21). These microfractures are observed petrographically as light-colored planar features within and crossing several quartz crystals. These microfractures lack the intensity of fluid inclusions which are observed within the host quartz crystal. The healed microfractures resemble stockwork vein sets and have complicated crosscutting relationships.

These healed microfractures are likely a result of diffusional crack healing within the quartz. Diffusional crack healing, as described by Smith et al., (1984), is a process of the annealing of a crystal along an existing fracture plane. Crack healing at higher temperatures and pore fluid pressures involves the diffusion of the fractured crystal resulting in the crystal being healed along the fracture plane. This is contrasted with crack sealing, which occurs when the crack is sealed by dissolved material in a fluid flowing through the crystal which is then precipitated onto the surface of the microfracture. During crack sealing, newly precipitated crystals would grow with their own crystallographic orientation, as a discretely observable new mineral crystal. As shown in Figure 1.21, healed microfractures propagate across subgrains

without disturbing the habit of the subgrains themselves and are not observed to be newly precipitated quartz crystals.

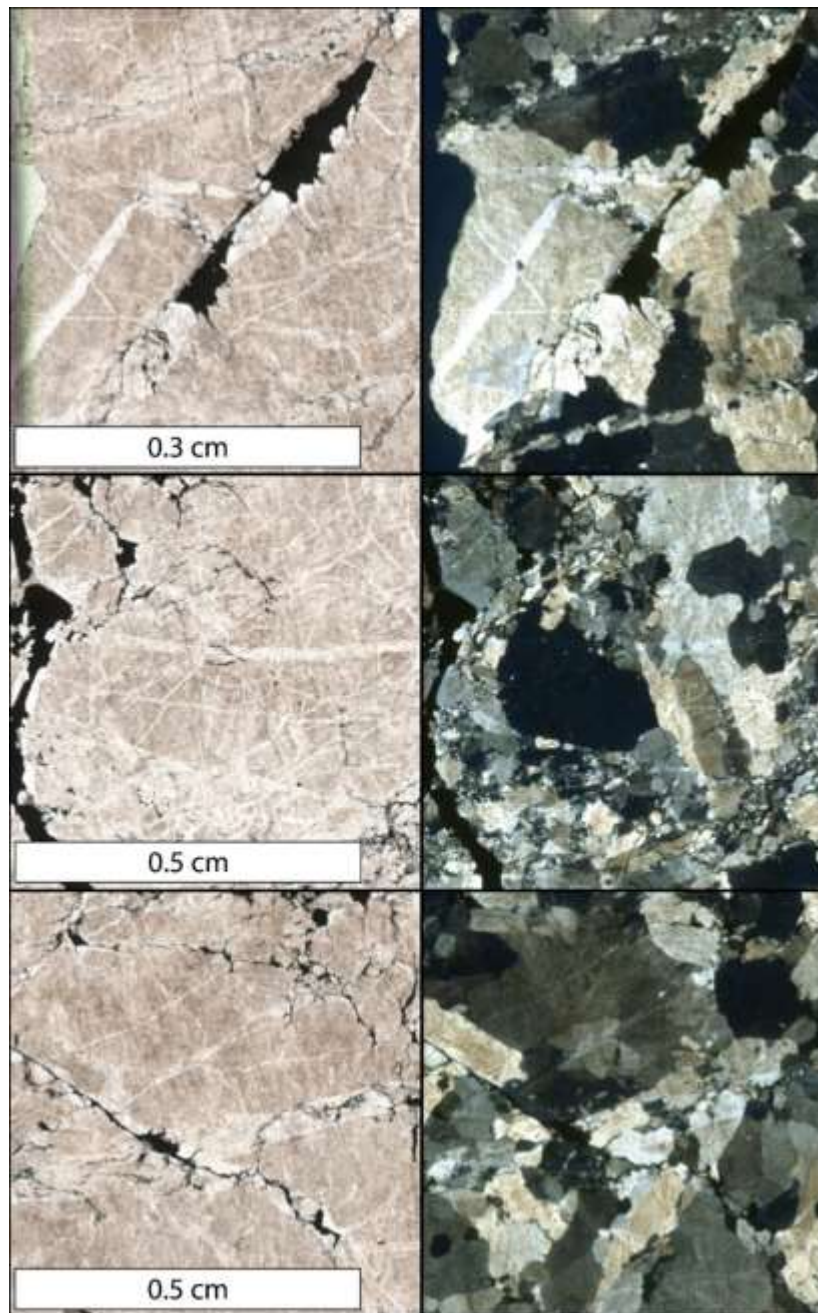


Figure 1.21. Plane Polarized and Cross Polarized photomicrographs of quartz crystals from “M” style orebody sample ZZG18-80 which exhibits diffusional crack healing. Side by side images are the same field of view. Healed microfractures propagate across quartz grain and subgrain boundaries but do not indicate new quartz crystal growth as a result of precipitation of new quartz from a fluid.

1.9 Hydrothermal Alteration

Hydrothermal alteration at Zaozigou is macroscopically observable as bleached haloes around ore-hosting quartz and quartz-carbonate veins. The width of alteration haloes is loosely dependent on the thickness of the orebody or vein around which the halo is found. Bleached haloes up to ~20m were measured in transects across the Au1 and Au9 orebodies, which were locally measured to be 5m and 3m wide, respectively. Smaller quartz-stibnite veinlets have vein to halo width ratios of approximately 1:5. The widths of bleached alteration haloes of “M” style orebodies is difficult to ascertain due to their relatively flat-lying orientations in an underground setting. Alteration halo widths were not noticeably different when observed in slate hornfels vs dikes.

Zoned alteration mineral patterns are uncommon. Quartz-sulfide (pyrite+arsenopyrite) selvages occur within bleached haloes (Figure 1.25). The intensities of bleaching and sulfidation are highest immediately proximal to the ore-hosting structures around which the alteration haloes are found. The bleached haloes are haloes of sericitic alteration. The alteration haloes extend past the macroscopically visible bleached aureole. Disseminated iron sulfides, chlorite, and illite extend past the outer boundary of bleaching. The hydrothermal alteration mineral replacement relationships are dependent on the original composition of the rock being altered, but the hydrothermal alteration minerals do not vary significantly between lithologies. Hydrothermal alteration in the quartz dacite porphyry dikes is dominated by (NH₄) illite replacing biotite, chlorite, and feldspar phenocrysts and arsenopyrite-pyrite replacement of biotite and chlorite. Hydrothermal alteration in the slate hornfels is dominated by (NH₄) illite replacement of diagenetic clays and arsenopyrite-pyrite sulfidation of the Fe-rich layers.

Hydrothermal alteration at Zaozigou can be broken into five main styles of alteration: sericitic/bleaching alteration, carbonate alteration, chlorite alteration, sulfidation and silicification. Sericite species are predominantly illite, ammonium illite (NH₄-illite), muscovite, and halloysite. Alteration mineralogy, especially of sericitic and clay species, was primarily interpreted from SWIR analysis.

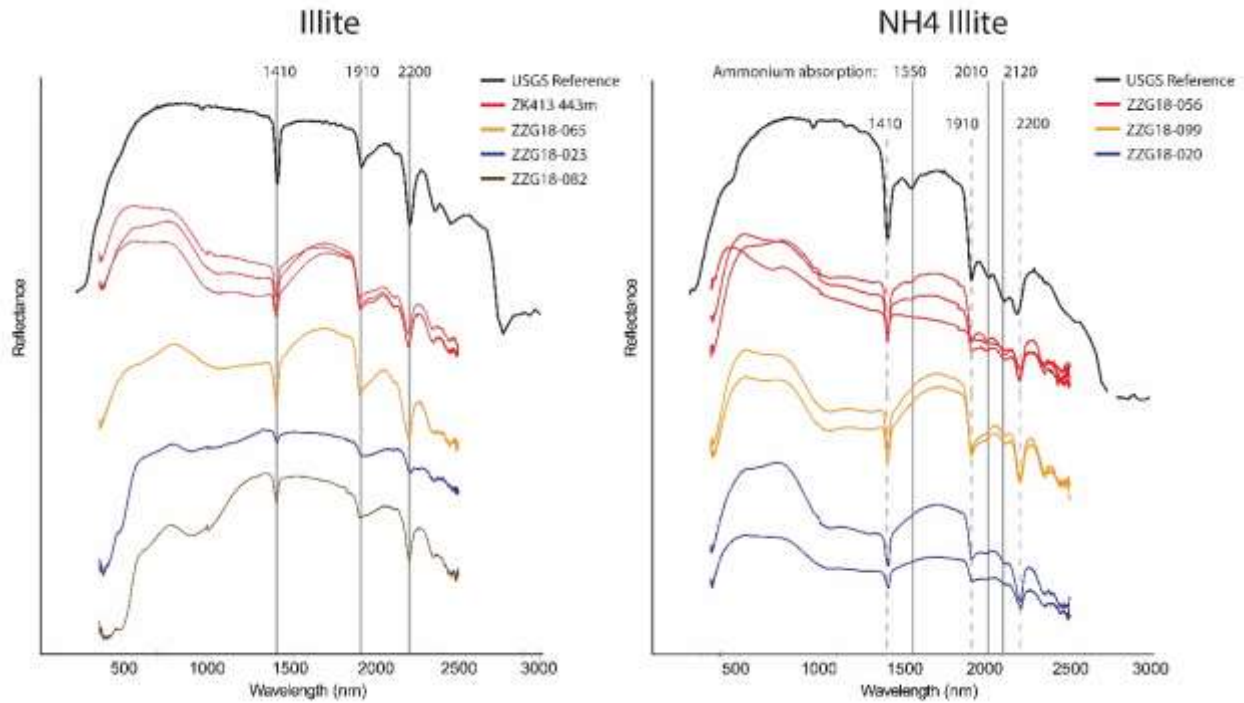


Figure 1.22. Stacked SWIR reflectance spectra of samples which host illite and NH₄ illite as hydrothermal alteration minerals compared with USGS reference spectra (Kokaly et al., 2017). Solid gray vertical lines correspond with diagnostic absorption bands for the respective mineral species. Dashed gray lines in NH₄ illite diagram correspond to illite diagnostic absorption bands to illustrate these are the same mineral group. Illite diagnostic absorption spectra wavelengths from Chang et al., 2012. NH₄ illite diagnostic absorption spectra (ammonium ion IR absorption) from Ferrari et al., (2019); Godeas and Litvak, (2006).

SWIR analysis of samples has led to the identification of two dominant sericite species: illite and NH₄-illite (Figure 1.22). Illite and NH₄-illite average Al-OH absorption trough of all samples analyzed was found at 2204 nm. The Al-OH absorption band does not exhibit a strong

correlation with the distance to the proximal vein, orebody, or mineralized structure (Figure 1.23). There is also no observed zonation pattern relating the Al-OH position of illite and NH₄-illite with the depth of the analyzed sample (Figure 1.24). The Al-OH position of both illite and NH₄-illite range from 2200 to 2208 and 2210 nm, respectively. This may be reflective of locally more paragonitic (Na) or phengitic (K, Fe, Mg) illite species, or may be a reflection of the preceding mineral that was altered, i.e. illites and NH₄-illites with lower Al-OH positions may be replacements of Na-enriched mineral phases (plagioclase, montmorillonite, etc), and the higher Al-OH positions are measured from replacements of more K, Fe, Mg-enriched phases (k-feldspar, biotite, kaolinite, etc).

1.9.1 Hydrothermal alteration of slate hornfels

Hydrothermal alteration in the slate hornfels at Zaozigou is primarily observed to occur as bleaching. In its unaltered state the slate hornfels is composed of dark and light interbedded sedimentary layers (Figure 1.8). Bleaching is the manifestation of intense sericite alteration and results in a color change to a buff brown to greenish brown color (Figure 1.41a-c). Alteration is texturally destructive resulting in the loss of identifiable bedding and foliation. Alteration minerals in the slate hornfels have been identified and interpreted based on SWIR and petrographic analysis. The most common minerals identified by SWIR in slate hornfels at Zaozigou are kaolinite, illite, NH₄-illite, and chlorite (Figure 1.27). SWIR analysis of slate and slate hornfels samples which were absent of obvious bleaching (samples ZZG18-023, 030, 052, 072, 073, 084) resulted in primarily the identification of illite, chlorite, kaolinite, and halloysite. Since SWIR spectra are unable to directly determine whether the identified minerals are products of hydrothermal alteration, kaolinite and halloysite are interpreted to be products of supergene weathering.

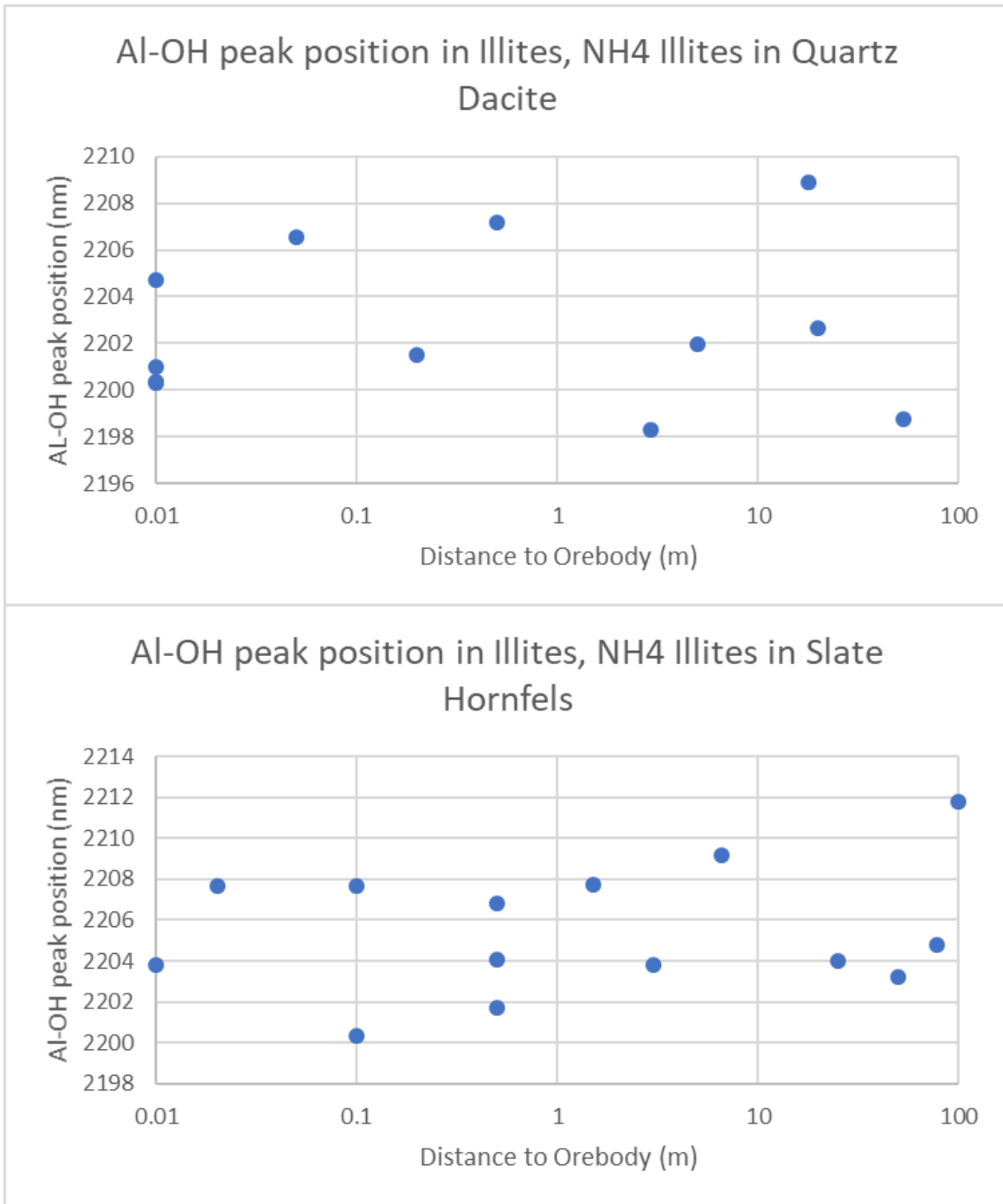


Figure 1.23. Peak position of Al-Oh absorption bands measured in illites and NH4-Illites analyzed by SWIR and segregated by lithology (quartz dacite and slate hornfels) plotted versus distance to the nearest proximal orebody. The peak position of Al-Oh in illites hosted in illite alteration of quartz dacite is consistently above 2200 nm, in the range from 2200-2212 nm. The Al-Oh absorption peak in measured slate hornfels ranges from 2198 to 2209 nm. In both lithological cases, there is no discernible trend showing a distance-dependant Al-Oh peak position.

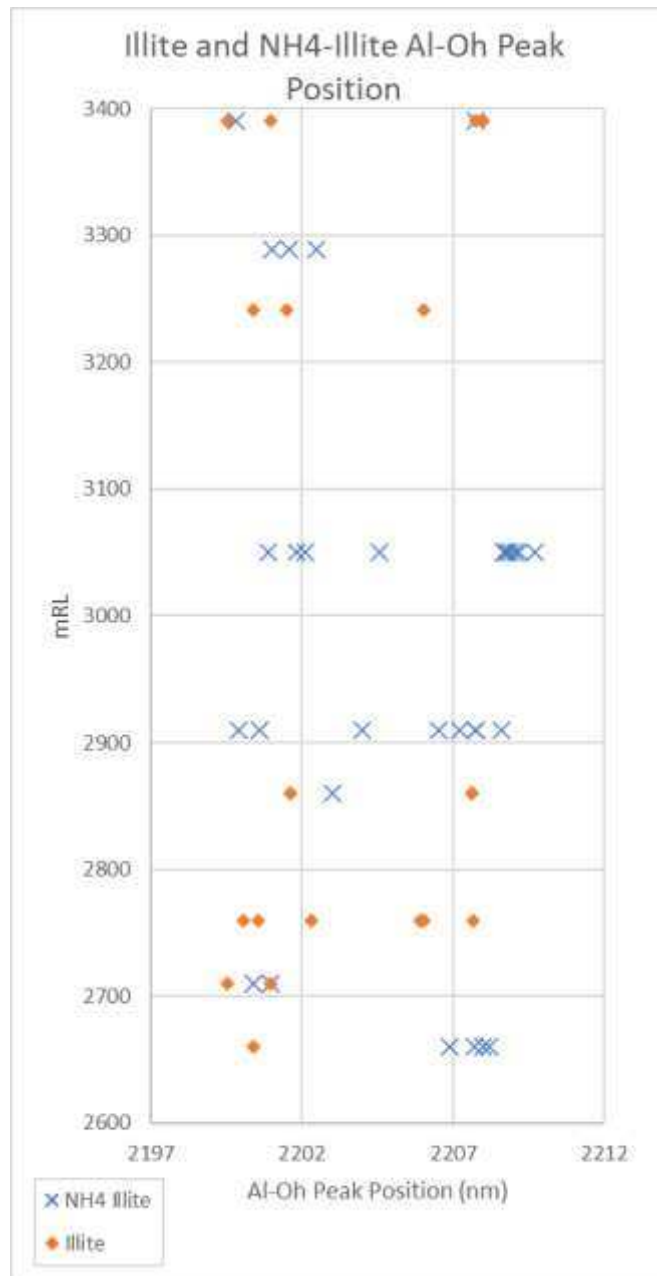


Figure 1.24. Al-OH (2200 nm) absorption peak positions measured in SWIR spectra for samples identified to contain Illite and/or NH₄-Illite, plotted against the relative level (geographical elevation) of the samples collected. Al-OH position of Illites (including Illite in slate hornfels, diorite, and quartz dacite) ranges from 2200 nm to 2208 nm. Al-OH position of NH₄-Illites (including NH₄-Illite in slate hornfels, diorite, and quartz dacite) ranges from 2200 to 2210 nm. No clear trend is observed of spatial variation of the Al-OH absorption peak as a function of depth in the system. Al-OH peak position in Illites is linked with chemical composition. Al-OH peaks closer to 2200 are generally more sodic, and peaks trending to 2210 are more potassic (Halley, 2010). Figure 1.23 shows that there is no clear trend in lithological control or the distance to the proximal orebody or mineralized structure.

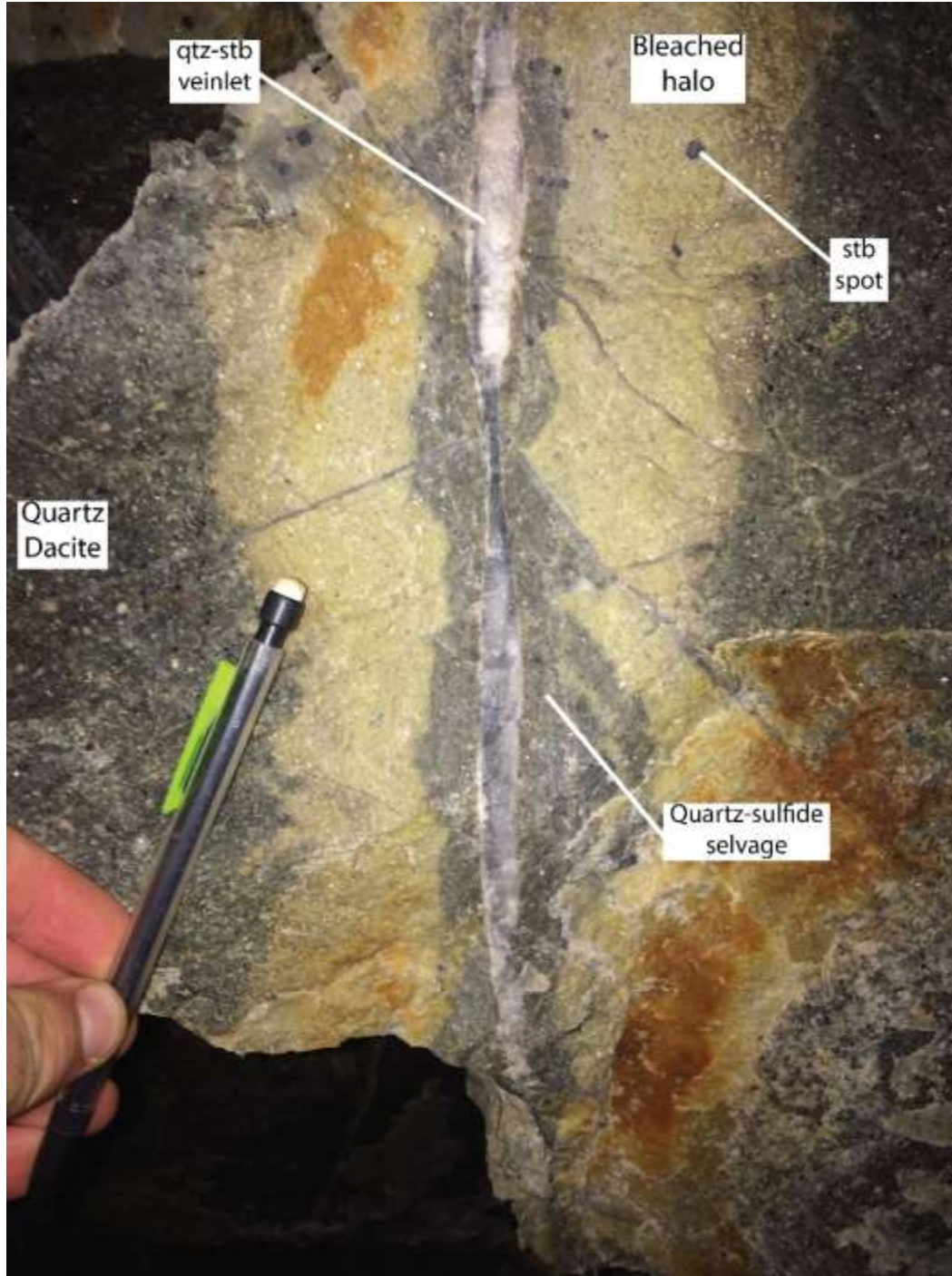


Figure 1.25. Quartz-sulfide selvage mantling a quartz-stibnite vein hosted in quartz dacite. This occurs coeval with the bleached halo. It is likely the quartz-stibnite vein pictured was a conduit for multiple generations of fluid flow. Quartz phenocrysts of the quartz dacite porphyry are preserved as quartz “eyes”. Feldspar phenocrysts are replaced by illite and ammonium illite within the bleached halo.

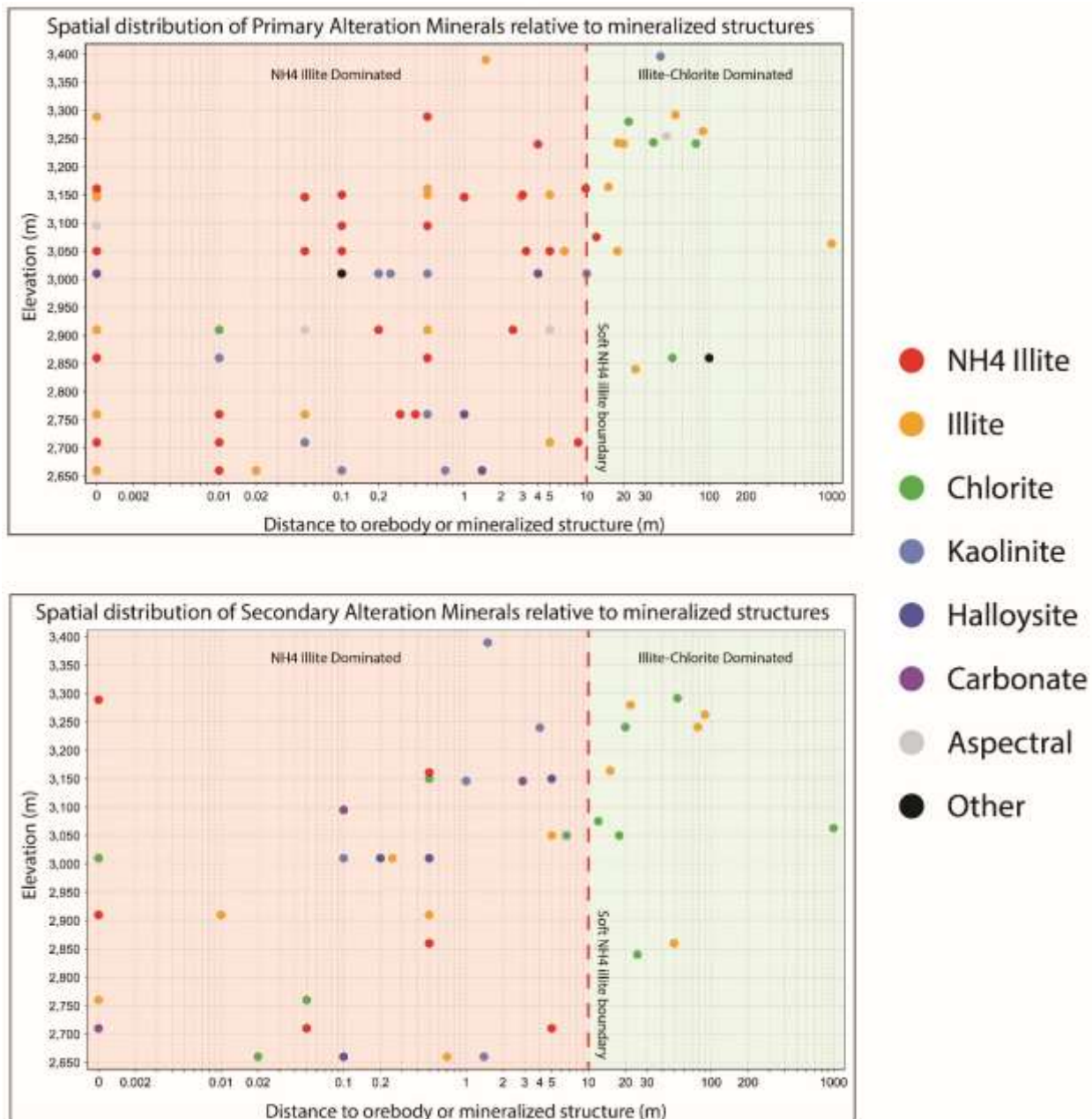


Figure 1.26. Spatial plots of dominant and secondary alteration minerals identified by SWIR, relative to proximal orebodies or mineralized structures. NH4 Illite is almost exclusively found within 10m of a mineralized structure, as demonstrated by the soft NH4 Illite boundary. Alteration assemblages at Zaozigou generally follow a spatial zonation of NH4 Illite-Illite, Illite, Illite-Chlorite. Kaolinite and Halloysite also show a close spatial association with mineralized structures, which is interpreted to be predominantly due to the steeply dipping faults acting as conduits for late, acidic, meteoric fluid circulation not directly related to hypogene ore deposition, but possibly related to supergene remobilization and enrichment.

Ammonium illite has been shown to preferentially replace kaolinite in laboratory studies (Sucha et al., 1998). NH_4 -illite found in slate hornfels is likely to be a replacement of kaolinite. The relatively low frequency of NH_4 -illite observed by terraspec, combined with NH_4 -illite's increased stability over kaolinite in hydrothermal conditions and the frequency of NH_4 -illite in analyzed quartz dacite porphyry samples suggests that NH_4 -illite is not a diagenetic component of the local slate hornfels, but is instead introduced by N-rich hydrothermal fluids. Carbonate alteration in the form of calcite and ankerite occur in minor amounts within slate hornfels, especially adjacent to veins which host ore minerals.

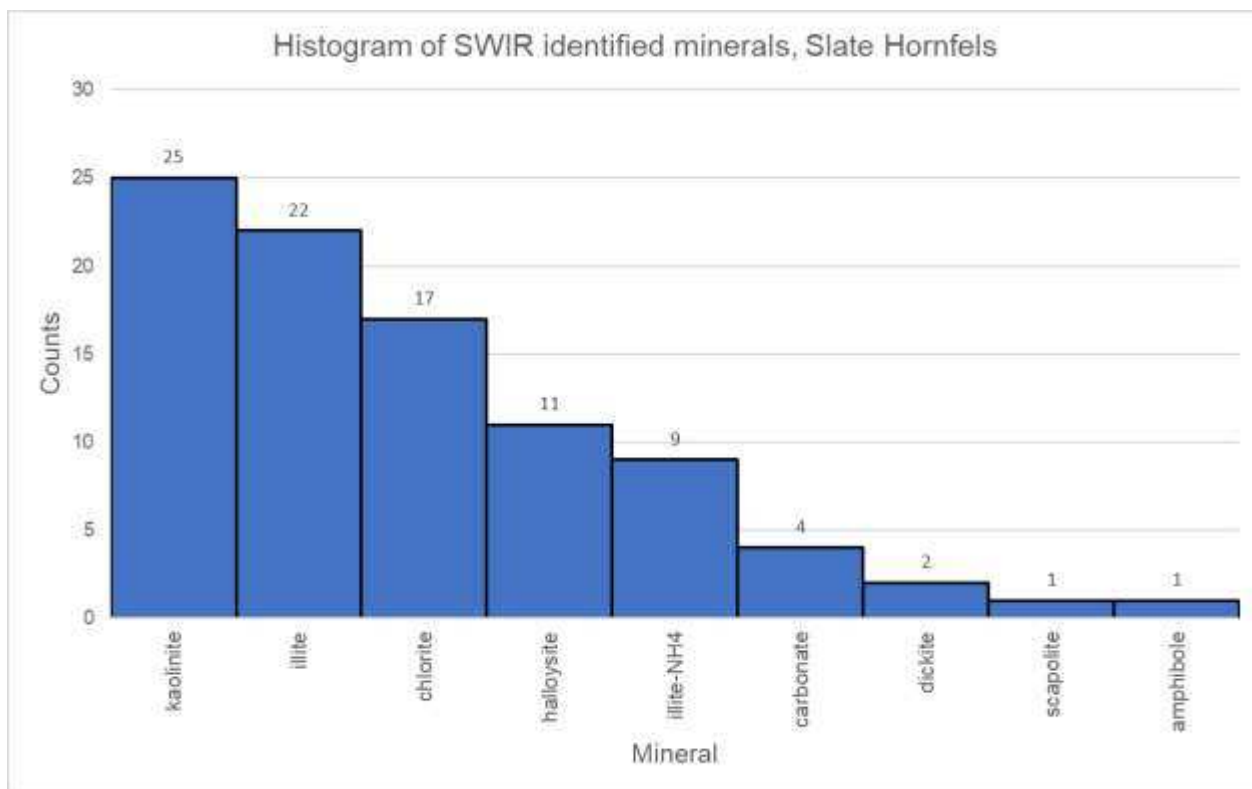


Figure 1.27. Histogram of alteration-related minerals in Slate Hornfels samples, identified using Terraspec. Illite species (Illite and Illite NH_4) constitute the most commonly observed alteration minerals (n=31), followed by kaolinite and halloysite.

1.9.2 Hydrothermal alteration of quartz dacite porphyry

Sericitic alteration of quartz dacite porphyry dikes is the most commonly observed alteration style to affect this unit. Sericite replaces plagioclase and biotite phenocrysts. It is likely that chlorite replacement of biotite phenocrysts was an intermediate step, as chlorite replacement of biotite can be seen clearly in thin sections of weakly altered quartz dacite porphyry samples. Illite is the dominant sericite species. In the strongest zones of sericitic alteration, illite completely replaces plagioclase phenocrysts, often maintaining the lathlike habit of feldspar crystals. Illite replacement of biotite is often accompanied by or superseded by muscovite replacement.

Ammonium illite has been identified in 14 quartz dacite porphyry samples by SWIR (Figure 1.29). Ammonium illite and illite have not been distinguished during petrographical examinations. Due to its similarity to the K^+ ion, NH_4^+ preferentially replaces potassium, especially in feldspars and micas.

Sericitic replacement of biotite has also been shown to be important for the precipitation of pyrite and arsenopyrite in altered quartz dacite porphyry ores. Replacement of biotite by sericite (illite and muscovite) liberates Iron and Magnesium from biotite and chlorite. The Iron can then react with Sulfur and Arsenic carried by the hydrothermal fluid to precipitate pyrite and arsenopyrite. Magnesium may be remobilized and precipitated in cracks as dolomite.

Rutile and zircon are also liberated by the sericitic replacement of biotite (Figure 1.28). The rutile and zircon were likely contained as inclusion within the unaltered biotites. These liberated zircons and rutiles may have useful future applications for thermobarometry and geochronology.

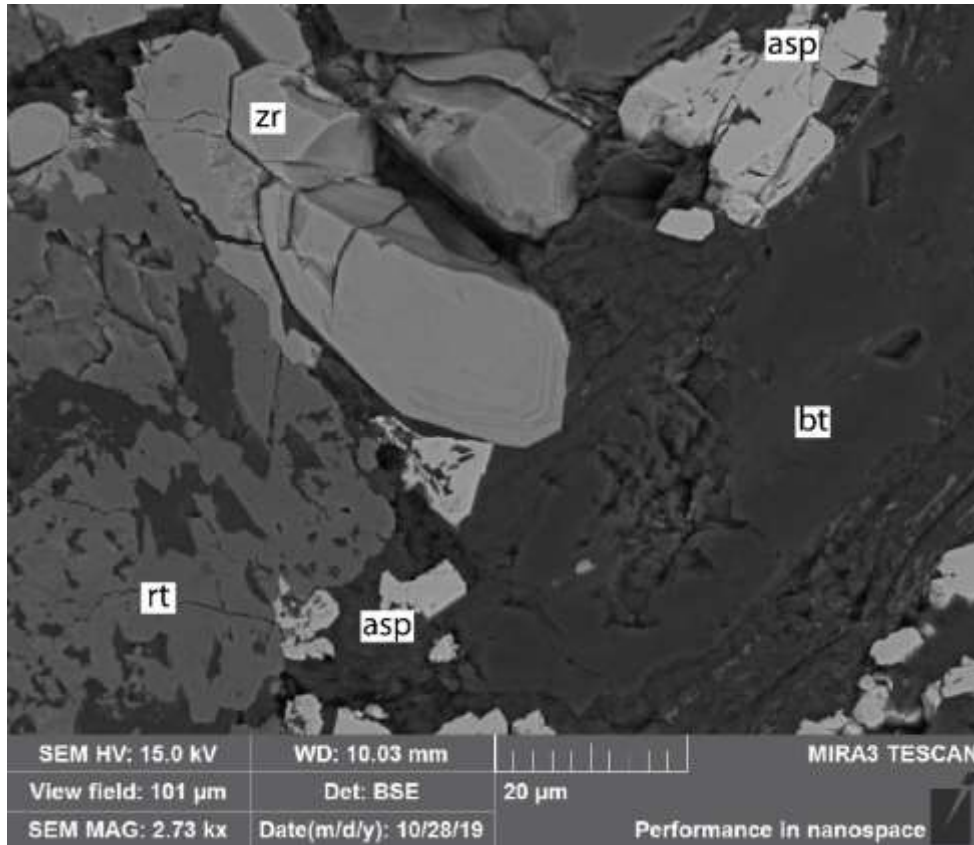


Figure 1.28. Arsenopyrite replacement of biotite in quartz dacite. Zircon and rutile also precipitate as a result of the liberation of Ti and Zr. Rt = rutile, zr = zircon, asp = arsenopyrite, bt = biotite.

Kaolinite is a minor alteration product but is seen more frequently and in higher proportions in samples taken from shallow levels of the mine, especially above the 3146 level, where a mapped fault serves as the lower boundary for a widespread supergene environment. Kaolinite is more likely a result of supergene weathering due to late circulation of meteoric fluids through the main stage ore-hosting structures.

Hydrothermal alteration haloes in quartz dacite porphyry dikes are notably narrower than alteration haloes in slate hornfels. Macroscopic hydrothermal alteration can be seen as bleaching up to 20 m transverse from large, fault-hosted, quartz-stibnite ore zones which are on the order of 3-5m width.

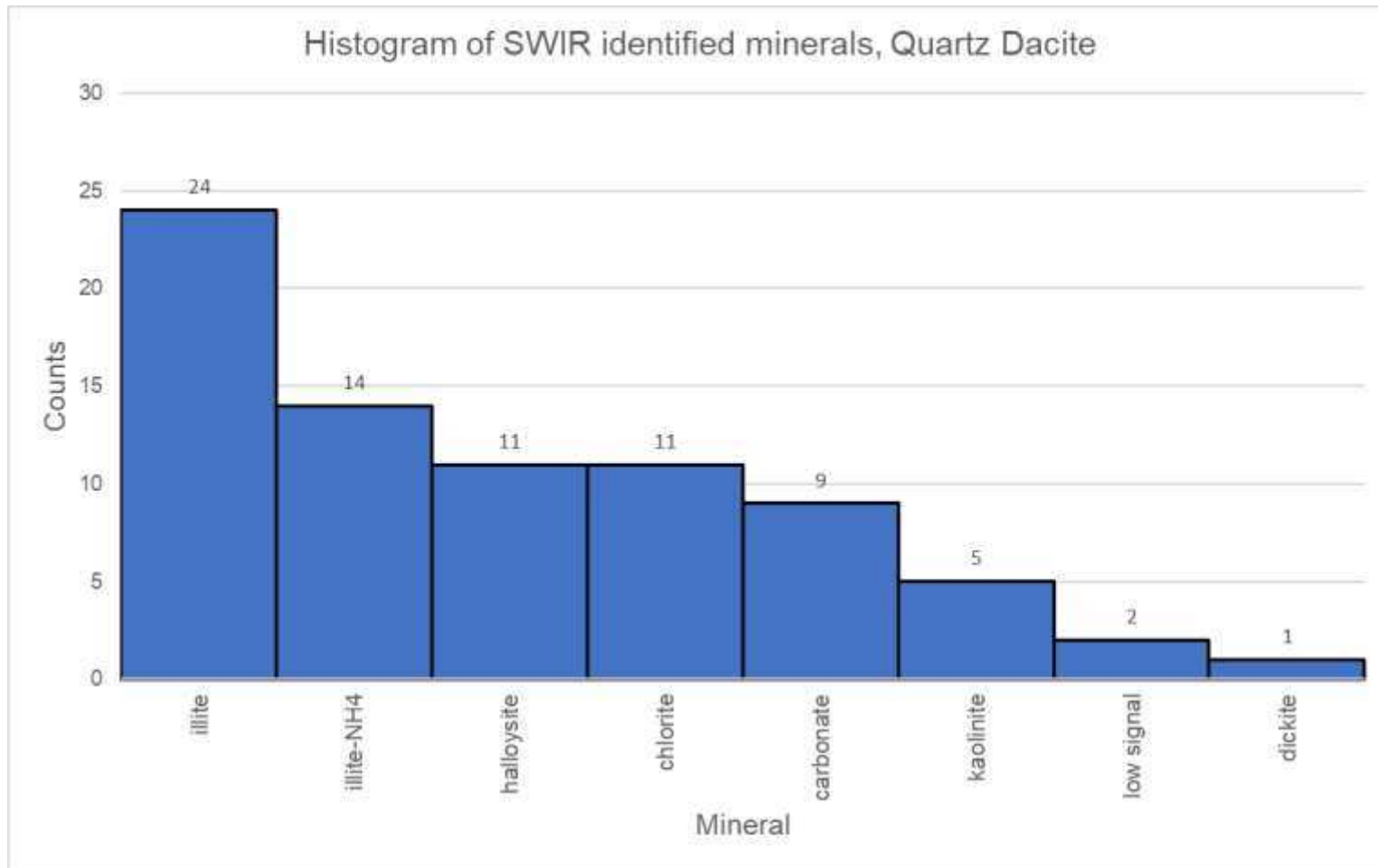


Figure 1.29. Histogram of alteration-related minerals in Quartz Dacite samples, identified using Terraspec. Illite species (Illite and Illite NH₄ constitute the most commonly observed alteration minerals (n=24, n=14), followed by halloysite and chlorite.

Figure 1.30. (Next Page) Spatial variation of hydrothermal minerals identified through SWIR. NH₄-Illite is identified in wall rock of both slate hornfels and quartz dacite directly in contact with Au36 ore-bearing fault, which in this location is oriented with strike and dip of 320/27. Here Au36 is found as a quartz-stibnite “extensional” vein with a narrow bleached alteration halo hosting disseminated arsenopyrite and pyrite. A visual gradient into fresher rock is conspicuously observed vertically above and below the fault-hosted orebody. This visual transition is substantiated by a transition of dominant clay species in slate hornfels from NH₄-Illite to Halloysite, and in Quartz Dacite as a transition from NH₄-Illite to Illite and Chlorite. The plan map to the right gives context to this location at the access portal to an ore extraction incline. The incline closely follows the Au36 orebody and would later transition to becoming a room-and-pillar style ore extraction site. Au36 juxtaposes hangingwall slate hornfels above footwall quartz dacite. It is unknown how much transport has been accommodated by the Au36 fault. Au36 vein is laminated, suggesting multiple pulses of movement and mineralization along. The Au36 is significantly offset by a crosscutting fault zone of apparent right lateral and reverse kinematics. The same fault crosscuts the Au1 orebody over multiple mine levels (Appendix D).

Geochemical zonation patterns reflect a decrease in Na proximal to hydrothermal fluid sources. This is due to the remobilization of Na ions during the replacement of plagioclase. Na is a highly mobile element, not found in significant quantities in other quartz dacite minerals. Na depletion is a useful indicator for high grade mineralization, as Na content is inversely correlated with the gold grade in quartz dacite porphyry samples.

1.10 Bulk Rock Geochemistry

A total of 31 samples collected at Zaozigou were selected for bulk rock geochemical analysis. Details on the analysis are found in Appendix E, and results are summarized in Table 1.1. The selected samples included unaltered protoliths, altered host rocks, and vein ore samples. Samples ZZG18-016, -023, 030, 150, and 151 are the unaltered protoliths and used as comparisons for geochemical changes experienced by host rocks affected by hydrothermal alteration and ore emplacement. Gold ranges from 1 ppb in an unaltered slate sample to 56521 ppb in a brecciated quartz-stibnite vein ore sample from the Au1 orebody. Quartz-stibnite vein ore hosts the highest-grade gold analyzed. The average gold grade of the 9 samples of vein ore is 19,537 ppb Au. The average gold grade of the 6 altered slate hornfels samples analyzed is 2936 ppb Au. The average gold grade of the 5 altered quartz dacite porphyry samples is 4420 ppb Au.

Altered host rocks enriched in gold are also enriched in arsenic up to and exceeding the 10,000 ppm reportable limit. All altered host rocks which are enriched in Au (>1000 ppb) and As (>300 ppm) have Na₂O analyses below or at the analytical detection limit. K₂O is enriched in samples containing high As but not in samples containing high Sb. Samples containing high Sb are depleted in all major oxides except SiO₂ due to the context of these samples being collected from veins and being mostly absent of wall rock material.

Table 1.1. (Four pages) Major and trace element concentrations from surface and underground transects at Zaozigou. S = surface, SH = slate hornfels, VO = vein ore, B = breccia, QD = quartz dacite porphyry, OB = ore breccia, VBS = brecciated ore with slate hornfels lithic clasts, Dio = diorite porphyry

Sample	Proximal Orebody	Dist. Orebody	Lith	SiO2	Al2O3	FeTOT	MgO	CaO	Na2O	K2O	TiO2	P2O5	MnO	Cr2O3	LOI	TOT/C	TOT/S
		m		%	%	%	%	%	%	%	%	%	%	%	%	%	%
ZZG18-																	
016	S	-	Slate	60	17.45	6.69	3.22	3.63	2.41	3.2	0.7	0.17	0.05	0.012	2.2	0.07	0.01
023	S	-	Slate	55.24	13.28	6.16	2.65	7.96	1.91	1.97	0.65	0.18	0.17	0.011	9.6	2.03	0.01
030	S	-	SH	50.2	17.62	6.64	3.22	14.09	1.79	3.06	0.65	0.14	0.08	0.014	2.2	0.39	0.03
041	Au1	0	VO	18.96	0.48	1.57	3.67	7.42	0.03	0.08	0.02	0.02	0.04	<0.002	14.1	2.83	17.29
048	Au9	0	B	43.77	7.63	5.02	0.9	20.61	0.01	2.13	0.26	0.05	0.08	0.006	19.1	4.86	2.68
049	Au9	0	VO	18.4	10.5	5.79	9.31	22.26	<0.01	1.88	0.29	0.05	0.08	0.007	31.2	7.97	1.47
050	Au9	0.1	SH	39.93	14.67	5.27	4.03	13.6	0.02	2.53	0.51	0.12	0.09	0.01	19	4.58	1.14
051	Au9	5	SH	51.49	15.37	3.83	2.03	10.72	0.03	2.26	0.6	0.14	0.06	0.011	13.2	2.55	0.15
055	Au1	0	VO	94.62	0.41	0.76	0.62	1.25	<0.01	0.02	<0.01	0.03	0.01	0.003	1.9	0.48	0.12
056	Au1	0.1	QD	58.82	15.78	3.7	2.57	4.52	<0.01	3.47	0.55	0.13	0.07	0.007	10.2	1.79	1.22
057	Au1	0	VO	89.11	0.46	0.63	0.61	1.07	0.01	0.08	<0.01	0.03	0.02	0.002	2.3	0.44	2.1
059	Au1	0	QD	70.87	7.88	2.92	2.76	4.75	<0.01	1.71	0.29	0.07	0.03	0.002	8.6	1.92	1.03
060a	Au1	0	VO	67.56	0.21	0.85	1.83	3.08	0.01	0.02	<0.01	0.02	0.03	0.002	6	1.22	7.11
065	Au1	0.1	QD	26.37	7.09	4.48	10.23	20.64	<0.01	1.04	0.25	0.05	0.08	0.002	29.6	8.08	0.87
068	Au1	0.15	SH	51.55	17.17	6.09	2.6	5.62	0.03	2.78	0.65	0.15	0.09	0.011	13	2.38	2.1
070	Au1	0	OB	63.44	10.82	5.21	2.65	4.48	<0.01	2.55	0.41	0.08	0.07	0.008	10.1	1.86	2.07
072	Au1	20	SH	46.76	14.29	5.64	3.13	17.46	1.13	1.92	0.55	0.13	0.18	0.01	8.6	2.03	0.14
074	M9	0	VBS	83.73	5.16	1.13	0.6	0.82	0.02	1.3	0.2	0.04	0.02	0.009	2.8	0.37	1.72
075	M9	0.1	SH	56.85	18.05	5.25	2.11	2.82	0.01	3.57	0.74	0.19	0.09	0.014	9.8	1.46	0.54
076	M9	5	SH	52.63	18.19	6.63	2.44	3.32	0.02	5.01	0.75	0.08	0.06	0.014	10.6	1.48	2.6
078	M9	5	QD	66.32	16.27	4.3	1	1.05	<0.01	4.11	0.55	0.07	0.02	0.004	6.1	0.41	1.92
080B	S	0	B	60.77	3.45	2.86	1.47	3.06	<0.01	0.81	0.16	0.13	0.04	0.004	6.8	1.21	7.37
080Q	S	0	VO	86.35	1.27	1.57	0.68	1.42	<0.01	0.26	0.05	0.07	0.02	0.003	3	0.63	2.08
081	S	0.1	SH	57.57	11.04	4.62	3.27	7.69	<0.01	2.76	0.49	0.16	0.14	0.008	12	2.99	0.53
082	S	0.5	SH	62.53	15.15	3.99	1.18	5.1	0.02	1.74	0.75	0.23	0.05	0.013	9	1.13	0.02
084	Au9	2.5	SH	56.25	18.49	6.48	3.02	2.77	1.08	4.33	0.69	0.15	0.05	0.011	6.5	0.98	0.27
088	Au9	0	VO	1.02	0.52	0.8	2.89	51.13	<0.01	0.07	0.03	<0.01	0.03	<0.002	43.2	12.35	0.03
090	Au9	0	SH	13.74	9.32	7	11.25	22.79	0.01	2.4	0.36	0.05	0.08	0.007	32.8	8.82	2.34
091	Au9	0.5	QD	49.88	15	3.35	4.04	8.53	0.03	3	0.58	0.12	0.06	0.005	15.2	3.38	0.12
150	S	-	Dio	62.31	16.1	4.96	2.28	5.54	2.25	2.09	0.59	0.11	0.05	0.004	3.5	0.39	<0.01
151	S	-	QD	64.99	16.53	3.62	1.47	4	2.59	3.09	0.61	0.13	0.04	0.004	2.7	0.25	0.01

Table 1.1 continued

Sample	Prox. Orebody	Dist. Orebody	Lith	Ba	Sc	Cs	Ga	Hf	Nb	Rb	Sn	Sr	Ta	Th	U	V	W	Zr
ZZG18-		m		PPM	PPM	PPM	PPM	PPM	PPM	PPM	PPM	PPM	PPM	PPM	PPM	PPM	PPM	PPM
016	S	-	Slate	480	17	15.6	21.8	3.8	12.5	133.7	4	374.4	0.9	13.5	2.6	107	2	135.6
023	S	-	Slate	304	13	4.3	15.2	4.4	12.2	90.7	2	230.2	0.9	12.6	2.8	83	1.9	160.3
030	S	-	SH	378	16	9.6	20.5	3.7	12.6	116.7	8	1004	0.8	13.6	3.3	107	2.8	125.9
041	Au1	0	VO	264	1	0.4	0.7	0.1	0.4	3.7	1	143.9	<0.1	0.5	1.2	<8	2381	4.6
048	Au9	0	B	168	7	7.9	8.8	1.8	5.2	97.1	1	194.1	0.3	6.5	2.6	51	12.4	58.7
049	Au9	0	VO	90	8	7.1	9.8	1.6	5.1	95.6	2	807.1	0.3	5.9	3.7	62	35.7	60.1
050	Au9	0.1	SH	125	14	14.2	16.7	3	9.2	129.1	5	459.8	0.7	10.4	5.9	98	32.5	107.4
051	Au9	5	SH	163	14	17.1	17.9	3.2	11.1	116	2	185.4	0.7	12.6	2.2	96	6.8	109.9
055	Au1	0	VO	10	<1	0.3	<0.5	<0.1	0.3	2.6	<1	17.1	<0.1	<0.2	0.3	<8	1.8	1.1
056	Au1	0.1	QD	126	8	21.3	18.1	4	8.4	190.1	1	156.5	0.5	10.9	4.5	45	37.3	154.7
057	Au1	0	VO	39	<1	0.3	1.5	<0.1	2.5	3.4	<1	16.5	<0.1	0.2	0.1	<8	0.8	1.6
059	Au1	0	QD	64	3	6.4	8.5	2.1	4.5	95.2	<1	162.7	0.4	6.2	3.7	22	24	77.4
060a	Au1	0	VO	98	<1	0.2	<0.5	<0.1	1.3	0.8	<1	71.3	<0.1	0.3	0.3	<8	422	1.8
065	Au1	0.1	QD	74	4	5.1	7.5	2.2	3.7	48.1	<1	486	0.2	5.5	9	21	20.7	77.6
068	Au1	0.15	SH	193	17	13.2	20.1	3.2	12	120.8	4	326.3	0.8	13.5	3.1	108	16	127.9
070	Au1	0	OB	115	11	8.7	13.9	2.2	8	127	2	294.7	0.5	9.5	5.8	75	22.1	76.2
072	Au1	20	SH	332	14	7.4	18.6	2.7	10.5	82.8	4	650.6	0.9	12.1	2.7	90	26.8	101.3
074	M9	0	VBS	142	4	8.2	6.2	1	3.8	70.9	<1	194.6	0.3	2.8	1.2	27	23.4	38
075	M9	0.1	SH	355	17	19.7	22.4	3.7	13	201.8	5	83.2	0.8	15.1	3	120	57.2	139
076	M9	5	SH	335	16	31.3	21.5	3.3	13.3	288.2	3	230.9	0.9	14.9	4.1	124	50.6	121.6
078	M9	5	QD	186	7	26.2	20.3	4	7.6	226.9	6	72.3	0.6	8.2	5.9	48	33.2	145.6
080B	S	0	B	122	4	3.7	2.8	1.6	2.4	33.5	2	620.7	0.2	4.8	0.9	26	18.1	54.1
080Q	S	0	VO	43	2	1.2	0.5	0.4	0.9	11.7	<1	312.5	<0.1	2.1	0.3	<8	8.2	14.4
081	S	0.1	SH	163	10	24.3	11.5	3.7	8	143	11	757.4	0.6	8.6	2.5	63	31.1	136.3
082	S	0.5	SH	252	14	9.6	17.1	7.3	12.9	63.7	11	90.8	0.9	14.8	4.7	88	84.8	284.4
084	Au9	2.5	SH	454	18	15.1	22.3	3.8	12.2	146.3	4	253.8	0.8	14	3.1	123	2.2	135.5
088	Au9	0	VO	46	1	0.6	<0.5	0.2	0.4	5.3	<1	2146	<0.1	0.7	0.3	<8	5.1	6.9
090	Au9	0	SH	170	9	9	11.8	2	6.7	89.5	7	868.2	0.5	8.2	3.9	61	30.5	72.2
091	Au9	0.5	QD	215	10	13.7	17.6	3.8	8.6	146.9	6	588.9	0.5	10.3	3.4	53	13.9	145.1
150	S	-	Dio	564	12	10.1	18	4.1	7.6	116.1	4	319	0.5	10.1	3.8	58	1.3	153.3
151	S	-	QD	641	5	9.4	20.1	4.7	9.1	127.8	2	301	0.6	14.4	3.2	34	1.2	176.2

Table 1.1 continued

Sample	Prox. Orebody	Dist. to Orebody	Y	La	Ce	Pr	Nd	Sm	Eu	Gd	Tb	Dy	Ho	Er	Tm	Yb	Lu
ZZG18-		m	PPM	PPM	PPM	PPM	PPM	PPM	PPM	PPM	PPM	PPM	PPM	PPM	PPM	PPM	PPM
016	S	-	23.4	37.3	76.8	8.51	32	5.35	1.11	4.72	0.71	4.25	0.91	2.59	0.36	2.35	0.36
023	S	-	27.9	35.6	70.2	7.43	27.7	5.86	1.2	5.69	0.85	4.94	1	2.89	0.39	2.65	0.37
030	S	-	23.4	38.2	76.8	8.21	30.1	5.4	0.99	4.5	0.68	4.07	0.86	2.53	0.36	2.4	0.36
041	Au1	0	3.2	22.6	8.4	1.04	4.5	0.9	0.47	1.02	0.13	0.87	0.1	0.27	0.03	0.16	0.01
048	Au9	0	11	19.3	37.3	4.1	15.7	2.58	0.49	2.21	0.31	1.82	0.42	1.18	0.16	1.21	0.18
049	Au9	0	17.1	22.2	44.4	4.85	19.1	3.51	0.77	3.3	0.48	2.84	0.59	1.67	0.21	1.35	0.19
050	Au9	0.1	21.4	31.3	62.1	6.82	26.2	5.13	1.03	4.63	0.69	3.94	0.77	2.2	0.3	2.25	0.31
051	Au9	5	23.9	37.9	74.4	8.17	29.6	5.09	1.01	4.78	0.73	4.25	0.84	2.3	0.32	2.05	0.31
055	Au1	0	0.6	0.6	0.7	0.06	0.3	0.08	0.02	0.12	<0.01	0.07	<0.02	<0.03	<0.01	<0.05	<0.01
056	Au1	0.1	11	33	63.1	7.09	27.6	5.29	1.2	4.27	0.53	2.53	0.43	0.95	0.12	1.02	0.12
057	Au1	0	0.2	2.8	0.8	0.05	<0.3	<0.05	<0.02	0.08	<0.01	0.08	<0.02	0.03	<0.01	<0.05	<0.01
059	Au1	0	4.9	18.9	36.2	4.04	15.6	2.69	0.5	1.8	0.22	0.99	0.16	0.49	0.05	0.44	0.06
060a	Au1	0	1.2	9.3	1.5	0.14	0.7	0.11	0.1	0.22	0.04	0.21	0.04	0.09	<0.01	<0.05	<0.01
065	Au1	0.1	6.8	15.6	28.6	3.13	11.1	2.06	0.44	1.89	0.25	1.26	0.22	0.56	0.07	0.5	0.07
068	Au1	0.15	25.5	41	78.2	8.57	32.6	6.63	1.39	6.24	0.9	4.9	0.96	2.66	0.38	2.55	0.37
070	Au1	0	16.2	27.9	54.1	6.1	23.6	4.29	0.76	3.54	0.51	2.83	0.6	1.82	0.23	1.62	0.23
072	Au1	20	26.4	35.5	71.8	7.58	27.8	5.82	1.13	5.54	0.82	4.63	0.93	2.71	0.36	2.49	0.38
074	M9	0	4.7	8.6	12.5	1.33	5	0.79	0.16	0.76	0.12	0.84	0.15	0.58	0.07	0.51	0.07
075	M9	0.1	25.7	41	80.6	8.67	32.1	6.35	1.29	5.6	0.88	4.87	0.96	2.84	0.41	2.69	0.39
076	M9	5	24.3	42.8	83.5	9.43	33.7	6.01	1.02	4.71	0.75	4.35	0.88	2.64	0.39	2.59	0.39
078	M9	5	10.2	17.9	32.7	3.63	13.8	2.38	0.47	2.12	0.36	2.01	0.37	1.01	0.12	0.88	0.11
080B	S	0	8.7	20.9	27	2.99	11.5	2.23	0.43	1.95	0.28	1.67	0.33	0.85	0.11	0.69	0.12
080Q	S	0	2.6	8.4	12.5	1.37	5.5	1	0.19	0.77	0.1	0.56	0.09	0.28	0.03	0.23	0.03
081	S	0.1	19.5	27.4	51.2	5.72	21.9	4.38	0.93	4.4	0.65	3.45	0.7	2.11	0.29	1.96	0.28
082	S	0.5	23.4	35.3	67.7	7.58	29.2	5.87	1.18	5.16	0.79	4.56	0.92	2.6	0.4	2.71	0.39
084	Au9	2.5	22.9	41.2	80.4	8.62	31.6	5.27	0.88	4.19	0.69	3.93	0.91	2.59	0.39	2.59	0.4
088	Au9	0	3	2.6	4.6	0.51	1.7	0.33	0.08	0.39	0.06	0.32	0.07	0.22	0.02	0.21	0.02
090	Au9	0	15	23.2	45.5	4.99	19	3.39	0.69	3.15	0.5	2.67	0.5	1.4	0.21	1.31	0.18
091	Au9	0.5	11.6	30	58.3	6.56	24.7	4.55	0.98	3.8	0.49	2.43	0.38	1.13	0.16	1.04	0.15
150	S	-	14.2	29.3	54.4	6.26	23.5	4.42	1.14	4.01	0.61	3.15	0.61	1.68	0.21	1.41	0.2
151	S	-	7.7	30.8	64.9	7.04	25.8	4.52	1.03	3.49	0.46	1.86	0.32	0.59	0.08	0.53	0.07

Table 1.1 continued

Sample	Prox. Orebody	Dist. to Orebody	Lith	Cu	Pb	Zn	Ag	Ni	Co	Mn	As	Au	Sb	Tl	Hg	Te
ZZG18-		m		PPM	PPM	PPM	PPB	PPM	PPM	PPM	PPM	PPB	PPM	PPM	PPB	PPM
016	S	-	Slate	15.37	4.99	82.3	17	35.8	17.3	391	33.3	22.4	7.66	0.53	13	0.05
023	S	-	Slate	28.32	31.12	81.6	33	30.6	14.5	1337	7.4	1	4.14	0.07	31	0.03
030	S	-	SH	23.64	5.19	52.4	24	20.9	9	158	8.8	7.7	0.93	0.18	<5	0.06
041	Au1	0	VO	9.94	<0.01	327.9	14521	2.9	0.9	287	0.2	56521.2	>2000	8.03	410	<0.02
048	Au9	0	B	10.79	2.9	101.2	321	16.2	7.5	582	>10000	10404.5	1896.97	1.35	309	0.02
049	Au9	0	VO	22.29	29.68	68.4	672	17.2	7.6	611	>10000	16984.6	88.82	0.26	125	0.06
050	Au9	0.1	SH	67.15	23.95	110.8	377	30.5	15.6	669	4075.4	1386.5	75.82	0.19	84	0.04
051	Au9	5	SH	33.51	19.36	84.2	35	29.7	16.9	435	45.1	7.1	393.66	0.26	11	0.04
055	Au1	0	VO	4.77	0.72	23.8	2009	0.7	0.2	112	26.2	25617.1	>2000	0.02	34	<0.02
056	Au1	0.1	QD	15.25	17.94	61.7	409	10.6	10.4	504	9623.2	1600.5	41.75	0.14	68	<0.02
057	Au1	0	VO	16.03	0.57	52.9	3239	0.6	0.2	134	78	23408.1	>2000	0.38	107	<0.02
059	Au1	0	QD	6.07	1.79	24.3	806	5.2	5.6	272	>10000	12067.6	71.58	0.71	108	0.15
060a	Au1	0	VO	10.27	0.19	193.7	1378	0.4	0.1	197	2	184.2	>2000	0.28	277	<0.02
065	Au1	0.1	QD	5.4	8.22	11	178	6.4	4.8	615	3092.9	1249.9	193.54	0.61	52	0.05
068	Au1	0.15	SH	56.15	23.57	90.1	50	28.9	17.9	642	83.8	35.3	72.26	0.36	45	0.03
070	Au1	0	OB	21.49	8.12	127.7	814	27.1	10.9	522	>10000	18632.1	123.09	0.45	98	0.1
072	Au1	20	SH	28.82	24.69	68.3	76	23.1	11.2	847	68	166.4	16.89	0.37	7	0.88
074	M9	0	VBS	27.99	17.8	636.2	144	8.1	3.9	157	2734.4	4788	>2000	0.14	1346	<0.02
075	M9	0.1	SH	69.86	16.42	38.1	84	25.8	16.3	681	458.1	31.8	1887.07	0.3	25	0.05
076	M9	5	SH	31.05	4.86	64	1217	34	17.7	494	>10000	6784.9	127.26	0.3	69	0.05
078	M9	5	QD	22.95	2.06	284	1030	8.4	9.3	180	>10000	7136.5	83.5	0.74	412	0.07
080B	S	0	B	44.22	3.52	368.3	4095	8.5	2.9	360	340	8790.6	>2000	5.29	1058	0.03
080Q	S	0	VO	51.85	58.74	546.3	914	6.6	2	198	2724.3	3411.3	>2000	0.93	1171	<0.02
081	S	0.1	SH	23.33	4.19	59.1	134	17.3	9.2	1077	4511.6	4613.8	121.34	0.19	44	0.1
082	S	0.5	SH	17.68	7.7	55.1	44	18	10.9	360	222.4	70.6	80.97	0.28	139	0.18
084	Au9	2.5	SH	55.91	13.95	89.8	54	34.7	15.4	322	228.2	10.3	45.11	0.27	7	0.04
088	Au9	0	VO	2.34	1.76	7.7	180	0.8	0.9	191	86	1431.1	63.54	<0.02	11	0.16
090	Au9	0	SH	35.07	15.52	15.3	1623	21.6	17.5	542	9455.1	6431.1	63.46	0.15	89	0.22
091	Au9	0.5	QD	39.72	6.67	15.2	203	5.5	8.3	448	319.5	49.5	25.35	0.08	12	0.1
150	S	-	Dio	16.2	5.1	40.9	25	6.3	11.4	322	47.9	14.6	40.95	0.04	7	0.03
151	S	-	QD	36.9	7.43	47.1	34	8.8	8.6	262	84.2	26.2	76.71	0.12	14	<0.02

1.10.1 Elemental Correlations

Basic factor analysis of bulk rock geochemistry results was performed and are presented in Table 1.2. The table contains Pearson's correlation coefficients based on the covariance between elemental values analyzed. The Pearson's correlation coefficient is a measure of the linear correlation between two populations of data. High coefficient values approaching 1.000 indicate a strong 1:1 linear correlation. Low coefficient values approaching -1.000 indicate a strong -1:1 linear correlation. Analyses of high-grade vein samples and disseminated sulfide ore exceeded the upper quantifiable limits for antimony (2000 ppm) and arsenic (10,000), so the statistical accuracy of correlation involving these two elements can not be verified. The correlation coefficients relating these two elements to others in the dataset are qualitative.

In analyzed samples from Zaozigou, gold has high correlation with antimony (0.471), arsenic (0.165), tungsten (0.758), silver (0.874), zinc (0.216), and mercury (0.169). Gold has negative correlation with molybdenum (-0.149), copper (-0.350), lead (-0.252), cobalt (-0.208), and tellurium (-0.153).

Antimony has strong positive correlation with mercury (0.626), tungsten (0.339), silver (0.470), and zinc (0.576). Antimony has negative correlation with arsenic (-0.151), molybdenum (-0.320), nickel (-0.423), and cobalt (-0.585).

Arsenic has positive correlation with gold (0.165), and manganese (0.124). Arsenic has negative correlation with tungsten (-0.121) and copper (-0.169). Other correlation coefficients do not indicate a strong correlation positive or negative with arsenic, varying from -0.094 to 0.080.

Additional strong positive correlation coefficients within the selected elements of the dataset are Zn-Hg (0.950), W-Ag (0.925), Zn-Ag (0.320), Cu-Pb (0.519), Cu-Co (0.463), and

Cu-Te (0.422). Notable strong negative correlation coefficients within the selected elements of the dataset are Hg-Co (-0.446), W-Co (0.294), Ag-Co (-0.403), and Zn-Co (-0.353).

Table 1.2. Pearson correlation coefficients of bulk rock geochemistry values of common Au-associated elements. Antimony displays a negative correlation with Arsenic, likely due to differing methods of precipitation of stibnite and arsenopyrite. Mercury is strongest correlated with Zinc followed by Antimony. Gold is strongest correlated with Ag, which is a logical conclusion considering free gold in samples analyzed by FE-SEM and EDS indicate that gold flecks have a roughly 80:20 gold to silver ratio. Note: true statistical correlation for Sb and As is not possible based on the data in this report. This is due to several Sb and As analyses exceeding the upper reporting limit of the geochemical laboratory. Upper limit for Sb was 2000 ppm. Upper limit for As was 10000 ppm.

	Sb	As	Hg	Au	W	Ag	Mo	Cu	Pb	Zn	Ni	Co	Mn	Te
Sb	1.000													
As	-0.151	1.000												
Hg	0.626	0.067	1.000											
Au	0.471	0.165	0.169	1.000										
W	0.339	-0.121	0.130	0.758	1.000									
Ag	0.470	-0.067	0.250	0.874	0.925	1.000								
Mo	-0.320	0.059	-0.149	-0.206	-0.149	-0.193	1.000							
Cu	-0.023	-0.169	0.117	-0.350	-0.201	-0.194	0.041	1.000						
Pb	-0.010	0.024	0.297	-0.252	-0.192	-0.232	0.019	0.519	1.000					
Zn	0.576	0.009	0.950	0.216	0.266	0.320	-0.090	0.146	0.340	1.000				
Ni	-0.423	0.048	-0.314	-0.333	-0.229	-0.314	0.480	0.410	0.282	-0.201	1.000			
Co	-0.585	0.080	-0.446	-0.468	-0.294	-0.403	0.433	0.463	0.222	-0.353	0.892	1.000		
Mn	-0.326	0.124	-0.293	-0.208	-0.117	-0.199	0.143	0.225	0.331	-0.280	0.482	0.462	1.000	
Te	-0.067	-0.094	-0.032	-0.153	-0.047	-0.094	0.541	0.422	0.199	0.029	0.312	0.264	0.150	1.000

1.11 Ore Mineralization

Distinct ore assemblages occur in Zaozigou in five distinct styles of hypogene mineralization. Mineralization is predominantly observed in veins, veinlets, and lodes of varying dimensions, and within vein-related alteration haloes. These mineralization assemblages and styles are described below in Table 1.3 and shown in Figure 1.41. The occurrences of the ore mineralization styles within orebodies are shown in Figure 1.4 and Figure 1.5.

Table 1.3. Summary chart of main ore style characteristics at Zaozigou Au-Sb deposit. Reported Au grades are based on independent multiple element analysis analyzed by LA-ICP-MS, n=31. Range of Au grade is based on bulk rock multi-element analysis and drillhole assay data. Max Au grade is based on the samples selected for bulk rock geochemistry. Due to the relatively high volume of hydrothermally altered rock at Zaozigou, range of Au concentration is more accurate for alteration-related ore than vein-related ore. This is partially due to the 1 meter sample intervals used in drill core assays. Reported max Au grade based on maximum Au concentration observed in the present study.

Style	Example Orebody	Ore mineral assemblage	Gangue mineral assemblage	Au grade (ppm)
Vein	M4, M6, M7, M9	Stibnite, Au (<20% Ag), pyrite, sphalerite, galena	Quartz ± carbonate (calcite, ankerite, dolomite)	5-10 (max 56.5)
Vein	Au9	<1 vol% pyrite, hematite	Dolomite, ankerite, calcite	~1-2 (max 1.4)
Vein Breccia	Au1, Au9	Arsenopyrite, pyrite, stibnite,	Quartz, illite, muscovite, chlorite, kaolinite,	>10 (max 18.6)
Alteration halo in slate hornfels	All hosted in slate hornfels	Arsenopyrite, (arsenian) pyrite, sphalerite	Calcite, quartz, illite (NH ₄), kaolinite, chlorite	1-7 (max 10.4)
Alteration halo in quartz dacite	All hosted in quartz dacite	Arsenopyrite, (arsenian) pyrite, sphalerite	Quartz, illite, muscovite, chlorite	2-10 (max 17.0)

Carbonate vein orebodies are likely late features resulting from dissolution of carbonate from host metasedimentary rocks and remobilization of Fe and Mg from clays, chlorites, and micas. Carbonate veins regularly crosscut Au and M style orebodies and veins (Figure 1.31). Carbonate in the form of calcite, dolomite, and ankerite is precipitated as late fracture infill within and at the margins of quartz-stibnite veins.

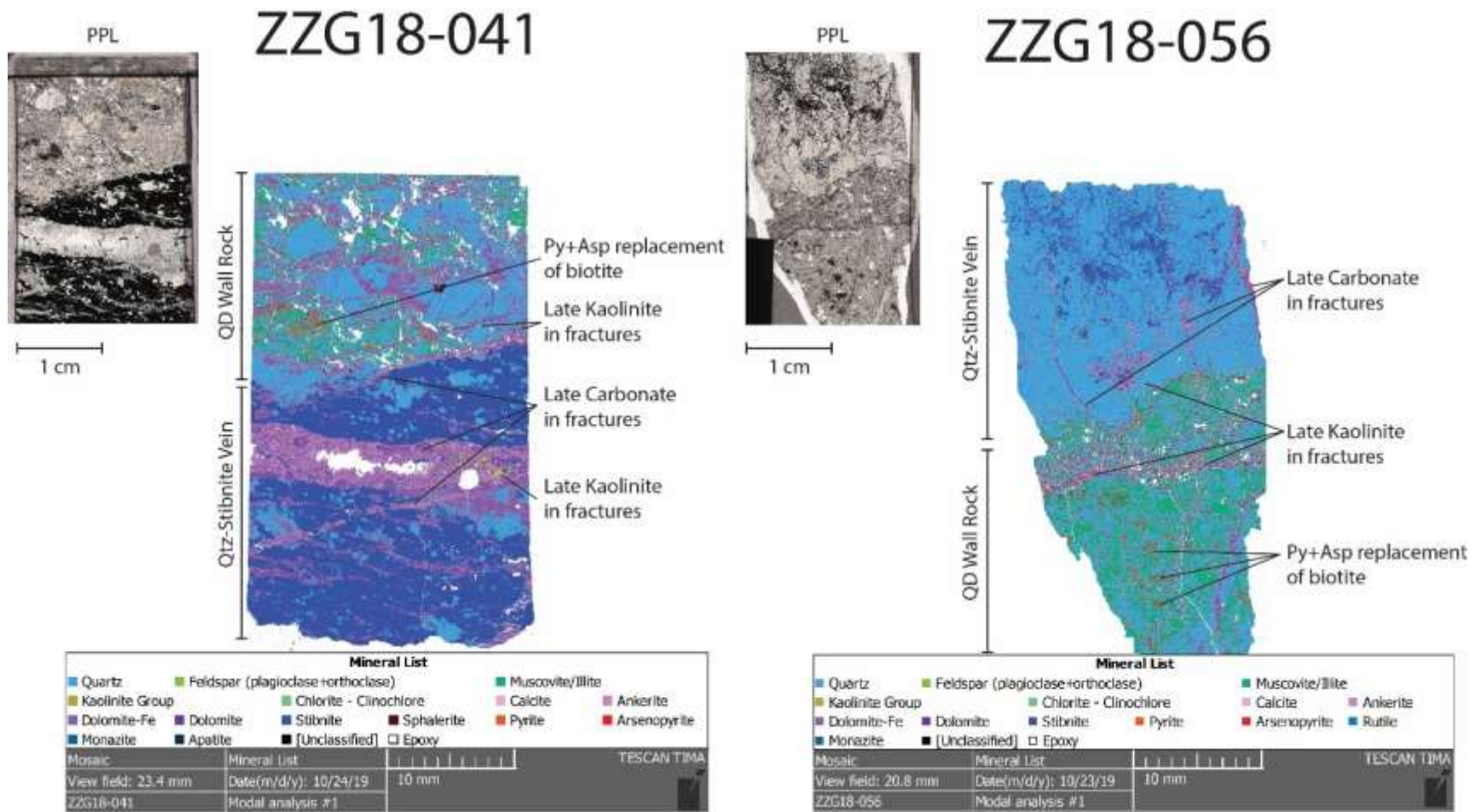


Figure 1.31. QEMSCAN mineral maps of two vein and disseminated mineralization hosting samples which were also studied petrographically. Pink and purple coloration corresponds to carbonate minerals, which are observed to occur as late overprints and fracture filling features.

1.11.1 Quartz-stibnite vein mineralization

Vein mineralization assemblages are most commonly found as quartz+stibnite discrete planar veins. Quartz-stibnite veins hosted in shallowly dipping faults are found as extensional veins where typically the veins are rimmed with quartz and have stibnite cores (Figure 1.32).

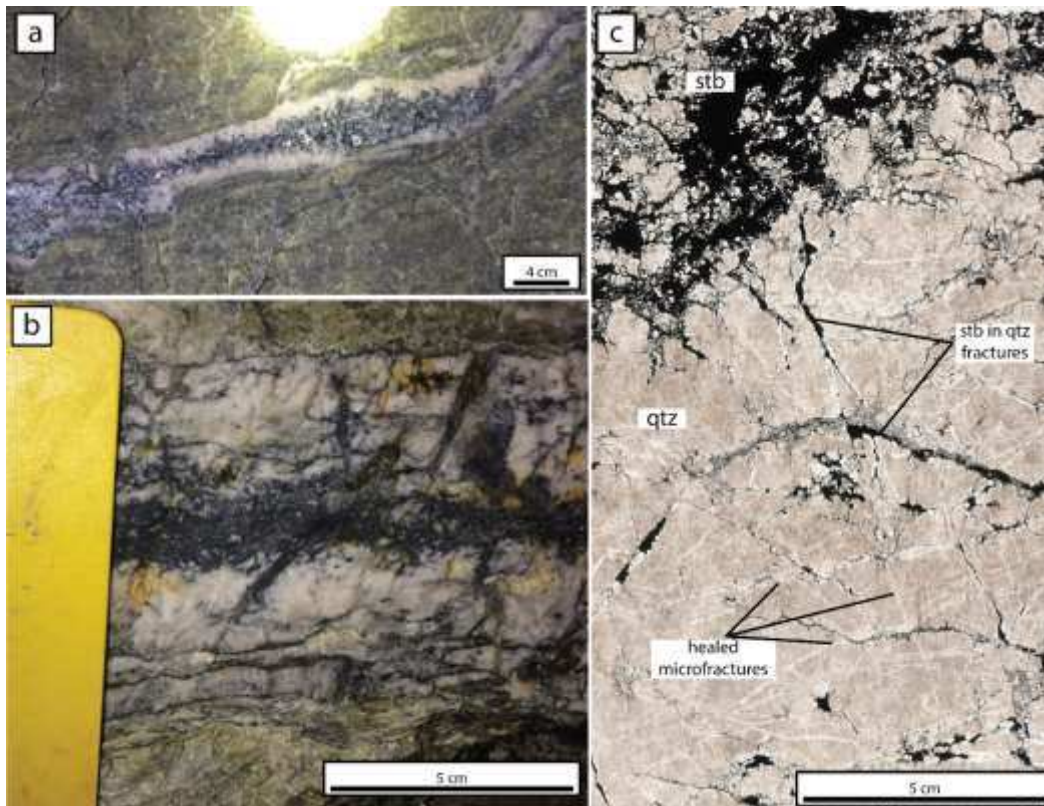


Figure 1.32. Typical quartz-stibnite veinlets within altered quartz dacite. Photo a.) taken on the 3050 level proximal to the M7 orebody. The quartz rims in this veinlet show typical comb quartz texture, indicating the opening direction of the vein and growth direction of the quartz crystals. Stibnite within these veinlets are typically amorphous. Where vugs are found, needle-like stibnite crystals can be observed growing into the void space. Photo b.) taken on the 2660 level as a constituent of orebody M10. This vein is oriented as 335/43. C.) is a thin section scanned in plane light of sample ZZG18-057, taken from the Au1 orebody.

Quartz-stibnite veins hosted in steeply dipping faults are frequently found to be highly fractured. They are rarely observed as vertically continuous, having been intensely fractured and dislocated. Deformation of the quartz is brittle, whereas ductile flow is prevalent among the

stibnite. These steeply dipping “Au” orebodies host stibnite mainly within quartz fractures. The difference in mineral deformation between quartz and stibnite is important to note. Studies of stibnite deformation are sparse; however, most researchers compare the material properties of stibnite with pyrrhotite (McQueen et al., 1980; Kuşçu and Erler, 1999; Bellot et al., 2004). As such, under stress regimes where quartz behaves in a brittle fashion, it is possible to interpret stibnite as a highly mobile mineral. Under tectonic stresses, stibnite is able to flow and infiltrate spaces opened by mechanical deformation. As such, it is difficult to conclude conclusively that stibnite precipitation was coeval with the precipitation of quartz. From context, and comparison with quartz-stibnite veins found within shallowly dipping orebodies, it can feasibly be concluded that quartz and stibnite precipitation occurred nearly simultaneously within individual tectonic pulses.

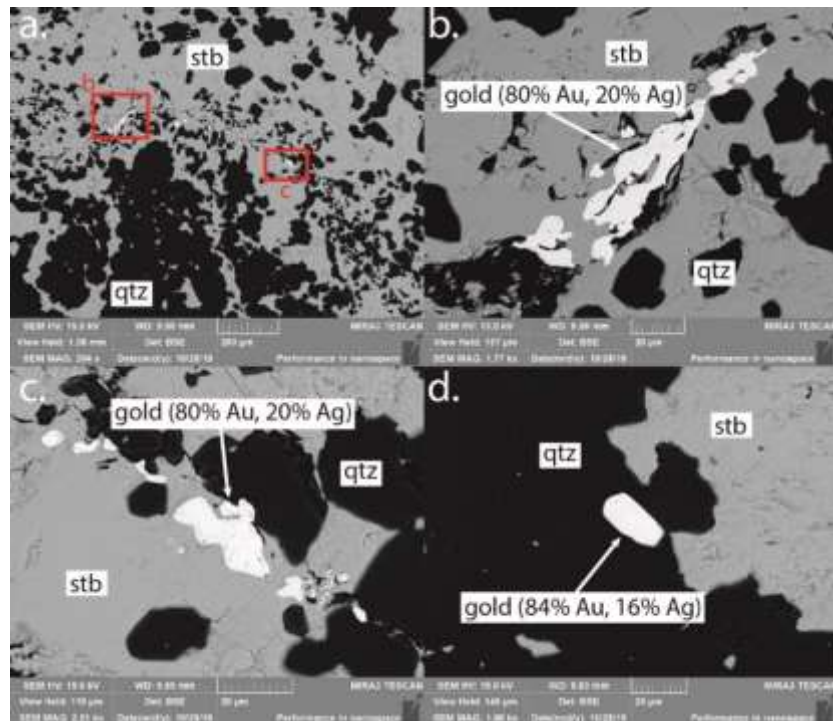


Figure 1.33. FE-SEM scans of sample ZZG18-056, which displays visible gold flecks up to 40 μm . Gold flecks were analyzed using by energy-dispersive X-ray spectrometry (EDS) to be an alloy of 80% Au, 20% Ag. EDS is not reliably quantitative to evaluate the true gold fineness. Silver in gold grains analyzed by EDS should be considered qualitative.

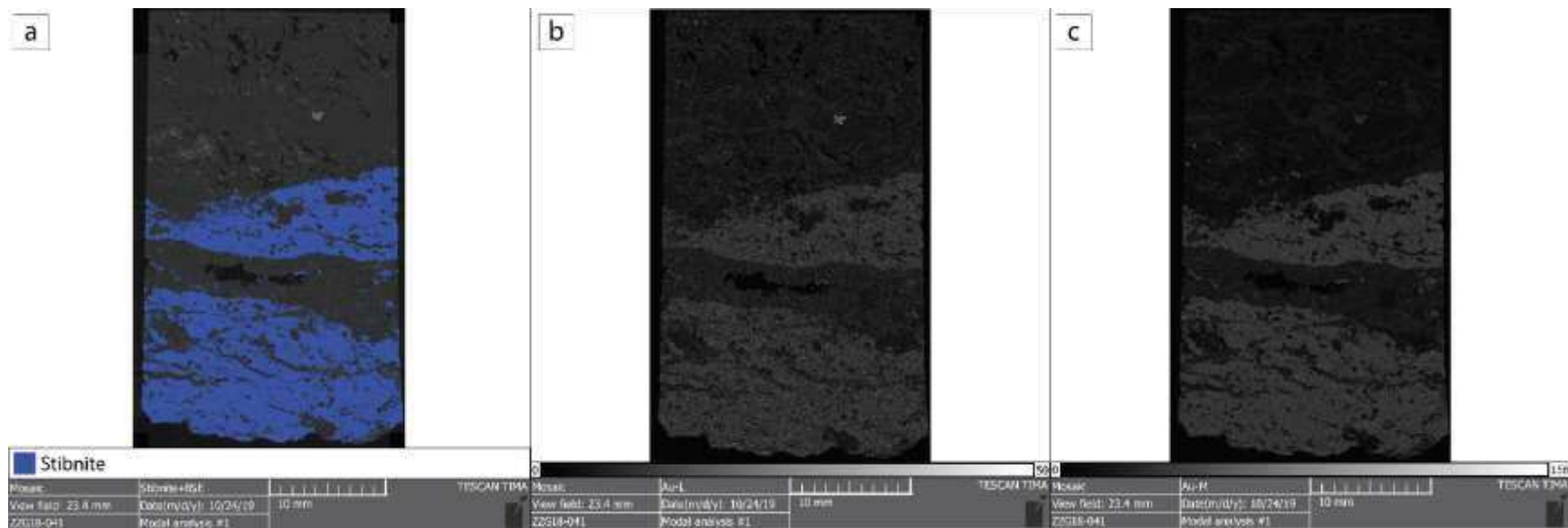


Figure 1.34 SEM/EDS scans of sample ZZG18—041. Sample is a high Au grade quartz-stibnite fault-hosted vein. A.) false color stibnite modal analysis shows the distribution of stibnite within the sample, superimposed on a backscatter electron background. b.) Electron dispersive X-ray scan of sample ZZG18-041 Au-L energy band. Relative high Au-L energy corresponds with stibnite. C.) Electron dispersive X-ray scan of sample ZZG18-041 Au-M energy band. Relative high Au-M energy response corresponds with stibnite.

Free gold is found within quartz vein fractures, sometimes spatially associated with, and crosscutting stibnite mineralization (Figure 1.33). Blebby flecks of free gold contain 80% Au and 20% Ag, as analyzed by Energy-Dispersive X-ray Spectroscopy (EDS). This method is not reliably quantitative.

Energy dispersive X-ray spectroscopy scans indicate low gold concentration within stibnite found in “M” style quartz-stibnite veins and lodes (Figure 1.34). EDS analysis for gold is generally not a reliably quantifiable method for analyzing elemental concentration in minerals. In EDS analysis, each element has up to a theoretical five characteristic X-rays which are produced when a specimen is excited by an incident electron beam. These are the K, L, M, N, and O energies which are related to the valence shells of each element. Elements may be inaccurately identified due to the similarity of characteristic X-rays across energy bands. For example Sodium characteristic K energy X-ray is 1.041 keV, which is very close to the L energy X-Ray of Zn, which is 1.012 keV. Thus a specimen being analyzed by EDS for Zn may be influenced by the presence of Na in the specimen.

Gold has two characteristic X-ray energy signatures when analyzed by EDS: These are the L energy and M energy characteristic X-rays. The L energy of gold is 9.712 keV. The M energy of gold is 2.120 keV. Gold’s L energy X-ray is similar to the K energy of Germanium (9.874 keV). Gold’s M energy is similar to the K energy of Sulfur (2.307 keV). Figure 1.34 shows QEMSCAN, SEM, and EDS scans of sample ZZG18-041. This sample hosts massive stibnite within a coarse-grained quartz vein from the Au1 orebody. Figure 1.34b,c show that the Au-L and Au-M signatures are coincident with the stibnite crystals in the vein. This would suggest that the stibnite crystal hosts some refractory enrichment of gold within the crystal lattice. However, it is probable that the sulfur and germanium content of the stibnite is

influencing the gold signal. Germanium is known to occur in sulfide minerals in lower temperature (<300°C) ore deposits, particularly lead or zinc sulfide minerals in VMS, MVT, Carbonate Replacement, and SEDEX deposits (Shanks et al., 2017, citations within). Germanium is not included in the bulk rock geochemical analysis of the present study, therefore it is impossible to estimate how much of the Au-M energy X-ray was contributed by the Ge content of stibnite in sample ZZG18-041. However, this sample was analyzed to contain 56,521 ppb Au (Table 1.1); the highest value among all analyzed samples. Visible gold has not been observed in hand sample, SEM bright phase scans, petrographic analysis, or hand panning of a 263-gram crushed sample. Because sample ZZG18-057, which was also collected from Au1 vein ore, and was analyzed to contain 23,408 ppb Au, has been shown to contain visible gold flakes in petrographic analysis and hand-panning of a crushed sample (Figure), it is highly probable that free gold exists in sample ZZG18-041 and due to the “nugget effect” free gold was simply not found within the polished face of the prepared thin section, and the researcher’s gold panning skill was insufficient to effectively and consistently separate gold flakes from crushed sulfide material. However, it is nonetheless interpreted that the combination of Au-L and Au-M X-ray energy signature coincident with stibnite in a known high-grade gold sample absent of observed free gold is indicative that gold exists within stibnite at Zaozigou. Follow-up analysis of stibnite by electron probe microanalysis is suggested to further investigate the gold content of stibnite in both “Au” and “M” style orebodies. With gold values of quartz-stibnite vein ore frequently exceeding 10000 ppb Au it is perplexing that the gold endowment represented by the quartz-stibnite is often reported as insignificant. During the site investigation, it was observed that large stockpiles of cobble to boulder sized quartz-stibnite ore fragments were stacked on the mine property and not routed to the mill. The coarse ore stockpiles were periodically loaded into high

capacity shipping trucks and hauled off property. I believe that the Zaozigou mill is not configured to handle ore of high stibnite content, and that the coarse ore is sold to another processing facility. As a result, the quartz-stibnite ore endowment may be under-reported.

1.11.2 Dolomite-ankerite-calcite low sulfide lode-style vein mineralization

The dolomite-ankerite-calcite low sulfide vein mineralization is observed only at Au9. The mineralization is cryptic, as neither sulfide minerals represent <1 vol% of the observed rock volume and are primarily pyrite. Free gold is not observed within the dolomite-ankerite-calcite orebodies. The widest observed vein has been measured at 5 m thick. It occurs as a subvertical lens of dolomite-ankerite-calcite containing abundant angular clasts of altered slate hornfels wall rock. The dolomite is coarse. It displays clear euhedral surfaces (Figure 1.35). The lode vein has hairline fractures which have been infilled with hematite. It is possible that the infilling hematite represents post-ore remobilization of Au, which precipitates within the fractures. Sample ZZG18-088 was analyzed to contain 1.4 ppm Au, the lowest grade of all orebodies directly sampled.



Figure 1.35. The Au9 dolomite lode vein. Euhedral dolomite faces are observed, and hematite fills in fractures.

1.11.3 Cataclastic vein brecciation mineralization

Found in all orebodies, but most voluminous in Au1 and Au9, the cataclastic vein brecciation mineralization is an important mineralization style. Analyses of this mineralization style have returned values of up to 18.6 ppm (sample ZZG18-070, Figure 1.36). Samples of this style of mineralization range in appearance, depending on the intensity of brecciation. ZZG18-120 M9 (Figure 1.41 e.) represents a sample taken from within a vein orebody. Samples taken from the cataclastic vein brecciation mineralization “Au” orebody samples have the highest analyzed gold values. ZZG18-070 (Figure 1.36), taken from the Au1 orebody, represents a fault boundary sample. It has an ashy appearance due to the volume of fine-grained wall rock fragments. Clasts in ZZG18-070 are elongate and imbricated, indicating

The cataclastic vein brecciation mineralization consists of wall rock fragments cemented in a quartz-sulfide matrix. Wall rock fragments are variably altered, depending on the clast size. The hydrothermal alteration of these wall rock fragments occurred during the brecciation as hydrothermal fluids flowed through the fault conduits. Finer lithic clasts are more strongly altered and can be replaced entirely by pyrite and/or arsenopyrite if sufficiently fine. Brecciation and re-brecciation are evidenced by clast composition. The clasts indicate a polymict breccia. In addition to altered slate hornfels and altered quartz dacite fragments have being observed, quartz vein fragments, and lithic clast-hosting quartz vein fragments have also been found, cemented in a quartz-sulfide matrix.

The dominant sulfide minerals in this style of mineralization are stibnite, arsenopyrite, and pyrite. Stibnite occurs exclusively within quartz veins, quartz vein fragments, and quartz-sulfide matrix. Pyrite and arsenopyrite occur as disseminated mineralization within wall rock clasts or as wholesale replacement of finely ground wall rock.

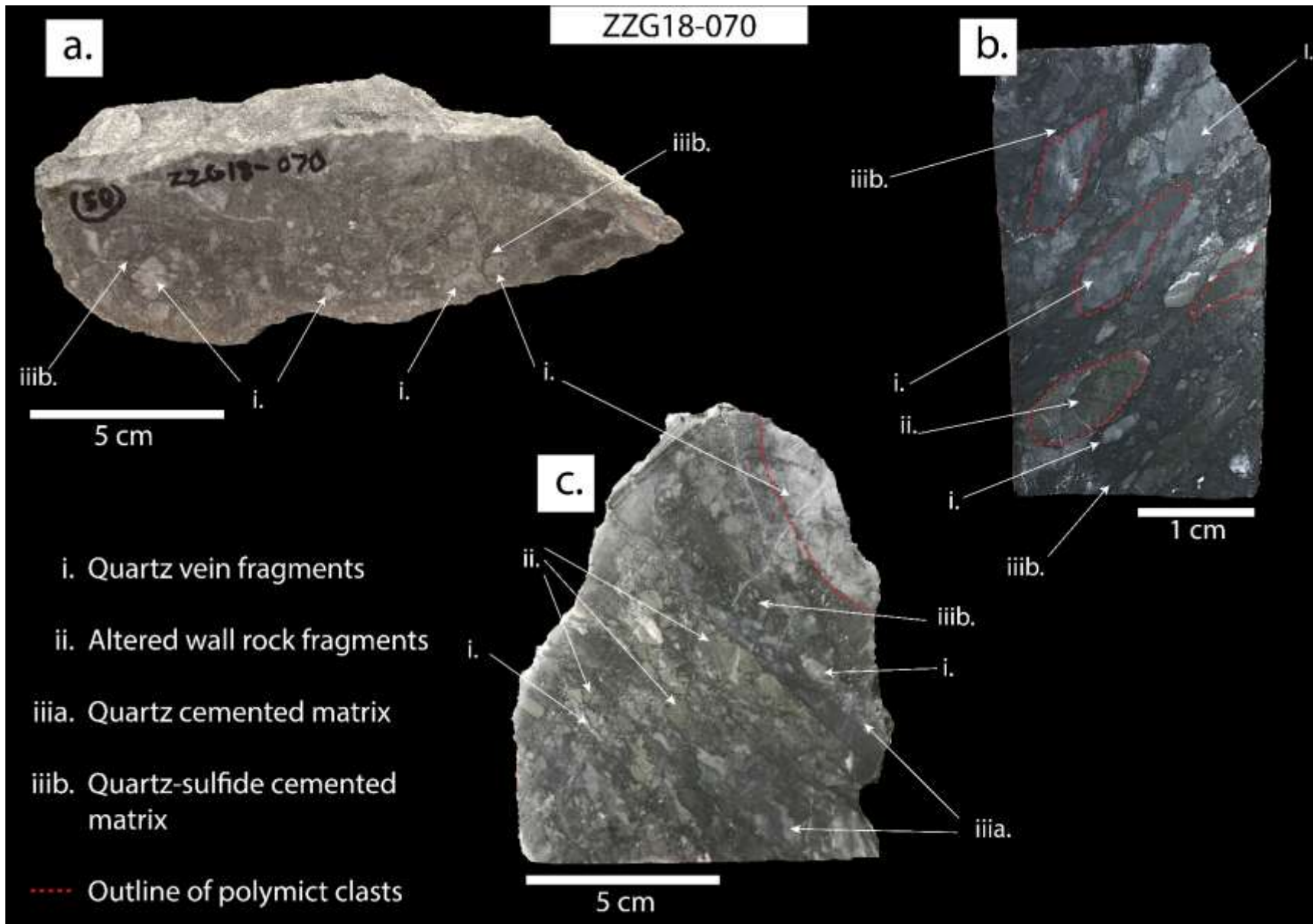
Brecciation and cataclasis occurs at fault interfaces where frictional forces grind fragments of wall rock through fault movement events. Brecciation is a well-known method for generating open space for mineralization through the localization of low-pressure inter-fragmental pockets becoming favorable locations for fluid flow. Additionally, the frictional grinding motion of the fault interface results in fine grained crush rock which have high surface area to volume ratios. The high surface area to volume ratio allows for more effective hydrothermal alteration of the fragments within the fault.

1.11.4 Slate hornfels-hosted disseminated sulfide wall rock alteration mineralization

Hydrothermal alteration within slate hornfels is associated with precipitation of disseminated sulfides which are mostly localized within the Fe-rich sedimentary layers of the slate hornfels. Fine Arsenopyrite and pyrite precipitate preferentially within cleavage planes (Figure 1.37). These preferential horizons within the sedimentary layers have elevated illite content, suggesting these were Fe-rich horizons which are preferentially more reactive to Sulfur rich fluids. The Fe-rich horizons serve to localize wall rock sulfidation reactions. Quartz±calcite infill and overprint the fluid conduits used by hydrothermal fluids to permeate the slate hornfels. Tabular or rhombic arsenopyrite crystals often are aligned such that the long axis trends parallel to the bedding plane of the sediments.

The gold grade in altered slate hornfels is highest proximal to fault-hosted mineralization. Typical grades for gold in proximal altered slate hornfels range from ~5 ppm Au to a maximum analyzed at 6.7 ppm, which was sampled 5 m from the M9 orebody. Elevated gold grades (184 ppb), have been measured in altered slate hornfels up to 20m laterally from Au1 (sample ZZG18-072). Background Au levels in the Gulangdi slate (ZZG18-023) are 1 ppb and slate hornfels 7.7 ppb (ZZG18-030) (Figure 1.38).

Figure 1.36. (Next Page) Sample photos of ZZG18-070. This is a sample of the cataclastic ore breccia which can be found within fault zones in subvertical fault-hosted orebodies at Zaozigou. Clockwise from top left a.) is the rough cut hand sample which was collected from the Au1 orebody at the 2860m level. Due to the fine grained cement and altered host rock altered slate hornfels clasts, sample ZZG18-070 has a dark, ashy appearance. b.) and c.) are moderately polished billet and slab and the imbrication of sub-rounded mono- and polymictic clasts are observable, along with shear fabric indicators. The dark interclastic cement is dominantly composed of fine-grained quartz with interstitial sulfides (pyrite+arsenopyrite) and dusty fragments of altered wall rock. Three types of clasts can be observed in hand specimen: i. (pure) quartz clasts, which are remnants of quartz veins which previously infilled the Au1 fault prior to at least one generation of frictional reactivation, ii. Altered wall rock fragments of slate hornfels composition. As individual clasts cemented in the quartz-dominant matrix these are sub-rounded and host minute disseminated pyrite and arsenopyrite within proto-bedding planes, and iii. Polymictic clasts which are composed of quartz and altered slate hornfels wall rock fragments. These altered slate hornfels fragments are angular, and typically dispersed within larger quartz clasts such that the larger clast represents quartz vein material which, possibly during the original fault formation, incorporated angular wall rock clasts within the crush zone which was the conduit for fluids and the permeability pathway for these fluids to precipitate lode-style quartz veins. Sample ZZG18-070 is stibnite-poor, sulfides observed in thin section are predominantly fine grained pyrite with minor arsenopyrite.



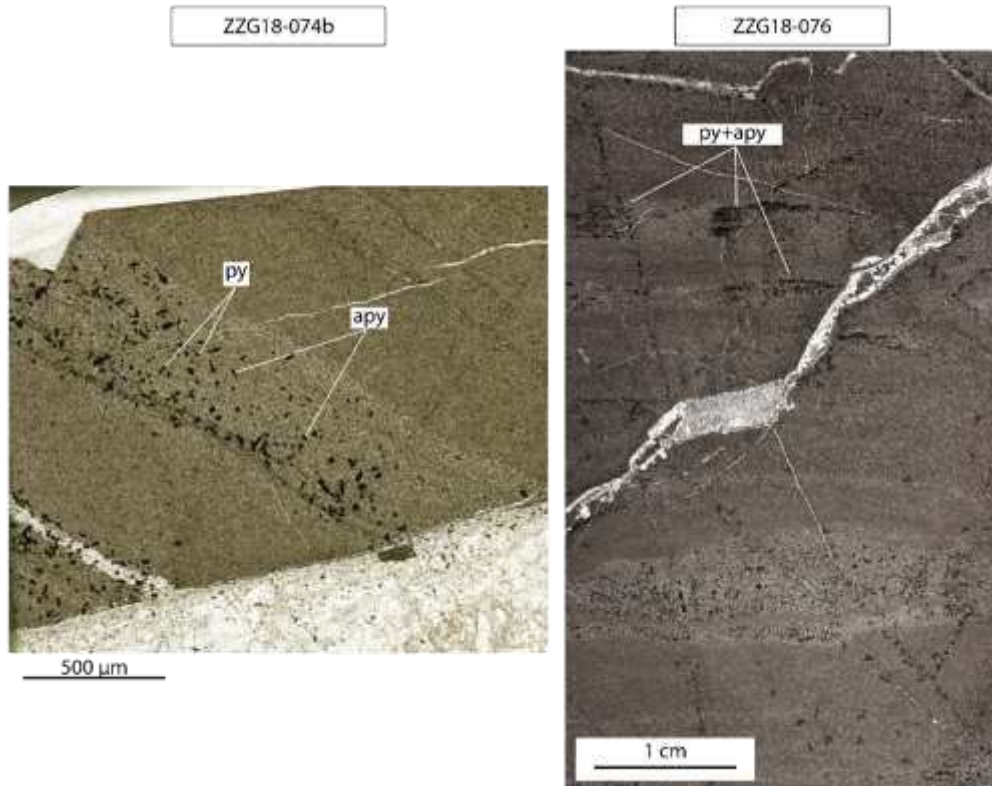


Figure 1.37. Thin section photomicrographs of hydrothermally altered slate hornfels. Pyrite and arsenopyrite (opaque minerals) are concentrated within specific sedimentary horizons. Py = pyrite, apy = arsenopyrite.

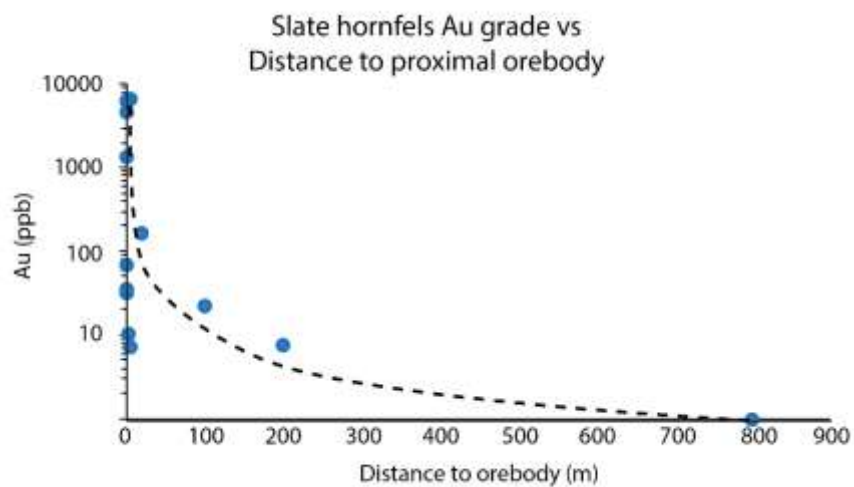


Figure 1.38. Grade-distance diagram showing decay of Au grade in slate hornfels with increased distance from orebody. Note Y axis logarithmic scale. Dotted line is an approximation of Au grade decay distal to the orebody. This is an illustrative approximation not based on any statistical method.

The highest Au grade analyzed from slate hornfels disseminated sulfide ore was 6.8 ppm. High Arsenic values (>4000 ppm) corresponded with greater Au analyses (>1 ppm). Mineralized slate hornfels are Sb-poor. One sample (ZZG18-075) had anomalously high Sb (1887 ppm) without any observable stibnite in hand sample.

1.11.5 Quartz dacite porphyry-hosted disseminated sulfide wall rock alteration mineralization

Disseminated arsenopyrite and pyrite are found replacing biotite and chlorite phenocrysts within altered porphyritic quartz dacite porphyry dikes. Arsenopyrite and pyrite precipitated through wall rock sulfidation reactions of Fe-rich mineral phases within bleached alteration haloes proximal to fault and vein-controlled orebodies.

Sericitic alteration plays a critical role in the generation of the quartz-dacite porphyry hosted disseminated sulfide mineralization at Zaozigou. The dominant sericite species at Zaozigou are (NH₄) illite and muscovite. The reaction to replacement biotite by illite or muscovite releases Fe, which can subsequently be utilized by S±As bearing fluids, leading to the precipitation of iron sulfides, which have been shown to host refractory Au at Zaozigou (Tang et al., 2019). This mineralization is typified by arsenopyrite and pyrite replacement along cleavage planes of biotite phenocrysts. Minor quantities of disseminated iron sulfides precipitate within the groundmass.

Arsenopyrite crystals replacing biotite in the wallrock host micro-inclusions of stibnite and sphalerite (Figure 1.39c,d). This is strong evidence that the same fluids responsible for precipitating wallrock disseminated sulfide also carried antimony. This suggests that vein hosted

stibnite and wallrock disseminated pyrite and arsenopyrite precipitated during the same fluid cycling events.

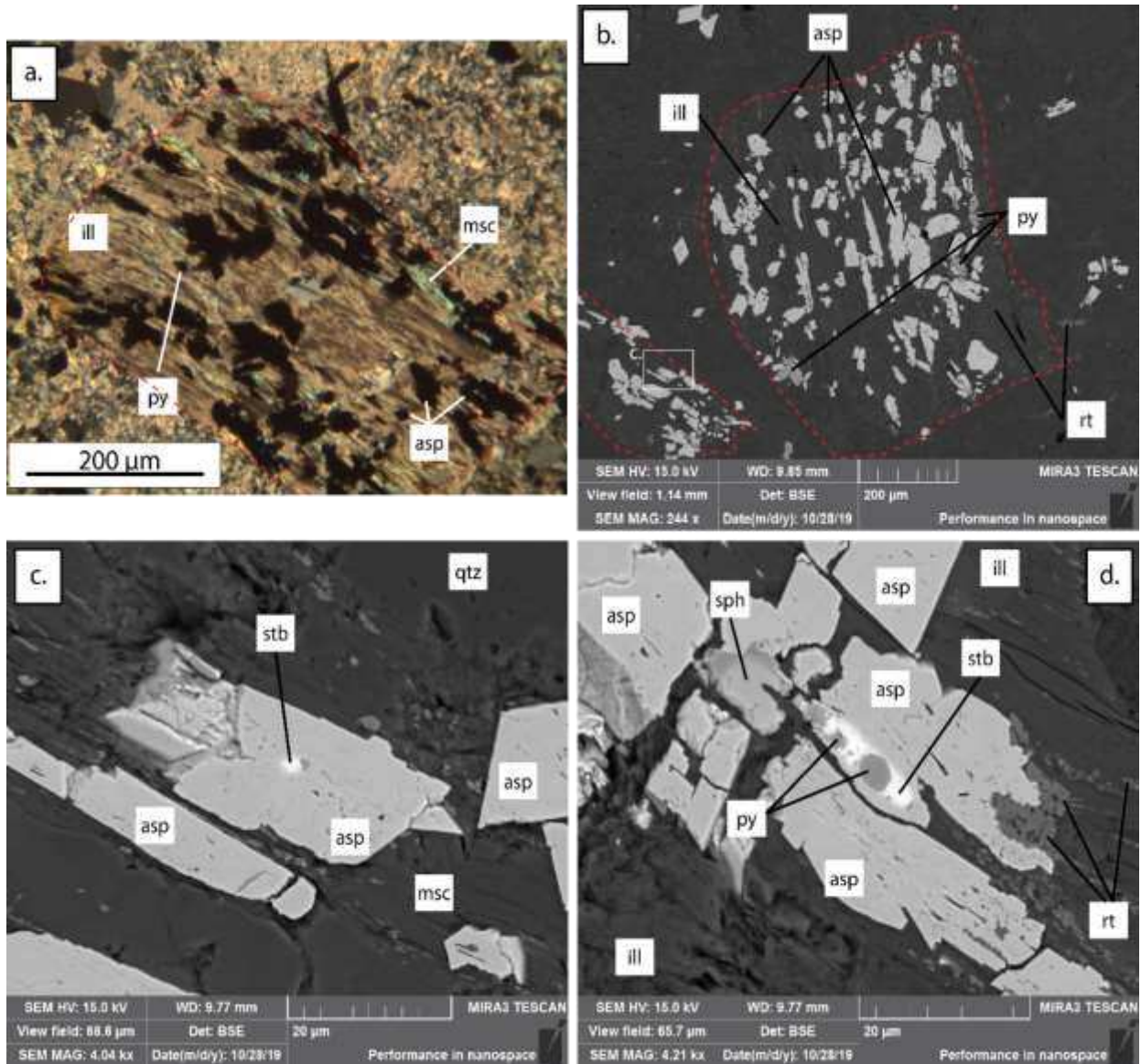


Figure 1.39. Photomicrograph and electron microscope scans of sample ZZG18-056. a.) transmitted polarized light and b.)-d.) scanning electron microscope images of arsenopyrite replacing biotite in situ. Arsenopyrite crystals host inclusions of stibnite, pyrite, and sphalerite. The long axis of arsenopyrite crystals align parallel with biotite cleavage. Ill = illite, msc = muscovite, py = pyrite, asp = arsenopyrite, rt = rutile. Red dashed lines represent the outline of relict biotite phenocrysts.

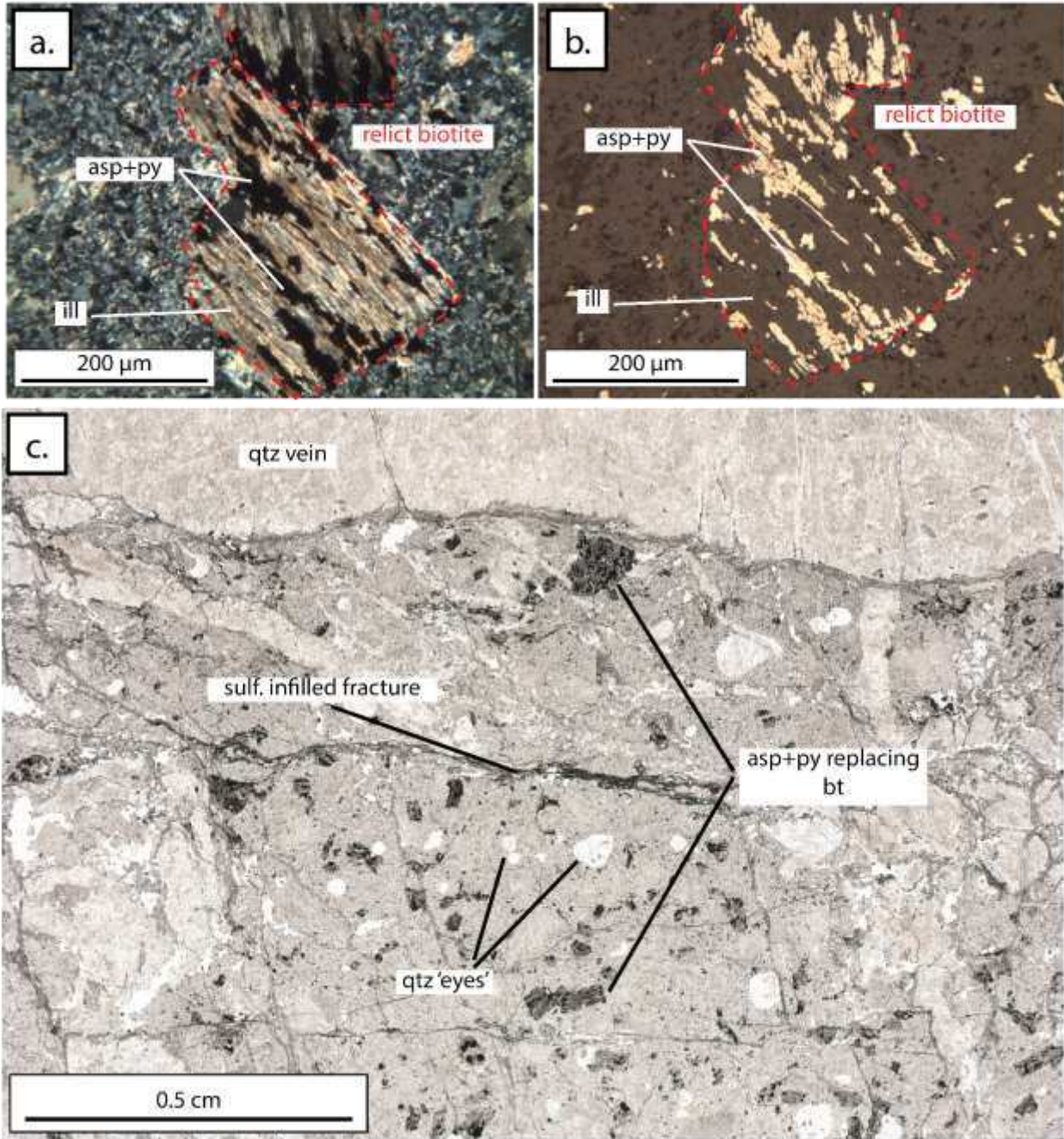
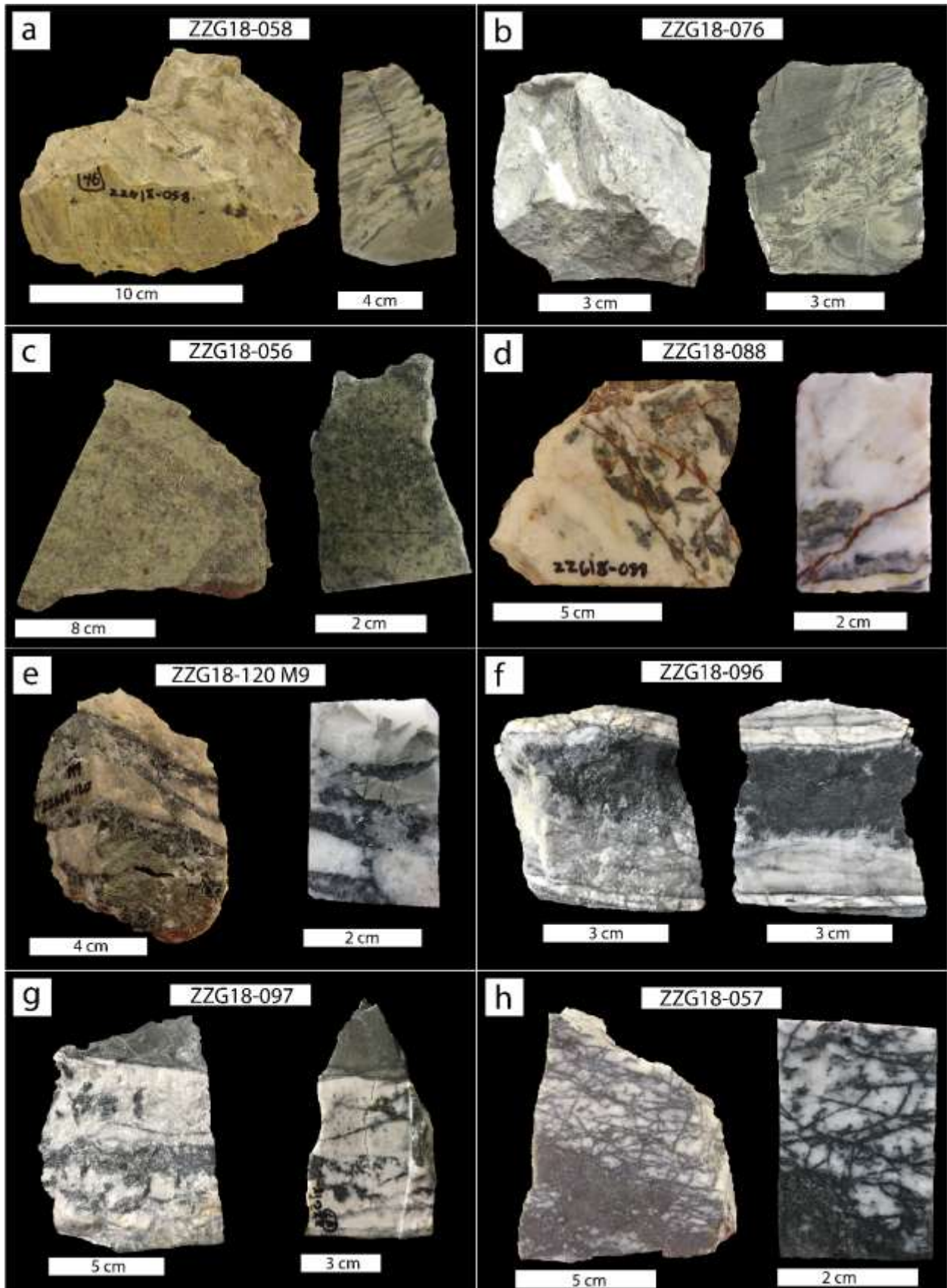


Figure 1.40. Photomicrographs of iron sulfides replacing biotite along cleavage planes during synchronous sericitic alteration of biotite. A.) cross-polarized transmitted light, b.) reflected light, c.) plane polarized transmitted light thin section scan. Ill = illite, qtz = quartz, asp = arsenopyrite, py = pyrite, bt = biotite

Figure 1.41. (Next Page) Representative ore sample photographs from Zaozigou. a.) Altered slate hornfels. b.) Altered slate hornfels. c.) Altered quartz dacite porphyry. d.) Dolomite-calcite low sulfide vein style ore. e.) Quartz-stibnite vein breccia ore. f.) Quartz-stibnite vein ore. g.) Quartz-stibnite vein ore. h.) Quartz-stibnite vein ore.



The highest analyzed Au value for mineralized quartz dacite porphyry was 12067.6 ppb. However this value is likely skewed by the sample containing a crosscutting quartz vein (Table 1.1). Vein free samples were analyzed with Au values ranging from 49.5 to 7136.5 ppb Au. Arsenic values of the highest gold intervals exceeded the upper detection limit (10,000 ppm). All quartz dacite porphyry samples analyzed are Sb-poor (< 200 ppm) when compared with other ore samples.

1.12 Discussion

1.12.1 Role of contact metamorphism

The intrusion of the ca. 248.9 ± 1.4 Ma quartz dacite porphyry dikes led to the contact metamorphism of the Gulangdi slate and the development of the slate hornfels at Zaozigou. Trace element geochemistry and bulk rock major oxide geochemistry (Figure 1.7) paired with the field observations of a gradient between pure hornfels and slate confirms that the Gulangdi slate is the probable protolith for the slate hornfels which hosts ore at Zaozigou.

Pre-mineralization structures, notably the plunging folds and upturned beds, are indicative of early ductile deformation in the local area. Ore hosting features are controlled by brittle deformation in the form of faults, fault breccias, and cataclastic zones. The pre-ore dike intrusions do not display ductile deformation. Ore hosting faults are found preferentially at the margins of the intrusions, where they contact the slate hornfels. Multiple scenarios could result in the transition from a ductile to brittle deformation at Zaozigou. A change in tectonic regime could cause this transition. Regional studies of the West Qinling do not address a significant change in the magnitude of stress or strain rate which could result in this transition. A far more likely cause for a shift from ductile to brittle deformation is a change in local rheology. Contact metamorphism of the Gulangdi slate resulted in change of rock strength parameters for the

metasedimentary unit. This change of rheology led to the unit hardening of the slate hornfels. As a result, the slate hornfels expressed strain as brittle deformation, leading to the widescale faulting which became the main ore hosts at the deposit.

1.12.2 Peak metamorphism of host rocks at Zaozigou

Slates which were not strongly contact metamorphosed and quartz dacite porphyry dikes exhibit metamorphic reactions consistent with mid- to late- Triassic regional metamorphism along the Mianlue suture zone during the West Qinling orogenesis. Garnet rims being replaced by chlorite in quartz dacite porphyry dike samples indicate that the dikes at Zaozigou experienced a prograde and retrograde metamorphic path after their emplacement ca. 248.9 ± 1.4 Ma. The prograde path may have reached upper greenschist to lower amphibolite facies metamorphism. Garnet represents peak metamorphism of the quartz dacite porphyry. Garnet may have been metastable and influenced by the composition of metasedimentary rocks in contact with the quartz dacite porphyry dikes. Garnet within the quartz dacite porphyry dikes could also be a result of the dikes incorporating sedimentary material during their emplacement. Chlorite identified by SWIR in slate samples may be indicative of regional prehnite-pumpellyite to greenschist metamorphism. No aluminosilicates have been observed in the metasediments at Zaozigou, suggesting the slates experienced only low-grade metamorphism.

The diorite porphyry dikes (actually andesite composition) which post-date the emplacement of the quartz dacite porphyry dikes may indicate a local temperature increase during subduction-related crustal thickening. The timing of emplacement of the diorite porphyry dikes is ca. 237.5 ± 1.4 Ma. This could mark an approximate timing of peak metamorphism of the local Zaozigou host rocks. The regional tectonic evolution during the emplacement of the diorite porphyry dikes was post closure of the Shangdan ocean, during collision and accretion

related to Mianlue ocean subduction. During this time the fore-arc prism of accretionary pelitic sediments of late Permian to Triassic age were being subducted along with Mianlue Oceanic crust. The metamorphic devolatilization of these Permian to Triassic age metasediments during Triassic subduction may represent a viable fluid source which led to the emplacement of ore at the Zaozigou Au-Sb deposit.

1.12.2 Structural evolution of Zaozigou in the context of the West Qinling Orogen

Linking the development of structural features at Zaozigou with regional scale tectonic events is essential to understanding establishing a rigorous geological framework for the deposit. Additionally, understanding the geological framework of Zaozigou can help to better understand the genesis of the Xiahe-Hezuo polymetallic zone.

The key assumption made here in the interpretation of the structural evolution of Zaozigou is that most of the folding of the sedimentary rocks occurred prior to the intrusion of Triassic dikes. This is a logical assumption to make based on two key observations: 1.) the Triassic dikes crosscut folded strata, and 2.) the Triassic dikes themselves are not folded. Folding most likely occurred after the local sedimentary strata were already lithified. This is evidenced by a lack of syn-diagenetic soft-sediment deformation structures such as slump folds. The sediments were most likely deposited during the Permian, as they were already lithified and folded by the time the first dikes intruded as early as 248.9 ± 1.4 Ma. The local Gulangdi sediments at Zaozigou were most likely deposited during continental accretion post-closure of the Shangdan Ocean and the folding observed pre-Triassic intrusion evolved during this NE-SW accretion. The pre-intrusion folds axes strike 144° to 160° and dip 58° to 81° to the SW, parallel to mineral foliation preserved in unaltered slates 800m east of the mining area (strike and dip of $147^\circ/68^\circ$ SE). NE-SW trending strike slip faults which would eventually be used as weakness

planes for later intrusion of Triassic dikes and reactivation as high angle reverse faults (i.e. the faults which host the Au1 and Au9 orebodies) likely also developed at this time.

The subduction of the Mianlue oceanic crust beneath the South Qinling Block is widely marked by late Permian to early Triassic magmatism (Dong et al., 2011). The quartz dacite and diorite dikes were likely emplaced during this period of subduction and accretion. The emplacement of these dikes led to contact metamorphism of the local sedimentary rocks, resulting in the slate hornfels, and increasing the local rock strength due to the rheological increase.

The intrusion of Triassic dikes marks the transition from ductile-plastic deformation to brittle deformation. By this time the NE-SW closure of the Mianlue Ocean was completing and suturing of the South China Block to the South Qinling Block resulting in oblique convergence. The Au1 and Au9 orebodies have orientations striking 235° to 248° and dipping subvertically to 77° to the NW. The M7 and M6 orebodies strike subparallel (220° to 032°) and dip 30° and 19° to the SE and NW, respectively. These orientations are perpendicular to the NE-SW direction of tectonic convergence and accretion. The Au1 and Au9 orebodies are hosted in high angle reverse faults and the M6 and M7 orebodies are manifest as extensional quartz-stibnite veins, indicating that the local compressional axis at Zaozigou was oriented NW-SE. This is probably a result of strain localization in response to the initiation of continent-continent convergence and accretion. The tectonic blocks resisted the continued NE-SW convergence, leading to crustal thickening and localized NW-SE compression to accommodate the strain. Crustal thickening and accretion may have driven increased fluid pressures, and the transition from ductile to brittle rheologies allowed the pressurized hydrothermal fluids to reach supralithostatic forces, reactivating the NE-SW trending strike-slip faults as fault veins (Au1 and Au9) and the M6 and M7 orebodies as

nearly flat lying extensional veins. Fluid pressure cycling may have continued throughout the period of accretion of the South China Block and South Qinling Block with “Au” and “M” hosting structures acting as fault valves (Figure 1.42). The multistage reactivation of the “Au” and “M” style orebodies is evidenced by hydrothermally cemented mineralized wall rock fragments and quartz-stibnite vein fragments in “Au” style orebodies (Figure 1.36, page 81), and by the multiple generations of extensional veins (Figure 1.17, page 39), and observed healed microfractures in quartz crystals of the “M” style orebodies (Figure 1.21, page 50).

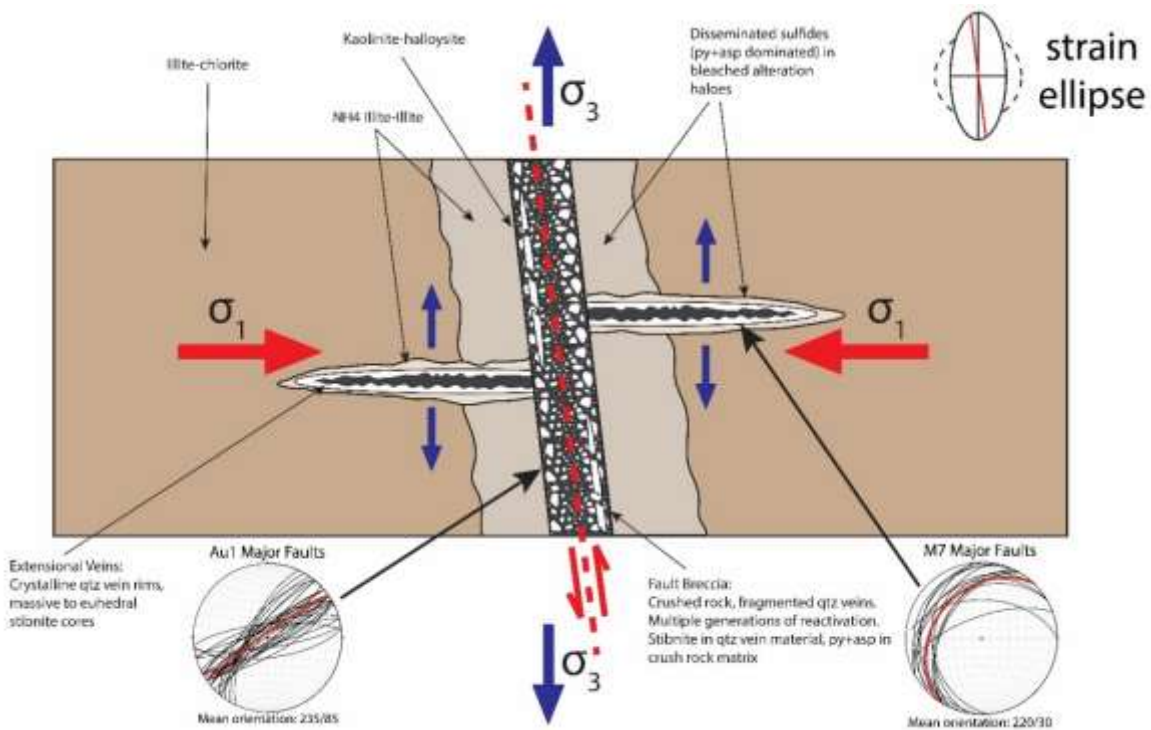


Figure 1.42. Schematic diagram of the relationship between “Au” and “M” style orebodies at Zaozigou in a fault-valve model.

Late-stage crosscutting faults such as the oxide fault (Figure 1.19, page 44) likely occurred either in the Jurassic to Cretaceous deformation related to exhumation and subsidence or during the late Triassic as collision transitioned to post-collisional collapse.

1.12.3 Discussion of bimodal model for ore mineral precipitation

Gold mineralization is partitioned between quartz-stibnite veins mineralization and disseminated wall rock sulfides. Quartz-stibnite veins on average have been analyzed to contain higher gold grades than the disseminated mineralization. Both As and Sb have strong correlation with Au in bulk rock geochemical analysis (Table 1.2), however As and Sb have a negative correlation coefficient, which would suggest that As and Sb were precipitated independently during separate ore events. Most publications written on Zaozigou refer to disseminated arsenopyrite-pyrite ore as an earlier generation of ore which is later crosscut by the quartz-stibnite veins (Sui et al., 2018; Yu et al., 2019; Du et al., 2021). This is not necessarily the case, as disseminated arsenopyrite-pyrite ore precipitated via wall rock sulfidation, whereas stibnite is almost exclusively found within veins, indicating that very different ore precipitating mechanisms led to the formation of distinct disseminated arsenopyrite-pyrite ore and (fault) vein hosted stibnite ore.

The correlation coefficients presented in Table 1.2 suggest two dominant gold-related elemental and mineralogical assemblages. These are represented by the quartz-stibnite veins hosted within faults in “Au” and “M” style orebodies, and the related disseminated arsenic-pyrite wallrock sulfidation style ore which is hosted in alteration haloes surrounding “Au” and “M” style orebodies.

The first assemblage, represented by quartz-stibnite vein ore, has Au-Sb-Hg-W-Ag-Zn association, which is consistent with the observed mineral assemblage of quartz-stibnite-sphalerite-scheelite \pm native gold. Mercury is likely refractory in sphalerite and stibnite, as no mercury minerals have been observed. The negative association that the elements in the vein ore

assemblage show, primarily with relation to cobalt, nickel, molybdenum, and tellurium, may be representative of the ore fluid source and composition.

The second assemblage, represented by disseminated wall rock ore, has Au-As association, which is consistent with the observed mineral assemblage dominated by arsenopyrite and pyrite wall rock sulfidation. The negative correlation that arsenic shows with antimony and tungsten is probably reflective of the different methods of precipitating Fe-sulfides during wall rock sulfidation compared with pressure cycling controlling quartz-stibnite ore in “Au” and “M” style orebodies.

Stibnite inclusions within arsenopyrite crystals found replacing biotite in wall rock mineralization (Figure 1.39c,d, page 85) indicate that the same fluids responsible for precipitating stibnite in fault hosted veins also precipitated pyrite and arsenopyrite in the wall rock. Additionally, ore stage pyrite crystals have been shown by in situ LA-ICP-MS to contain Sb levels up to 4617 ppm (Du et al., 2021). Narrow quartz-stibnite veinlets with quartz-pyrite-arsenopyrite selvages and sericitic alteration haloes are frequently observed (Figure 1.11, page 27; Figure 1.25, page 55), further suggesting that the antimony-bearing hydrothermal fluids also carried arsenic which preferentially precipitated in the wallrock by sulfidation reactions with Fe-rich wall rock minerals. Stibnite, being absent of Fe in its chemical makeup, does not precipitate by sulfidation of Fe-rich minerals in the wall rock at Zaozigou.

The solubility and physicochemical controls of antimony speciation and stibnite precipitation are discussed at length in Appendix C. Krupp and other researchers (Krupp et al., 1988; Hagemann & Luders, 2003) working in similar Au-Sb systems have suggested that adiabatic decompression could lead to a decrease in temperature sufficient to trigger precipitation of stibnite (Hagemann & Luders, 2003; Voisey et al. 2019).

Traditionally, Au-As, Au-Sb, and Au-Sb-Hg mineral assemblages in gold deposits have been thought to occur in different, and discrete temperature conditions, such as described in temperature delineated hypozonal, mesozonal, and epizonal environments following hypothermal, mesothermal, and epithermal deposit types (Lindgren, 1933). Based on this understanding of ore minerals' affinities for varying temperature conditions, a logical conclusion upon observation of a deposit wherein disseminated arsenopyrite is found within wallrock which is cut by stibnite-bearing quartz veins could be that the precipitation of the disseminated arsenopyrite in the wallrock preceded quartz-stibnite veining at a time when the gold system was hotter. Thus as the system cooled to a temperature permitting stibnite precipitation, later pulses of mineralization would overprint the existing pervasive arsenopyrite mineralization. Where the predominant ore mineralization style varies as a function of depth and heat in the system, this phenomenon is referred to as a telescoped ore deposit, and has been recently invoked to describe the orogenic Fosterville gold deposit in Victoria, Australia (Voisey et al., 2019; 2020), which shares many characteristics with Zaozigou; primarily disseminated gold-bearing arsenopyrite and arsenian pyrite in metamorphosed sedimentary wall rocks being crosscut by quartz-(carbonate)-stibnite±gold veins. They propose that adiabatic decompression, whereby a localized decrease in pressure can trigger substantial reduction in temperature, related to the intense pressure fluctuation during fault-valve behavior could lead to a temperature decrease sufficient to trigger stibnite precipitation in extensional veins.

Adiabatic decompression may be a valid method for explaining stibnite precipitation which is concurrent with arsenopyrite precipitation. However, the noted differences in precipitation environment of wall rock-hosted disseminated arsenopyrite and arsenian pyrite and

quartz-stibnite veining at Zaozigou would suggest that adiabatic decompression alone is not solely responsible for the simultaneous ore mineralization.

Globally, Au-Sb deposits share many similarities (Appendix A). Au-Sb deposits are overwhelmingly found within greenschist to lower amphibolite facies carbonaceous or carbon-rich metamorphosed sedimentary rocks. Refractory gold is associated with Fe-sulfides and free gold is hosted in quartz±carbonate veins. Nearly every reported major Au-Sb deposit has stibnite-arsenopyrite-pyrite ore mineral association and sericite and/or carbonate alteration assemblages.

A plausible explanation for the coprecipitation of arsenopyrite and stibnite at Zaozigou is that hydrothermal fluid-rock interaction results in sericitic alteration haloes where biotite, chlorite, and Fe/Mg clay minerals liberate Fe which is then incorporated into the Fe-sulfides arsenopyrite and pyrite through wall rock sulfidation. This fluid-rock reaction removes sulfur from the ore-fluid. Krupp (1988), Hagemann et al., (2003), and Voisey et al., (2019;2020) show that a decrease in a_{H_2S} can trigger stibnite precipitation and precipitation of free gold (Appendix C). Petrographic observation in this study has shown that disseminated arsenopyrite and pyrite at Zaozigou precipitated with (NH_4) -illite replacement of biotite, chlorite, and feldspars in both quartz-dacite and slate hornfels host rocks. Scanning electron microscopy has also shown stibnite inclusions within this wall rock disseminated arsenopyrite replacing biotite (Figure 1.39), strongly suggesting that coeval precipitation of stibnite in veins and arsenopyrite in the wall rock occurred from the same ore fluid.

1.12.4 Ammonium illite as a product of hydrothermal alteration

The identification of hydrothermal ammonium (NH_4) illite in ore deposits is expanding with geologists increased usage of SWIR. Diagenetic ammonium varieties of silicate minerals commonly occur in sedimentary rocks high in organic matter, S-type granitoids, and accretionary

metamorphic rocks. The NH_4^+ ion similar charge and ionic radius to K^+ and Rb^+ , and is known to replace K and Na in feldspar, biotite, muscovite, illite, kaolinite. Application of spectral technologies has led to the identification of NH_4 illite as an important mineral for vectoring towards gold mineralization. NH_4 illite identification has notably been identified in spatially restricted alteration haloes such as at the Hauraki Au-Ag epithermal deposits (Simpson & Christie, 2018), Jerrit Canyon Carlin-type Au deposit (Mateer, 2010), the MacArthur River SEDEX deposit (Williams et al., 1987). Experimental synthesis of NH_4 illite has shown that at 300°C illite, illite-smectite, and kaolinite is preferentially replaced by NH_4 -illite when exposed to equimolar contents of K and NH_4 ions (Šucha et al., 1998). However, it is unlikely that kaolinite would withstand regional and contact metamorphism of the slate hornfels. Kaolinite is unstable under most conditions above 150°C (Zotov et al. 1998). Kaolinite is most likely a product of supergene weathering at Zaozigou. Slate hornfels at Zaozigou is therefore likely to have most remaining clay species and feldspar clasts replaced by NH_4 illite at the interpreted temperatures of an NH_4 -bearing hydrothermal fluid. NH_4 illite is a common diagenetic constituent of argillaceous shales, especially shales in which organic matter is a component. However, the presence of NH_4 illite as a hydrothermal mineral in the quartz dacite porphyry dikes at Zaozigou is likely not locally sourced from the Gulangdi slate, as unaltered samples (ZZG18-016, -023) did not contain NH_4 illite when analyzed by SWIR. Au-Sb deposits are commonly associated with $\text{H}_2\text{O}-\text{CO}_2-\text{CH}_4-\text{N}_2$ fluids (Appendix A; Hagemann & Luders, 2003; Bortnikov et al., 2010; Pochon et al., 2016). It is possible that Nitrogen in these fluids are responsible for the precipitation of NH_4 illite as an alteration product. This would suggest that the fluids which led to the precipitation of ore minerals at Zaozigou were also N_2 bearing fluids.

1.12.5 An orogenic gold deposit?

There is presently no consensus on which ore deposit model best describes Zaozigou. Two deposit styles are most prevalent when describing Zaozigou: orogenic gold deposit, or Reduced Intrusion Related Gold System (RIRGS).

Much of the lack of consensus on the deposit model at Zaozigou is likely due to the lack of an established geological and structural framework with which to evaluate the deposit. The geology of Zaozigou evolved in a compressional orogenic setting during a series of terranes accreting onto the North China Block including during the ca. Upper Devonian closure of the Shangdan Ocean and Permian-Triassic closure of the Mianlue Ocean.

The local tectonic regime within the Xiahe-Hezuo polymetallic zone is compressional to transpressional and includes the multi-stage reactivation of high-angle reverse faults and low angle thrust faults. Orebodies are explicitly structurally controlled by these faults and occur within veins, fault breccias, and associated hydrothermal alteration haloes. Veins record multitudes of protracted pressure cycling events. The relationship of “M” and “Au” orebodies and their characteristics best reflect a fault-valve system for the development of these orebodies (Figure 1.42). The orientations of ore hosting structures, and their crosscutting relationships show that orebody development occurred and continued during the structural-tectonic evolution of the local geology, recording a stepwise rotation of the principal stress axis. This relationship suggests that ore formation at Zaozigou continued over an extended timeframe and the ore history at Zaozigou may span several million years.

The interpretation of Zaozigou as a RIRGS relies on the fluid exsolution of a causative intrusion. The timeframe for formation of RIRGS is explicitly linked to the thermal history of the causative intrusion. Most intrusion-related deposits, such as porphyry and epithermal deposits,

form on the order of 10^4 years (McInnes et al., 2005). Attempts to constrain the age of Zaozigou based on bracketed intrusions have been shown to be misleading or inaccurate. Interpretation as a RIRGS also relies on a spatial zoned relationship with the intrusions at Zaozigou. Such a zonation pattern is not observed at Zaozigou in the present study, and the role of porphyritic dikes is interpreted to be ground preparation resulting in the transition to a brittle regime where faults are preferentially found at the hornfelsed contacts between intrusion and metasediments. There is a marked lack of many of the diagnostic features of RIRGS. These features which are not observed at Zaozigou include: enrichment in the metals Bi, Te, Sn, and Pb (Hart, 2007), a clearly genetic relationship of ores to a causative intrusion, metallic or ore style zonation centered on a causative intrusion, or an extensional tectonic setting sufficiently distanced from convergent plate boundaries (Lang & Baker, 2001).

Contextually, the structural and tectonic framework established here suggest that the best classification for the Zaozigou Au-Sb deposit is as an orogenic gold deposit. The “Au” and “M” orebodies are interpreted to have formed from fault-valve behavior in a transpressional-compressional environment, as commonly seen in global orogenic gold deposits. Previously reported $\delta^{34}\text{S}$ isotope values by proponents of RIRGS (Sui et al., 2020) and orogenic gold (Qiu et al., 2020) are consistent in suggesting a metasedimentary sulfur isotope signature, such as those in metamorphic fluids. The coprecipitation of disseminated arsenopyrite and vein-hosted stibnite has been interpreted to be plausible without invoking thermal gradients. Orebodies and mineralization are observed to be explicitly controlled by faults at Zaozigou. “Au” and “M” orebodies each occur in styles and relationships typically associated with orogenic gold deposits such as high angle reverse faults with associated low angle extensional veins.

1.13 Conclusions

The geology, structure, hydrothermal alteration, and mineralization of the Zaozigou Au-Sb deposit have been described in detail. New mapping and classification of ore-bearing and non-ore-bearing structures at Zaozigou indicates that the deposit formed in stages in response to compressional tectonics first oriented NE-SW, shifting to NW-SW compression later in the geological history. Five significant geological events are identified which are interpreted to be essential to the formation history of the Zaozigou deposit. These events are:

1. Early folding and faulting in response to NE-SW compression, resulting in SE striking fold axes and reverse faults perpendicular to the axis of compression, and NE trending strike-slip faults which are subparallel to the axis of compression.
2. Intrusion of Triassic porphyritic quartz dacite and diorite (andesite) porphyry dikes within many of the NE trending strike slip faults. The dikes contact metamorphosed local sedimentary rocks, marking a transition to brittle deformation.
3. Reactivation of NE trending strike slip faults as steep reverse faults in response to an interpreted change of tectonic stresses to NW-SE compression.
4. Continued cyclical reactivation of structures hosting “Au” style steep fault-fill vein orebodies and “M” shallowly dipping extensional quartz-stibnite veins through interpreted fault-valve pressure cycling behavior.
5. Late brittle faults crosscut earlier structures and orebodies, faulting and dismembering the orebodies.

Constraints on the temperature at the time of syn-tectonic deformation and ore precipitation are interpreted based on the observed microtectonic structures of stibnite (deformation bands, dynamic recrystallization), quartz (subgrain bulging), and calcite (type II

twins) crystals. Together these constraints suggest a ca. 250-300°C temperature range during deformation. Diffusion crack healing of quartz crystals is also presented as evidence that “M” style orebodies experienced multiple pulses of cyclical pressure cycling.

Bulk rock geochemistry data are presented to show that the fault-fill and extensional vein style ore is narrow and high grade in gold up to 56,521 ppb Au. This is contrasted with the disseminated arsenopyrite-pyrite ore, which is lower grade than vein hosted ore, with a maximum analyzed value in altered slate hornfels of 6,431 ppb, and a maximum analyzed value in altered quartz dacite of 7,137 ppb. Bulk rock major oxide geochemistry analyses indicate that the protolith of the local slate hornfels is of shale to greywacke composition. The diorite described in this study geochemically plots as an andesite.

Evaluation of rock samples by SWIR has resulted in the reliable identification of zoned hydrothermal alteration packages. NH₄-illite was newly identified at Zaozigou, and is found only constrained to a 10m altered halo around orebodies. The distal signature of hydrothermal alteration is illite-chlorite. Observation of hydrothermal mineral replacement relationships has shown that (NH₄) illite replacement of iron-rich clay species in slate hornfels, and of biotite, chlorite, and plagioclase in quartz dacites and diorites is the main hydrothermal alteration reaction causing the bleached haloes around orebodies. These bleached haloes are associated with fine grained disseminated arsenopyrite and pyrite occurring as wall rock sulfidation reactions in tandem with bleaching of iron-rich mineral phases.

It is interpreted based on observation of stibnite inclusions within disseminated arsenopyrite in the altered wall rock, that the disseminated arsenopyrite-pyrite and vein- and fault-hosted stibnite could have been precipitated by the same ore fluids. Iron sulfides can easily precipitate from a sulfide ore fluid through wall rock sulfidation of iron-rich mineral phases such

as biotite and chlorite. The controls of stibnite precipitation are not as well understood, but it is believed that precipitation of arsenopyrite and pyrite in alteration haloes in host rocks may have caused desulfidation of the hydrothermal ore fluid, triggering stibnite precipitation. Elevated fluid pressures could have driven fluid-rock interaction using fault and extensional vein rupturing events as fluid conduits.

1.14 Recommendations for future work

This research has highlighted many directions that future work can enhance our understanding of the Zaozigou deposit. Logical continuations of the conclusions and interpretations presented in this research focus on further defining the absolute timing of hydrothermal alteration and mineralization. The geological context established by this research opens new pathways for evaluating the ore deposits of the Xiahe-Hezuo polymetallic zone to further define the structural and tectonic evolution of the region.

Zircon and rutile crystals have been shown to be liberated by illite replacement and sulfidation of biotite crystals in samples of porphyritic quartz dacite. In-situ U-Pb dating of carefully chosen zircons may give insights into the timing of alteration and mineralization at Zaozigou. Additionally Zr in rutile or Ti in zircon thermometry can be attempted to further constrain the temperature of mineralization and alteration.

Vein hosted stibnite crystals from “Au” and “M” style orebodies at Zaozigou have not been analyzed by EPMA, LA-ICP-MS, or micro-XRF to investigate the possibility that stibnite crystals contain refractory gold within the lattice or growth zones. Gold in the quartz-stibnite veins is dominantly observed as free gold in cracks and fractures or spaces between stibnite and quartz crystals. The exceptionally high grades of quartz-stibnite vein samples in this study

suggest that some samples which did not contain observable free gold should likely contain invisible gold locked up in stibnite crystals.

Fluid pressure cycling can be easily confirmed through petrographical analysis of quartz veins from “M” style orebodies using cathodoluminescence to characterize the generations of quartz vein precipitation and diffusion crack healing. Cathodoluminescence applied to these quartz-stibnite veins could also resolve the question of whether quartz precipitation occurred simultaneously with stibnite precipitation or if stibnite simply filled in fractures in quartz veins and crystals.

Very little in-depth mapping of smaller deposits of the Xiahe-Hezuo polymetallic zone has been completed. A cohesive regional scale study of the structural hosts, alteration, and mineralization styles of the deposits hosted in this zone should be completed to define a district-scale framework for this well-endowed, underexplored area. The tectonic regime under which the deposits formed is an essential piece of information that can inform better exploration of the area.

REFERENCES

- Ashley, P.M., Creagh, C.J. and Ryan, C.G., 2000. Invisible gold in ore and mineral concentrates from the Hillgrove gold-antimony deposits, NSW, Australia. *Mineralium Deposita*, 35(4), pp.285-301.
- Bas, M.L., Maitre, R.L., Streckeisen, A., Zanettin, B. and IUGS Subcommittee on the Systematics of Igneous Rocks, 1986. A chemical classification of volcanic rocks based on the total alkali-silica diagram. *Journal of petrology*, 27(3), pp.745-750.
- Bellot, J.P., Bailly, L., Lerouge, C. and Bouchot, V., 2004. Stibnite microstructures as imprints of fault movement. *Mineralium Deposita*, 39(5-6), pp.576-582.
- Boocock, C.N., Cheshire, P.E. and Vearncombe, J.R., 1984. Structural geology of the Gravelotte Shaft Quarry and Monarch antimony mine, Murchison greenstone belt, Transvaal. *South African Journal of Geology*, 87(3), pp.315-325.
- Bortnikov, N.S., Gamynin, G.N., Vikent'eva, O.V., Prokof'ev, V.Y. and Prokop'ev, A.V., 2010. The Sarylakh and Sentachan gold-antimony deposits, Sakha-Yakutia: a case of combined mesothermal gold-quartz and epithermal stibnite ores. *Geology of Ore Deposits*, 52(5), pp.339-372.
- Burkhard, M., 1993. Calcite twins, their geometry, appearance and significance as stress-strain markers and indicators of tectonic regime: a review. *Journal of structural geology*, 15(3-5), pp.351-368.
- Cao, X.F., Sanogo, M.L.S., Lue, X.B., He, M.C., Chen, C., Zhu, J., Tang, R.K., Liu, Z. and Zhang, B., 2012. Ore-Forming Process of the Zaozigou Gold Deposit: Constraints from Geological characteristics, gold occurrence and stable isotope compositions. *Journal of Jilin University (Earth Science Edition)*, 42(4), pp.1039-1054.
- Chang, Z. and Yang, Z., 2012. Evaluation of inter-instrument variations among short wavelength infrared (SWIR) devices. *Economic Geology*, 107(7), pp.1479-1488.
- Chen, G.Z., Wang, J.L., Liang, Z.L., Li, P.B., Zhang, Y.N., and Ma, H.S., 2013. Analysis of Geological structures in Zaozigou gold deposit of Gansu Province. *Gansu Geology*, 22 (4), pp. 50-57. Text in Chinese, English abstract.
- Clark, B.R. and Kelly, W.C., 1973. Sulfide deformation studies; I, experimental deformation of pyrrhotite and sphalerite to 2,000 bars and 500 degrees C. *Economic Geology*, 68(3), pp.332-352.
- Dai W.J., Shi W.Q., Li H.R., Tian X.S., and Yao X.H., 2016. Geological characteristics of the Jiagantan gold deposit and preliminary exploration of its genesis. *Gold*, (2016 01), pp. 18-22. (In Chinese with English abstract).

- Dill, H.G., 1998. Evolution of Sb mineralisation in modern fold belts: a comparison of the Sb mineralisation in the Central Andes (Bolivia) and the Western Carpathians (Slovakia). *Mineralium Deposita*, 33(4), pp.359-378.
- Dou, X.Y., Tian, X.S., Fu, N., Liu, C.X., Shao, X.J., Luo, Y.X. and Liu, L., 2012. Soil geochemistry of Zhihewangan Gold Deposit in West Qinling of Gansu province. *Gansu Geology*, 2.
- Dong, Y.P., Zhou, M.F., Zhang, G.W., Zhou, D.W., Liu, L., Zhang, Q., 2008. The Grenvillian Songshugou ophiolite in the Qinling Mountains, Central China: implications for the tectonic evolution of the Qinling orogenic belt. *Journal of Asian Earth Sciences* 32, 325–335
- Dong, Y., Zhang, G., Neubauer, F., Liu, X., Genser, J. and Hauzenberger, C., 2011. Tectonic evolution of the Qinling orogen, China: review and synthesis. *Journal of Asian Earth Sciences*, 41(3), pp.213-237.
- Ferrari, M., De Angelis, S., De Sanctis, M.C., Ammannito, E., Stefani, S. and Piccioni, G., 2019. Reflectance spectroscopy of ammonium-bearing phyllosilicates. *Icarus*, 321, pp.522-530.
- Godeas, M. and Litvak, V.D., 2006. Identificación de anomalías de amonio por espectrometría de reflectancia: Implicancias para la exploración minera. *Revista de la Asociación Geológica Argentina*, 61(3), pp.438-443. In Spanish with English abstract.
- Goldfarb, R., Baker, T., Dube, B., Groves, D.I., Hart, C.J. and Gosselin, P., 2005. Distribution, character and genesis of gold deposits in metamorphic terranes. *Economic Geology* 100th Anniversary Volume, pp. 407-450.
- Hagemann, S.G. and Lüders, V., 2003. PTX conditions of hydrothermal fluids and precipitation mechanism of stibnite-gold mineralization at the Wiluna lode-gold deposits, Western Australia: conventional and infrared microthermometric constraints. *Mineralium Deposita*, 38(8), pp.936-952.
- Hart, C.J., 2007. Reduced intrusion-related gold systems. *Mineral Deposits of Canada: A synthesis of Major deposit types, district metallogeny, the Evolution of geological provinces, and exploration methods: Geological Association of Canada, Mineral Deposits Division, Special Publication*, 5, pp.95-112.
- Herron, M.M., 1988. Geochemical classification of terrigenous sands and shales from core or log data. *Journal of Sedimentary Research*, 58(5), pp.820-829.
- Ileri, S., 1973. Genesis and fabric study of stibnite ores at the Murchison Range, S.A. Columbia University, Ph.D. Thesis (unpublished).

- Jaguin, J., Boulvais, P., Poujol, M., Bosse, V., Paquette, J.L. and Vilbert, D., 2013. Albitization in the antimony line, Murchison Greenstone Belt (Kaapvaal Craton): A geochemical and geochronological investigation. *Lithos*, 168, pp.124-143.
- Jaguin, J., Boulvais, P., Boiron, M.C., Poujol, M., Gapais, D., Ruffet, G. and Briant, N., 2014. Stable isotopes (O, C) and fluid inclusion study of quartz-carbonate veins from the antimony line, Murchison Greenstone Belt. *American journal of science*, 314(7), pp.1140-1170.
- Jiang, Q. and Wang, R., 2010. Deposit formation environment and genesis of Zaozigou gold deposit in Hezuo, Gansu Province. *Gold Sci. Technol.*, 18, pp.37-40.
- Jin, X.Y., Li, J.W., Hofstra, A.H. and Sui, J.X., 2017. Magmatic-hydrothermal origin of the early Triassic Laodou lode gold deposit in the Xiahe-Hezuo district, West Qinling orogen, China: implications for gold metallogeny. *Mineralium Deposita*, 52(6), pp.883-902.
- Kokaly, R.F., Clark, R.N, Swayze, G.A., Livo, K.E., Hoefen, T.M., Pearson, N.C., Wise, R.A., Benzel, W.M., Lowers, H.A., Driscoll, R.L., and Klein, A.J., 2017. USGS Spectral Library version 7: U.S. Geological Survey Data Series 1035, 61 p., <https://doi.org/10.3133/ds1035>
- Krupp, R.E., 1988. Solubility of stibnite in hydrogen sulfide solutions, speciation, and equilibrium constants, from 25 to 350 C. *Geochimica et Cosmochimica Acta*, 52(12), pp.3005-3015.
- Kuşçu, I. and Erler, A., 1999. Deformation of stibnites and pyrites in the Madsan antimony deposit (Niğde, Turkey): implications for pressure-temperature conditions of local deformation. *Turkish Journal of Earth Sciences*, 8(1), pp.57-66.
- Lang, J.R. and Baker, T., 2001. Intrusion-related gold systems: the present level of understanding. *Mineralium Deposita*, 36(6), pp.477-489.
- Liang ZL, Gong QS, Ma HS, Zhang YN, Chen GZ, Li PB, Wang JL, Cai L, Yang F, Chi HG, Zhao, JZ, Zhao ZC, Zhu R (2016a) Mineral exploration report of Zaozigou gold deposit. 221p (in Chinese).
- Liu, C.X., Li, L. and Sui, J.X., 2011. Mineralization characteristics and ore genesis of the Zaozigou gold deposit, Gansu province. *Geol. Sci. Tech. Inf*, 30(6), pp.66-74.
- Liu, Y., Liu, Y.H., Dong, F., Li, Z.H., Yu, J.K. and Ma, X.P., 2012. Accurate dating of mineralogenetic epoch and its geological significance in Zaozigou gold deposit, Gansu Province. In *Gold* (No. 11, p. 4).
- Mao, X., Zhang, J., Yu, S., Li, Y., Yu, X. and Lu, Z., 2017. Early Paleozoic granulite-facies metamorphism and anatexis in the northern West Qinling orogen: Monazite and zircon U-Pb geochronological constraints. *Science China Earth Sciences*, 60(5), pp.943-957.

- McInnes, B.I., Evans, N.J., Fu, F.Q., Garwin, S., Belousova, E., Griffin, W.L., Bertens, A., Sukarna, D., Permanadewi, S., Andrew, R.L. and Deckart, K., 2005. Thermal history analysis of selected Chilean, Indonesian, and Iranian porphyry Cu-Mo-Au deposits. *Super Porphyry Copper and Gold Deposits: A Global Perspective* (Porter, TM; editor). Porter Geoconsultancy Publishing, de Adelaide, Australia, pp.27-42.
- McQueen, D.R., Kelly, W.C. and Clark, B.R., 1980. Kinematics of experimentally produced deformation bands in stibnite. *Tectonophysics*, 66(1-3), pp.55-81.
- Pochon, A., Gapais, D., Gloaguen, E., Gumiaux, C., Branquet, Y., Cagnard, F. and Martelet, G., 2016. Antimony deposits in the Variscan Armorican belt, a link with mafic intrusives?. *Terra Nova*, 28(2), pp.138-145.
- Pouba, Z., Ilavsky, J., Dunning, F.W. and Evans, M., 1986. Czechoslovakia. *Mineral deposits of Europe*, 3, pp.117-173.
- Qiu, K.F. and Deng, J., 2017. Petrogenesis of granitoids in the Dewulu skarn copper deposit: Implications for the evolution of the Paleotethys ocean and mineralization in Western Qinling, China. *Ore Geology Reviews*, 90, pp.1078-1098.
- Qiu, K.F., Yu, H.C., Deng, J., McIntire, D., Gou, Z.Y., Geng, J.Z., Chang, Z.S., Zhu, R., Li, K.N. and Goldfarb, R., 2020. The giant Zaozigou Au-Sb deposit in West Qinling, China: magmatic-or metamorphic-hydrothermal origin?. *Mineralium Deposita*, pp.1-18.
- Rabbia, O.M. and Hernández, L.B., 2012. Mineral chemistry and potential applications of natural-multi-doped hydrothermal rutile from porphyry copper deposits. *Rutile: Properties, Synthesis and Application*; Low, I.-M., Ed, pp.209-228.
- Sibson, R.H., Robert, F. and Poulsen, K.H., 1988. High-angle reverse faults, fluid-pressure cycling, and mesothermal gold-quartz deposits. *Geology*, 16(6), pp.551-555.
- Sillitoe, R.H., 1994. Erosion and collapse of volcanoes: Causes of telescoping in intrusion-centered ore deposits. *Geology*, 22(10), pp.945-948.
- Silk Road Technical Report <http://www.infomine.com/index/pr/Pa651215.PDF>
- Stipp, M. and Kunze, K., 2008. Dynamic recrystallization near the brittle-plastic transition in naturally and experimentally deformed quartz aggregates. *Tectonophysics*, 448(1-4), pp.77-97.
- Šucha, V., Elsass, F., Eberl, D.D., Madejová, J., Gates, W.P. and Komadel, P., 1998. Hydrothermal synthesis of ammonium illite. *American Mineralogist*, 83(1), pp.58-67.
- Sui, J.X., Li, J.W., Jin, X.Y., Vasconcelos, P. and Zhu, R., 2018. $^{40}\text{Ar}/^{39}\text{Ar}$ and U-Pb

- constraints on the age of the Zaozigou gold deposit, Xiahe-Hezuo district, West Qinling orogen, China: Relation to early Triassic reduced intrusions emplaced during slab rollback. *Ore Geology Reviews*, 101, pp.885-899.
- Sui, J.X., Li, J.W., Hofstra, A.H., O'Brien, H., Lahaye, Y., Yan, D., Li, Z.K. and Jin, X.Y., 2020. Genesis of the Zaozigou gold deposit, West Qinling orogen, China: constraints from sulfide trace element and stable isotope geochemistry. *Ore Geology Reviews*, p.103477.
- Tang, Q., Di, P., Yu, M., Bao, J., Zhao, Y., Liu, D. and Wang, Y., 2019. Mineralogy and Geochemistry of Pyrite and Arsenopyrite from the Zaozigou Gold Deposit in West Qinling Orogenic Belt, Central China: Implications for Ore Genesis. *Resource Geology*, 69(3), pp.314-332.
- Wilson, C.J., Moore, D.H., Luzin, V. and Salvemini, F., 2017. Costerfield antimony-gold deposit, southeast Australia: Coupling between brittle deformation and dissolution-precipitation reactions in the Melbourne Zone. *Ore Geology Reviews*, 91, pp.741-764.
- Vasil'ev, V.I., 2013. Rare graphic textures of cinnabar–stibnite and cinnabar–chalcopyrite pairs and their genesis. *Russian Geology and Geophysics*, 54(11), pp.1385-1391.
- Vearncombe, J.R., 1988. Structure and metamorphism of the Archean Murchison belt, Kaapvaal craton, South Africa. *Tectonics*, 7(4), pp.761-774.
- Voisey, C.R., Tomkins, A.G. and Xing, Y., 2019. The first analysis of a telescoped orogenic gold system. *Crustal-to Nano-Scale Influences on Orogenic Gold Deposits: Insights from the Central Victorian Goldfields*. Doctor of Philosophy thesis. Monash University, Clayton. p.114.
- Voisey, C.R., Willis, D., Tomkins, A.G., Wilson, C.J., Micklethwaite, S., Salvemini, F., Bougoure, J. and Rickard, W.D., 2020. Aseismic Refinement of Orogenic Gold Systems. *Economic Geology*, 115(1), pp.33-50.
- Voisey, C.R., Tomkins, A.G. and Xing, Y., 2020. Analysis of a Telescoped Orogenic Gold System: Insights from the Fosterville Deposit. *Economic Geology*, 115(8), pp.1645-1664.
- Waltham, T., 2002. *Foundations of engineering geology*. CRC Press.
- Yakubchuk, A., Stein, H. and Wilde, A., 2014. Results of pilot Re–Os dating of sulfides from the Sukhoi Log and Olympiada orogenic gold deposits, Russia. *Ore Geology Reviews*, 59, pp.21-28.
- Yan, Z., Fu, C., Aitchison, J.C., Buckman, S., Niu, M. and Cao, B., 2020. Triassic turbidites in the West Qinling Mountains, NW China: Part of the collisional Songpan-Ganzi Basin or an active forearc basin?. *Journal of Asian Earth Sciences*, 194, p.104366.

- Yu, H.C., Guo, C.A., Qiu, K.F., McIntire, D., Jiang, G.P., Gou, Z.Y., Geng, J.Z., Pang, Y., Zhu, R. and Li, N.B., 2019. Geochronological and geochemical constraints on the formation of the giant Zaozigou Au-Sb deposit, West Qinling, China. *Minerals*, 9(1), p.37.
- A Yu, H.C., Qiu, K.F., Nassif, M.T., Geng, J.Z., Sai, S.X., Duo, D.W., Huang, Y.Q. and Wang, J., 2020. Early orogenic gold mineralization event in the West Qinling related to closure of the Paleo-Tethys Ocean—Constraints from the Ludousou gold deposit, central China. *Ore Geology Reviews*, 117, p.103217.
- B Yu, H.C., Qiu, K.F., Sai, S.X., McIntire, D.C., Pirajno, F., Duo, D.W., Miggins, D.P., Wang, J., Jia, R.Y. and Wu, M.Q., 2020. Paleo-tethys late triassic orogenic gold mineralization recorded by the Yidi'nan gold deposit, West Qinling, China. *Ore Geology Reviews*, 116, p.103211.
- Zhai, X., Day, H.W., Hacker, B.R. and You, Z., 1998. Paleozoic metamorphism in the Qinling orogen, Tongbai Mountains, central China. *Geology*, 26(4), pp.371-374.
- Zhou JB (2011) Study on geological characteristics and metallogenic mechanism of the Laodou gold deposit in Gansu province, China. *Gansu Metall* 33:56–60 (In Chinese with English abstract)
- Zhu, Y.N. and Peng, J.T., 2015. Infrared microthermometric and noble gas isotope study of fluid inclusions in ore minerals at the Woxi orogenic Au–Sb–W deposit, western Hunan, South China. *Ore Geology Reviews*, 65, pp.55-69.
- Zotov, A., Mukhamet-Galeev, A. and Schott, J., 1998. An experimental study of kaolinite and dickite relative stability at 150–300 C and the thermodynamic properties of dickite. *American Mineralogist*, 83(5-6), pp.516-524.

APPENDIX A

SUMMARY TABLE OF SIGNIFICANT GLOBAL AU-SB DEPOSITS

Table A.1. (Next Page) Summary Table of significant Global Au-Sb deposits.

Deposit	Costerfield	Fosterville	Wiluna	Chilcobija	Woxi	Zaozigou	Xiangxi	La Lucette, Les Biards	Sarylakh	Sentachan	Olympiada	Dubrava	Monarch-Free State	Alpha-Gravelotte	Stibnite (Yellow Pine)
Country	Australia	Australia	Australia	Bolivia	China	China	China	France	Russia	Russia	Russia	Slovakia	South Africa	South Africa	USA
Province	Melbourne Zone, Victoria	Bendigo Zone, Victoria	Greenstone Belt, Yilgarn Craton	Bolivian Andes	Yangtze meta-platform, Hunan	West Qinling Orogen	Yangtze meta-platform, Hunan	Armorican massif	Yakutia, Verkhoyansk, Kolyma province	Yakutia, Verkhoyansk, Kolyma province	Krasnoyarsk region	Nizke Tatry Mountains	Transvaal, Murchison Range	Transvaal, Murchison Range	Yellow Pine District
Tonnage	1 Moz Au, 260,000t Sb	21.6 Moz Au	3.7 Moz Au, 3.5t Sb	70,000t Sb	1.6 Moz Au, 220,000t Sb, 25,000t W	3.8 Moz Au, 0.12 Mt Sb	0.73 Moz Au, 106,000t Sb	42,000t Sb	21.3 Moz Au, 180,000t Sb	20.6 Moz Au, 110,000t Sb	60 Moz Au	1.18 Mt Sb (E)	1.13 Moz Au, 150,000t Sb (E)	E) 2.6 Moz Au, 270,000t Sb (E)	5 Moz Au, 8 Moz Ag, 92,000t Sb
Grade	>10 g/t Au; 40-50% Cu	5-10 g/t Au, 260 g/t Au	>3 g/t Au	5 g/t Au; 11% Sb	9.7 g/t Au; 2.84% Sb; 0.1% W	5 g/t Au; ~10-20% Cu	13 g/t Au; 6% Sb; 0.1% W	5% Sb	8 g/t Au; 20% Sb	35 g/t Au; 30% Sb	3.5 g/t Au	3 g/t Au; 5% Sb	0.7 g/t Au; 3.1% Sb	0.9 g/t Au; 3.5% Sb	g/t Ag, 0.25% Sb
Host Rocks	Costerfield Siltstone. Lower Silurian elastic meta-sedimentary rocks. High carbonate, organic Carbon content	Castlemaine group: Ordovician turbidites of the Bendigo Zone. Regionally metamorphosed to greenschist facies. Weakly to strongly carbonaceous. Silurian to mid-Devonian aged quartz feldspar porphyry dykes	Metamorphosed mafic-ultramafic volcanic rocks.	Silurian and Ordovician siltstones and slates, interbedded with carbonaceous slates	Proterozoic Lengjiaxi Group sandy slates and phyllites, Banxi Group red slates (Madiyi Formation) interbedded with sandstones	Triassic Gulangdi formation interbedded mudstone and carbonaceous greywacke, triassic quartz dacite porphyry dikes	Proterozoic Lengjiaxi Group sand slates and phyllites, Banxi Group red slates (Madiyi Formation) interbedded with sandstones.	Ordovician to upper Silurian metapelites and sandstones, black shales, spatially associated doleritic dikes	Upper triassic siltstones and sandstones	Upper triassic siltstones and sandy siltstones and interbedded sandstones.	Neproterozoic quartz-mica carbonaceous schists	Late Silurian to Early Carboniferous mylonitized gneissic and granitic rocks	Chlorite phyllite, schistose carbonate, tale schist, chert, siliceous carbonates, mafic-ultramafic volcanics	quartz-sericite/chlorite schists, quartzites, carbonates, mafic-ultramafic volcanics	Cretaceous Idaho Batholith granitoids, Precambrian to Paleozoic metamorphic rocks, quartzite, schist, calc-silicate, marble.
Metamorphic Grade	Greenschist	Greenschist	Sub-greenschist (greenschist-hydrothermal)	Lower Greenschist	Sub-greenschist	Lower Greenschist	Low-grade metamorphic	Greenschist	Greenschist	Greenschist	Greenschist	Medium- to low-grade metamorphism	Greenschist to amphibolite facies	Greenschist to amphibolite facies	Greenschist to amphibolite facies
Structural host	transpressional faults, abundant brittle behavior. Elastic, elastofracture deformation	Saddle reefs, chevron fold hinges, fault zones, S-plays	breccias, cataclastic zones, S-plays	Lode and vein stockworks, saddle reefs	Vein breccias, strata-parallel vein lenses	High angle reverse faults, low angle extensional veins	stratabound	Tension gashes and shear fractures	Anticline, transpressional fault zone	Transpressional fault zone	Anticline folds, boudinage	Shallow-dipping fault zones	Tensional vein fractures, stratabound lenses	Tensional vein fractures	Strike-slip tensional faults
Age	~375 Ma	~380 Ma				<40 Ma, 211 Ma	Yanshanian	310-300 Ma	~140-120 Ma	~140-120 Ma	Inconclusive		2.9 Ga	2.9 Ga	(Previously believed)
Deposit type	Orogenic	Orogenic	Orogenic	Mesothermal	Orogenic?	Orogenic?	meso/epithermal	Orogenic?	Mesothermal?	Mesothermal?	Orogenic	Epithermal	Orogenic	Orogenic	Undetermined
Structure/ setting	transpressional fault system	Bendigo zone fold and thrust belt	Strike-slip fault system	Shear zone	Thrust belt	transpressional fault system	Thrust belt	Brittle strike slip shear zone	Fold-thrust belt	Fold-thrust belt	Fold and thrust belt	Shear zone	Shear Zone	Shear Zone	Orogenic Belt
Ore style	Quartz Lode	quartz-carbonate veins, Disseminated Fe-sulfide	Quartz-stibnite shear veins, disseminated	Quartz-stibnite veins	Banded quartz veins, quartz-stibnite veins,	Quartz-stibnite veins, disseminated	Scheelite-quartz veins, pyrite veins,	Quartz-carbonate-stibnite veins	Quartz-stibnite veins	Quartz-ankerite-stibnite veins	Quartz-carbonate veins	Quartz-stibnite veins	Quartz-carbonate veins	Quartz-carbonate veins	Quartz-stibnite-scheelite veins; auriferous
Ore minerals	stibnite, pyrite, arsenopyrite, sphalerite, gold	stibnite, aurostibite, pyrite, arsenopyrite, gold	Stibnite, arsenopyrite, pyrite	Stibnite, gold	Scheelite, stibnite, pyrite, gold, wolframite, arsenopyrite, sphalerite, galena.	stibnite, arsenopyrite, pyrite, sphalerite	Stibnite, pyrite, scheelite, arsenopyrite, galena, sphalerite, gold	Stibnite, arsenopyrite, gold	stibnite, arsenopyrite, pyrite	stibnite, pyrite, arsenopyrite, sphalerite, galena	Stibnite, pyrite, chalcopryrite, pyrrhotite, sphalerite, scheelite	Stibnite, pyrite, arsenopyrite, sphalerite, chalcopryrite, sulfosalts, gold	Stibnite, berthierite, pyrite, arsenopyrite	Stibnite, berthierite, arsenopyrite	Stibnite, scheelite, pyrite, arsenopyrite
Alteration	carbonate	sericite (illite, muscovite), carbonate, kaolinite	chlorite, carbonate (calciteankerite siderite),	kaolinite, calcite,	Sericite, carbonate, chlorite	carbonate, silicification, kaolinite	Sericite, silicification, carbonate, chlorite,	Sericite, carbonate	sericite, carbonate, sulfidation	sericite, sulfidation	Sericite, carbonate	Siderite	Albite, carbonate	Albite, carbonate	Sericite, Potassium metasomatism,
Au occurrence	Free gold, refractory in Fe-sulfides	Free gold, refractory in Fe-sulfides, Au adsorbed onto	Free gold, refractory in Fe-sulfides	Free gold, refractory in Fe-sulfides	Free gold, refractory in Fe-sulfides	Free gold, refractory in Fe-sulfides	Free gold, refractory in Fe-sulfides	Free gold, refractory in Fe-sulfides	Free gold, refractory in Fe-sulfides	Free gold, refractory in Fe-sulfides	Free gold, refractory in Fe-sulfides	Free gold, refractory in Fe-sulfides	Free gold, refractory in Fe-sulfides	Free gold, refractory in Fe-sulfides	Free gold, refractory in Fe-sulfides
Fluid characteristics	180-230C, Moderate salinity (<10wt %NaCl eq.), near neutral pH, CO-H-N high N2	180-270C	286±25C, 0.2-8.8 wt%NaCl eq. H2O-CO2-CH4 aqueous carbonic fluids,	<270C, 234-150C, CO2-CH4-N2 aqueous fluids	140-240C, <7.0 wt% NaCl eq. H2O-CO2-N2 aqueous carbonic fluids	Aqueous-carbonic	~230C, Low Cl, high HS-, Near-neutral pH	200-270C, <9 wt% NaCl eq. 618Quartz = 8.5-10.7% CO2-CH4-H2O aqueous fluids	Free gold, refractory in Fe-sulfides 253-318C, <8 wt%NaCl eq. Carbonic-aqueous-CH4 fluids.	232-340C, <10 wt% NaCl eq. Carbonic-aqueous-CH4 fluids. H2O-CO2-CH4-H2S-NaCl, CO2, CH4, H2S, H2, and NH3 volatiles	H2O-CO2-CH4-N2 aqueous carbonic fluids.	<153-238C, <7 wt% NaCl eq. CO2-CH4-N2 aqueous fluids	350-450C, <16.7 wt% NaCl eq. 618Quartz = 10.9-14.3% H2O-CO2-CH4-N2	350-450C, <16.7 wt% NaCl eq. 618Quartz = 10.9-14.3% H2O-CO2-CH4-N2 aqueous carbonic fluids.	<4001 to 180C for gold, <180 C for stibnite. 618Quartz = 6-9 wt%NaCl, H2O-CO2-CH4-N2 aqueous carbonic fluids.
Citation	Wilson et al., (2017)	Voisey et al., (2019); Voisey et al., (2020)	Hagemann & Laders, (2003)	Dill (1998)	Zhu & Peng, (2015)	Sui et al., (2018); Yue et al., (2019); Qiu et al., (2020)	Yang & Blum, (1999)	Pochonet et al., (2016)	Bortnikov et al., (2010)	Bortnikov et al., (2010)	Yakubchuk et al., (2014)	Dill (1998); Poubá and Ilavský, (1986)	Boocock et al., (1984); Vearnecombe, (1988); Jaguin et al., (2013); Jaguin et al., (2014)	Boocock et al., (1984); Vearnecombe, (1988); Jaguin et al., (2013); Jaguin et al., (2014)	Wntzer (2019); Lewis (1984); Perpetua Resources NI-43 101 (2021)

APPENDIX B

SUPPLEMENTAL ELECTRONIC FILES

The included supplemental file is an Excel spreadsheet of mineral interpretations. Interpretations were made based on spectra collected by an ASD Terraspec SWIR spectrometer.

SWIR-Table.xlsx

APPENDIX C

STIBNITE SOLUBILITY AND AQUEOUS SPECIATION

C.1 Gold-Antimony deposits

Gold-Antimony deposits occur in many countries and continents in rocks of varying lithologies and geologic ages. Au-Sb or Sb-Au deposits are here defined as deposits which host economic concentrations of Au and Sb, where Au and Sb are present in significant enough concentrations to be extracted as primary commodities or as byproducts, i.e. gold deposits with trace Sb concentrations and Sb deposits with no/low Au (notably the Sb-only Xikuangshan deposit, Hunan, China) are excluded. The most significant and well-studied deposits are found in China, Russia, South Africa, Australia, Bolivia, New Zealand, Slovakia, and France, and are described in Appendix A. These deposits most commonly occur as quartz-stibnite±carbonate veins hosted by sub-greenschist to greenschist facies regionally metamorphosed sequences. Deposits of the South African antimony line are a notable exception, being found in upper greenschist to amphibolite facies. Globally, Au-Sb deposits have significant grade variation. The mines of the Monarch-Free State district in South Africa average around 0.7 g/t Au and 3.1% Sb (Boocock et al., 1984; Vearnecombe, 1988; Jaguin et al., 2013; Jaguin et al., 2014), whereas the Sentachan deposit in Russia hosts ore at 35 g/t Au and 30% Sb (Bortnikov et al., 2010).

Host rocks of significant Au-Sb deposits are highly variable. Many large deposits are hosted in carbonaceous meta-sedimentary sequences. Costerfield (Wilson et al., 2017), Fosterville (Voisey et al., 2019; Voisey et al., 2020), Chilcobija (Dill, 1998), Zaozigou (Sui et al., 2018; Yu et al., 2019; Qiu et al., 2020), Olympiada (Yakubchuk et al., 2014), Monarch-Free State and Alpha-Gravelotte (Boocock et al., 1984; Vearnecombe, 1988; Jaguin et al., 2013; Jaguin et al., 2014) are at least partially hosted by Carbon-rich or carbonaceous metasediments.

The Woxi and Xiangxi deposits in Hunan, China are notably hosted by red slates of the Madiyi Formation (Yang and Blum, 1999; Zhu and Peng, 2015). This suggests that fluid-rock redox reactions may play an important role in the precipitation of antimony minerals. Volcanic or intrusive igneous rocks can be found at most significant Au-Sb deposits. These range in composition from felsic, such as the quartz feldspar porphyry dikes at Fosterville (Voisey et al., 2019; Voisey et al., 2020) to the intermediate intermediate quartz dacite and diorite dikes at Zaozigou (Sui et al., 2018; Yu et al., 2019; Qiu et al., 2020), to the mafic-ultramafic volcanics which host deposits of the South African antimony line (Boocock et al., 1984; Vearnecombe, 1988; Jaguin et al., 2013; Jaguin et al., 2014).

Stibnite (Sb_2S_3) is globally the most important ore mineral in Au-Sb deposits, however in some localities, aurostibite (AuSb_2), berthierite (FeSb_2S_4), stibiconite ($\text{Sb}_3\text{O}_6[\text{OH}]$), Sb-tellurides, Sb-selenides, sulfosalts and other, less common Fe, Cu, Ag, Pb, Tl, Hg, As, Bi, and Sb-oxide minerals are found but are typically accessory minerals of little economic importance.

Gold typically occurs as free gold within quartz-stibnite veins, or as refractory gold within Fe-sulfides, arsenopyrite and pyrite being the most common hosts. Arsenopyrite and pyrite are found in veins and/or wall rock alteration haloes at every significant global Au-Sb deposit except Chilcobija.

Hydrothermal alteration assemblages most commonly contain carbonate (calcite, dolomite, ankerite) and at least one sericite species (illite and muscovite most common). Chlorite, albite, and fuchsite are common depending on the host rock composition. Sulfidation, found as disseminated arsenopyrite and pyrite, commonly replacing biotite, chlorite, and mafic minerals, is an important source of Au. The Hillgrove gold-antimony deposits in Australia produce ~50-55% of their Au from invisible gold in arsenopyrite and pyrite (Ashley et al., 2000).

Gold-Antimony ores are structurally hosted. Quartz-stibnite veins and lenses are found in saddle reefs, transpressional faults, fault breccias, shear veins, stockwork veins, stratabound lenses, tension gashes, and other features. It is highly uncommon in large deposits for stibnite to precipitate in wall rock alteration assemblages. Deposits are found dominantly in convergent tectonic regimes along craton boundaries and active subduction zones.

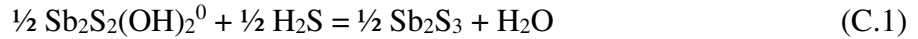
Fluid inclusion studies indicate a range in temperatures of precipitation, but typically range in temperature from ~200-300°C. Inclusions are typically low to moderate salinity (<10 wt% NaCl eq.). Fluids are aqueous-carbonic, and often have minor to major CH₄, and minor N₂ or NH₃ volatiles. The South African antimony line deposits are notably different. Jaguin et al., (2014) measured fluid inclusions in quartz-carbonate veins interpreted to have precipitated at 350-450° and 200-300 MPa. Fluids were higher salinity (<16.7 wt% NaCl eq.) and were of H₂O-CO₂-CH₄-N₂ composition. Stable Oxygen isotopes at La Lucette and the Murchison Greenstone Belt antimony line have yielded δ¹⁸O values of 8.5-10.7 ‰ and 10.9-14.3 ‰, respectively (Jaguin et al., 2014; Pochon et al., 2016). This has been used to interpret metamorphic fluids as the main fluid source in these deposits.

Most large Au-Sb deposits globally have been interpreted as orogenic or mesothermal deposits, depending on the date studied. The Xiangxi and Dubrava deposits are argued to be epithermal (Pouba and Ilavsky 1986; Yang and Blum 1999).

C.2 Antimony Geochemistry

Antimony is transported in hydrothermal fluids as thioantimonite complexes (H₂Sb₂S₄⁰, HSb₂S₄⁻, and Sb₂S₄²⁻, or as hydroxothioantimonite species (Sb₂S₂[OH]₂⁰). The Sb-speciation and solubility in hydrothermal fluids has been shown to be strongly controlled temperature and pH conditions (Krupp, 1988). Typical geological conditions for the mineralization of Au-Sb deposits

are ca. 150-350 degrees C, and slightly acidic to neutral pH (~5.5-6.5). Under these conditions, the dominant Sb- species in hydrothermal fluids has been calculated thermodynamically to be hydroxothioantimonites of the general formula $\text{Sb}_2\text{S}_2(\text{OH})_2^0$. Precipitation of stibnite from these hydrothermal fluids can trigger the precipitation of free Gold by the destabilization of $\text{Au}(\text{HS})_2^-$ complexes following the paired reaction:



Wherein H_2S is scavenged from gold bisulfide complexes and incorporated into stibnite. Thus, the precipitation of stibnite from a hydrothermal fluid can trigger free gold precipitation. This reaction requires an additional process to initiate stibnite precipitation from a hydrothermal fluid. Hagemann & Luders, (2003) studied stibnite-gold mineralization at the Wiluna deposits in Western Australia. Their thermodynamic modelling of P-T-X conditions of stibnite precipitation suggest that, where hydroxanthimonite is the dominant Sb fluid compound, the most efficient control on stibnite precipitation would be a decrease in temperature of the hydrothermal fluid. They found that a 50° C decrease would result in a stibnite fluid solubility decrease of one order of magnitude (i.e. Figure path 1-7, 3-8). However, they also suggest that, if the dominant Sb species is thioantimonite ($\text{H}_2\text{Sb}_2\text{S}_4$), then stibnite solubility would decrease following a decrease in $a_{\text{H}_2\text{S}}$, as shown by the following equation presented in Krupp (1988):



Thioantimonite has been shown thermodynamically to be the dominant Sb species in hydrothermal fluids at ~300-200° C, pH of 5.5 and $\log a_{\text{H}_2\text{S}} > \text{ca. } -2$ (Figure , Krupp, 1988, Hagemann & Luders, 2003). However, as $a_{\text{H}_2\text{S}}$ decreases, hydroxothioantimonite becomes the dominant Sb fluid species, and further decrease of $a_{\text{H}_2\text{S}}$ would result in increased Sb solubility

within the hydrothermal fluid as indicated in Equation C.1 (Figure path from point 4 through 1). Figure illustrates the effects of changing fluid conditions and Sb speciation on the aqueous Sb solubility in hydrothermal fluids. This presents multiple methods by which stibnite can precipitate and co-precipitate with gold in ore systems. Probably the most common method for precipitation of stibnite is a decrease in temperature. In magmatic-hydrothermal systems, thermal gradients are likely an important method triggering Au-Sb mineralization. However, in meso- to epizonal orogenic deposits, thermal gradients are not as pronounced (Goldfarb et al., 2005). Hagemann & Luders (2003) suggest that cooling related to adiabatic decompression, especially in extensional veins (eg. Sibson et al., 1988) could also trigger Au-Sb mineralization. An alternative method of precipitating stibnite, especially where $\text{H}_2\text{Sb}_2\text{S}_4$ is the dominant Sb aqueous phase, is wall rock sulfidation. Au-Sb deposits' common association with wall rock pyrite and arsenopyrite in wall rock alteration haloes could represent a decrease in hydrothermal fluid aH_2S . Phase separation i.e. boiling may also represent a mechanism to precipitate stibnite and free gold. The Hagemann & Luders (2003) model does not account for variations in REDOX condition. With Au-Sb deposits' common occurrence in (metamorphosed) sedimentary terranes, it is conceivable that reduction from wall rock interaction of organic carbonaceous or graphitic sediments may also present an effective precipitation mechanism.

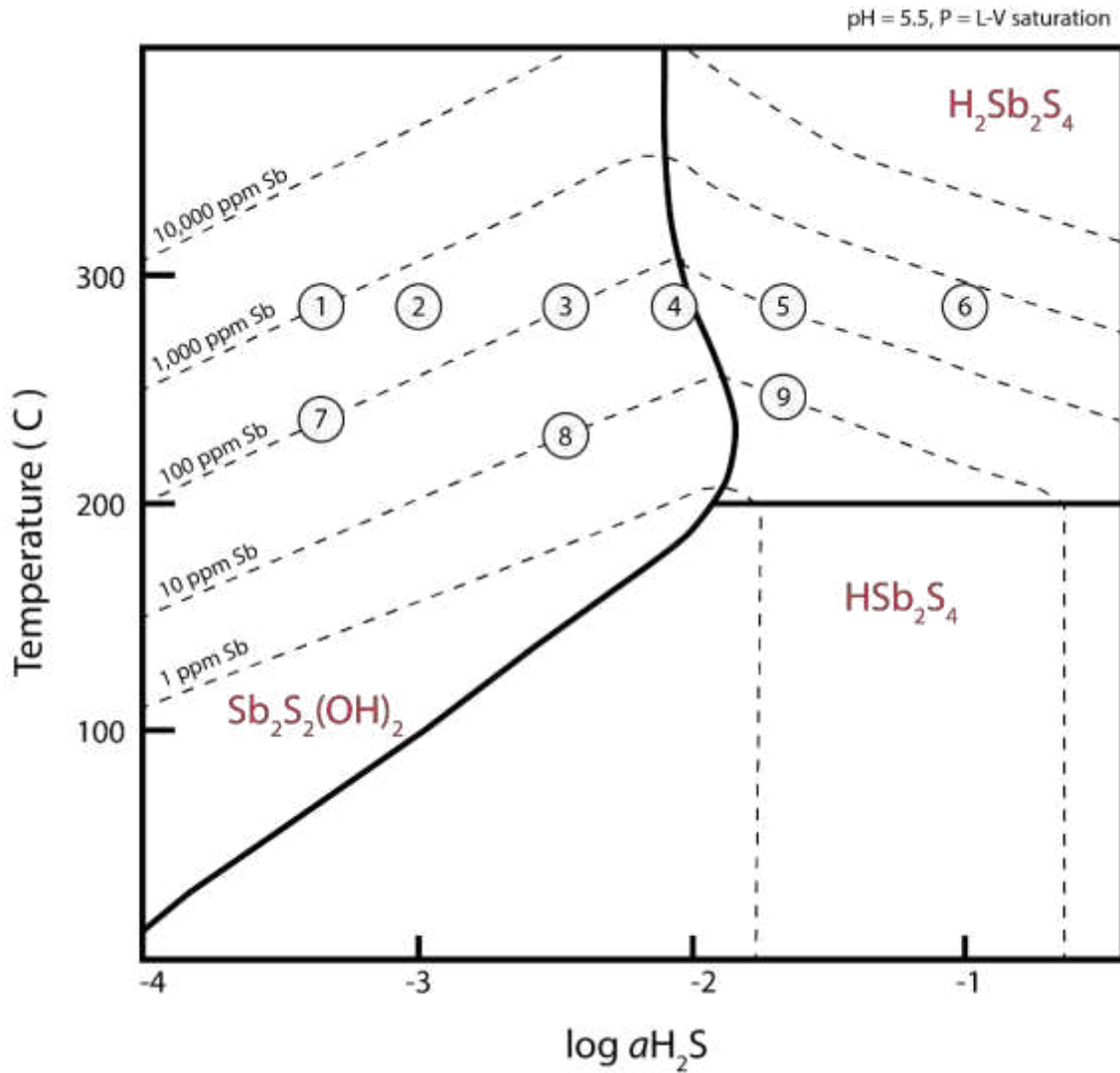


Figure C.1. Phase diagram of aqueous Sb species in hydrothermal fluids with superimposed Sb fluid solubility contours. Bold lines indicate boundaries between aqueous Sb species. Circled numbers indicate hypothetical points for illustrating fluid property changes. Modified from Hagemann & Luders (2003).

APPENDIX D

STRUCTURAL CROSS SECTIONS

No vertical exaggeration. Constructed using apparent dip. Orebody thicknesses not to scale.

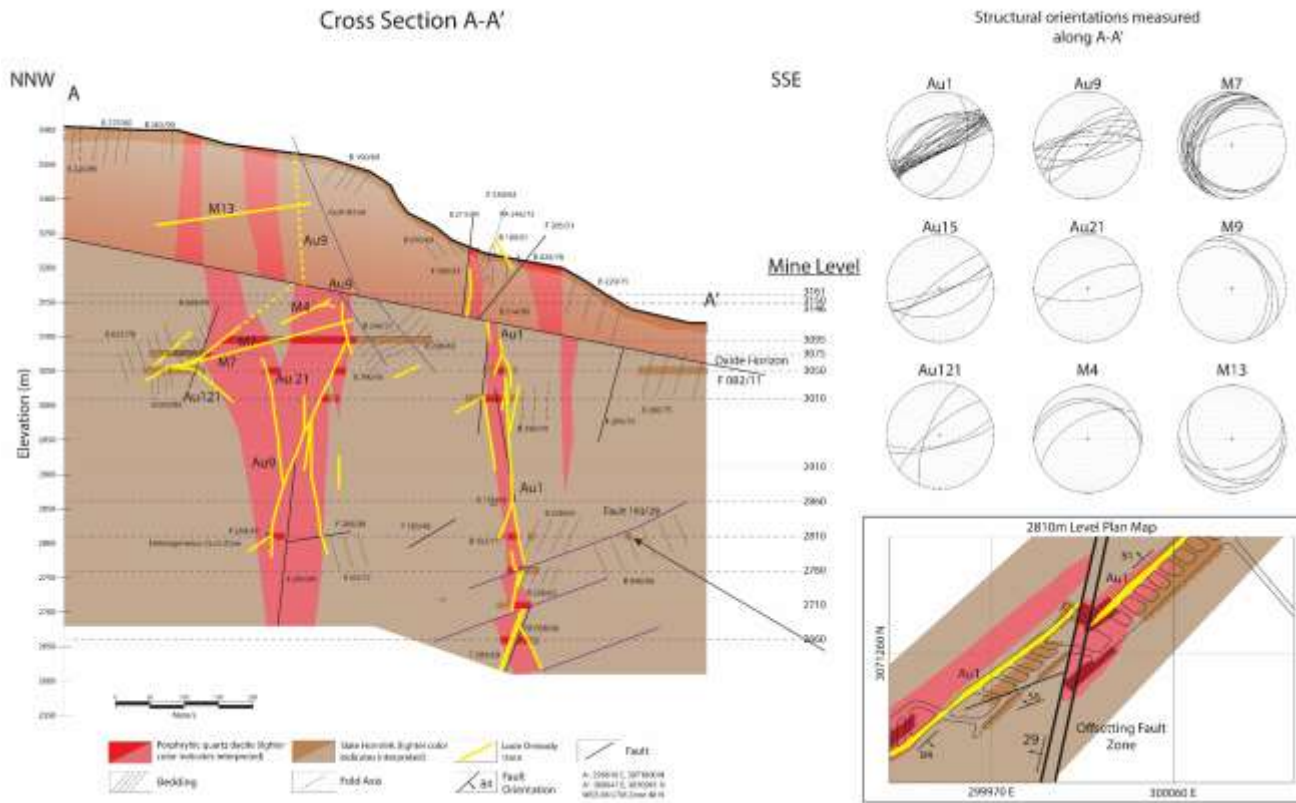


Figure D.1. Cross Section A-A'.

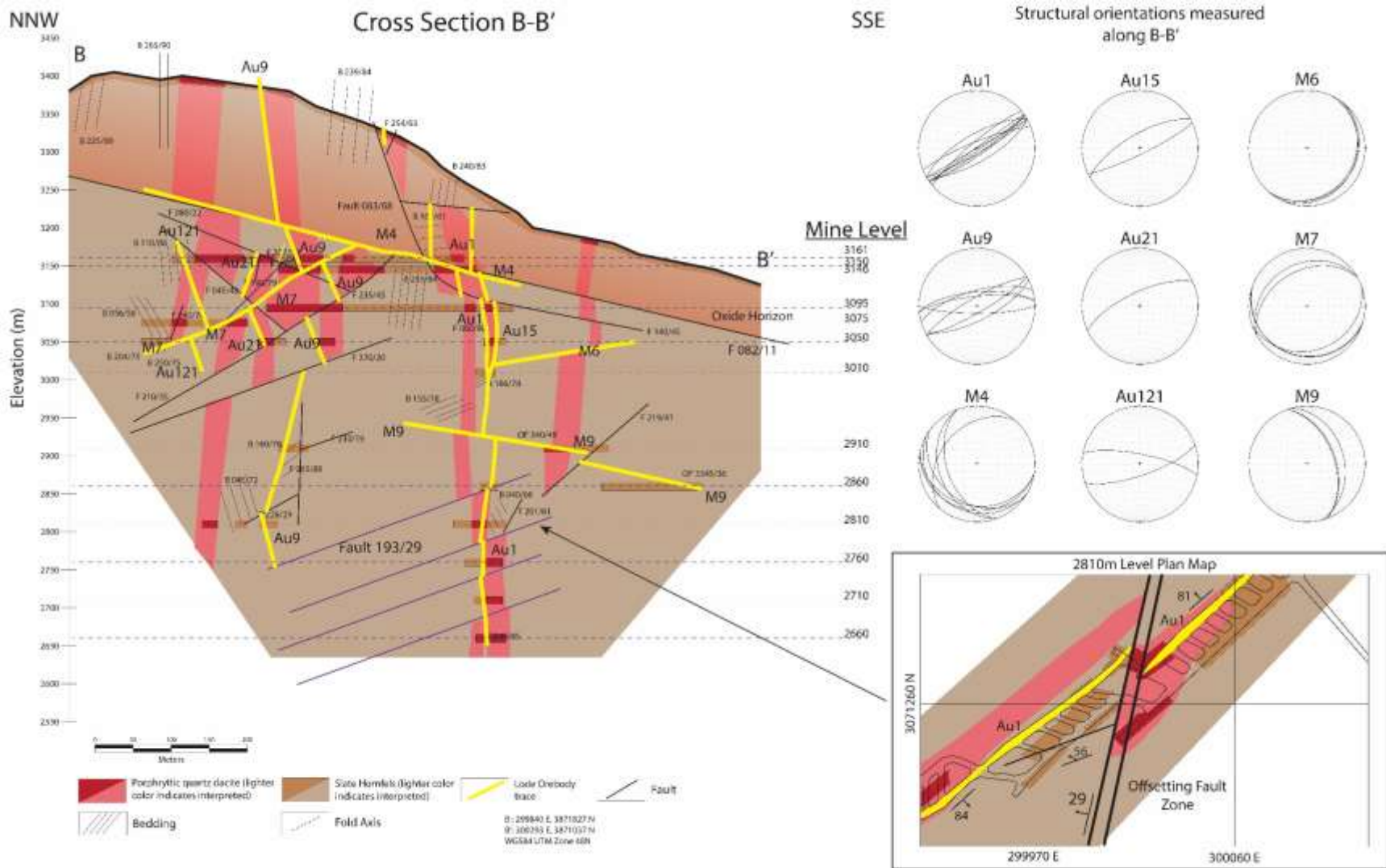


Figure D.2. Cross Section B-B'.

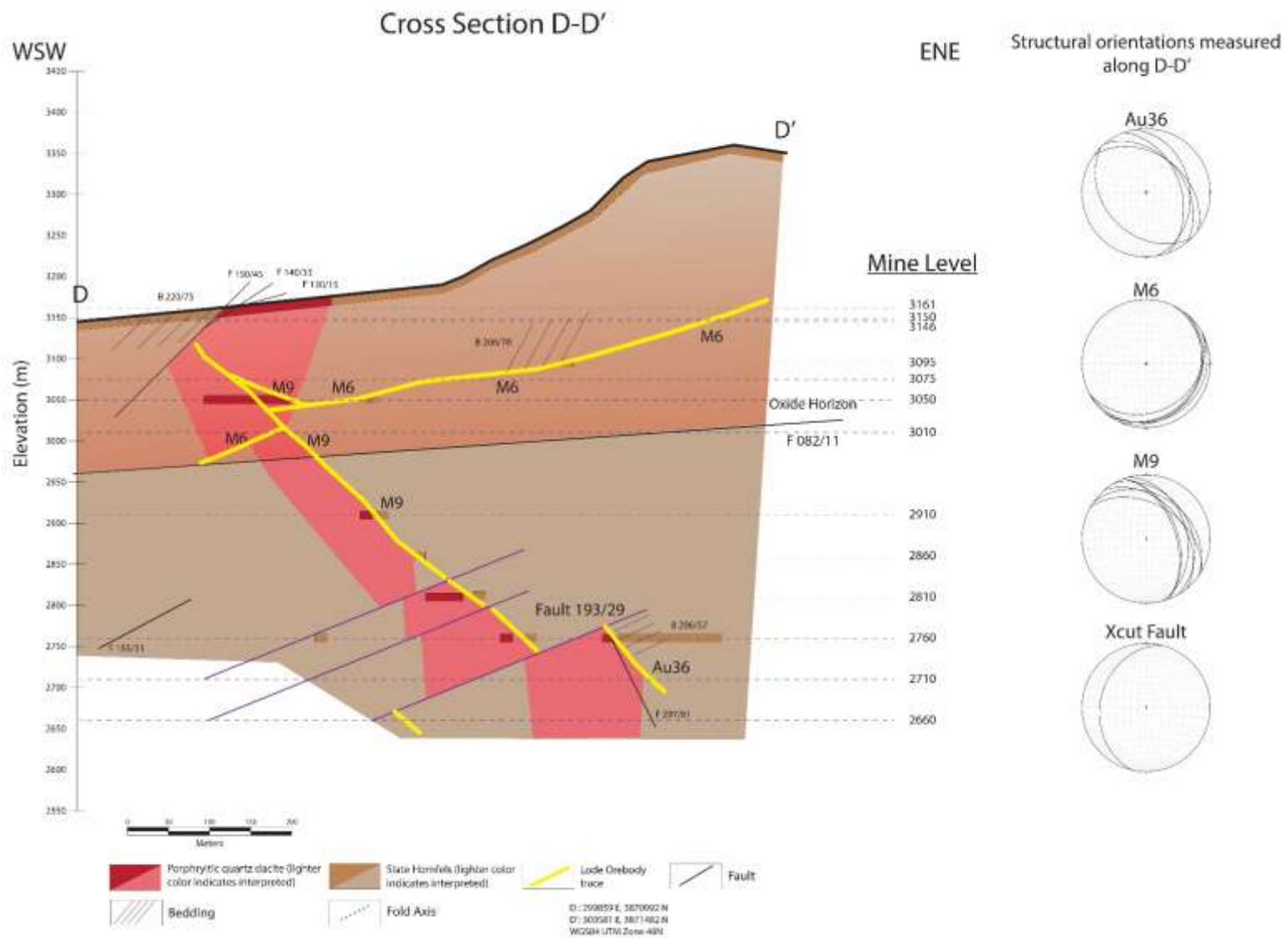


Figure D.3. Cross Section D-D'.

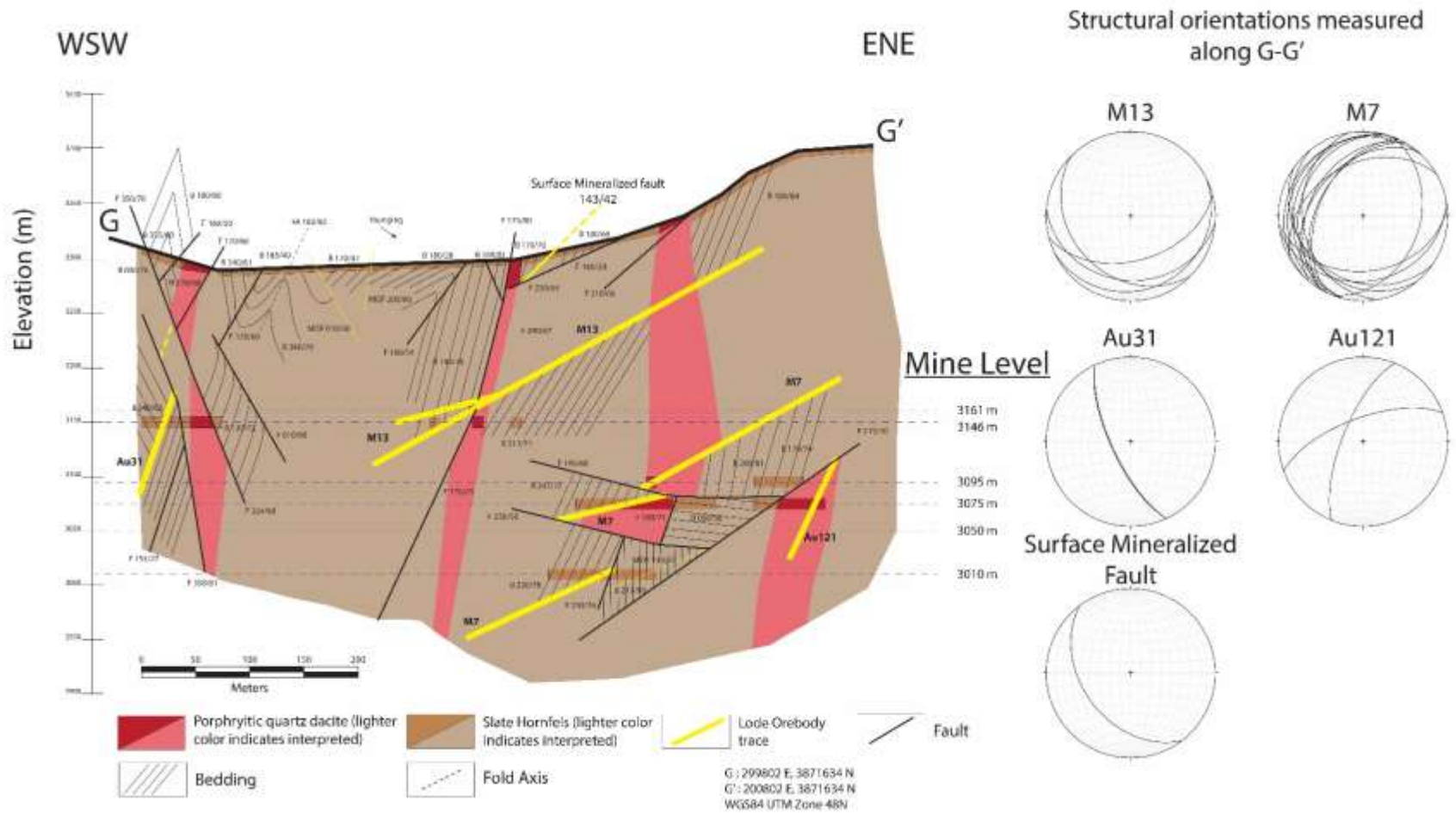


Figure D.4. Cross Section G-G'.

APPENDIX E

ANALYTICAL METHODS

E.1 Analytical Methods

The objectives of this research were to 1.) characterize the structural evolution of the Zaozigou deposit, and 2.) to evaluate the role that the structural evolution of the Zaozigou deposit played in the development of ore and hydrothermal alteration. Characterization of the structural evolution of Zaozigou is based on the new mapping of surficial geology and 13 underground mine levels. Relative timing relationships of intrusions and structures were observed. Effort was made to link structures between underground levels and surface outcrops. Structural measurements, rock units, and orebodies have been plotted on maps and cross sections. Relative timing relationships are used to constrain the timing of structural events where possible. The role that the structural evolution of the Zaozigou deposit played in the development of ore and hydrothermal alteration was evaluated in stages. With a model for the structural evolution of Zaozigou in place, it is necessary to show how that structure controlled the style and dimensions of mineralization and hydrothermal alteration. The first step is to characterize the styles of alteration and mineralization at Zaozigou. A first pass interpretation of hydrothermal alteration and mineralization styles was made in the field during mapping activities. The understanding of hydrothermal alteration was further refined through the application of shortwave infrared spectrometry (SWIR) data collected using an ASD Terraspec. Samples were collected systematically in transits across veins and fault-hosted orebodies to evaluate the spatial variation of hydrothermal alteration species. Locations of all samples collected during field work and their respective distances to the nearest proximal orebody were recorded. Samples were selected for petrographical work based on representivity. Petrography included observation with

plane polarized, cross polarized, and reflected light. Mineral relationships and microtectonic indicators were the priority of petrographic observation. Based on observed petrography, samples were later selected for bulk rock geochemistry. Samples analyzed included altered and unaltered quartz dacite, diorite, slate hornfels, and unaltered slate and also included ores from “Au” and “M” style orebodies and their alteration haloes. Bulk rock geochemistry was used to further define the petrology of the lithologies found at Zaozigou, to define a distance-grade relationship of disseminated ore in wall rock and define expected grades for different ore styles at Zaozigou. Observation by FE-SEM, EDS, and QEMSCAN further defined mineral replacement and timing relationships. After bulk rock geochemical analytical results returned high gold values for some samples which did not have observable gold in thin section under petrographic microscope or FE-SEM, crude attempts were made to evaluate whether the samples contained coarse free gold. These samples with high gold analyses were crushed using a mortar and pestle and the crushed material was panned by hand. Gold grains were successfully liberated and observed using this method.

Over 120 individual rock samples were collected on site at surface and in the active underground mine at Zaozigou. Comprehensive structural, lithological, and alteration mapping was conducted over a 1.8 km² quadrangle at the surface, and across 13 underground levels. Special attention was paid to the vertical continuity of structures between levels of the underground mine and at surface. Samples were selected to be representative of the lithologies, orebodies, styles and intensities of hydrothermal alteration associated with ore.

Mapping was conducted using a Brunton-style transit compass clinometer. All measurements reported follow right-hand rule strike and dip conventions i.e. a strike of 180° corresponds to a dip azimuth of 270°, and a strike of 330° corresponds to a dip azimuth of 60°.

Where safety concerns and access limitations prohibited direct measurement of geological features, the geometries of these features were estimated using standard field practices. All maps presented here use the World Geodetic System of 1984 (WGS84) UTM zone 48 North (EPSG:32468). Maps and data provided by Zhaojin Gold Company were originally in the New Beijing / 3-degree Gauss-Kruger zone 34 projection (EPSG:4770). These have been projected to WGS84 zone 48 N. The magnetic declination at Zaozigou is 2° W.

E.2 Bulk Rock Geochemistry

From the 120+ samples collected, 31 representative samples were chosen for bulk rock geochemical analysis by ICP-MS/ICP-ES, and LECO. Samples of minimum 100g were sent to Bureau Veritas in Vancouver, BC for 70 element analysis including major oxides, LOI, total carbon, and total sulfur. Five combinations of sample digestion and analysis were performed on the selected samples. Major oxides, LOI, C, and S analysis was performed using an initial Li borate fusion with ICP-ES finish. Ba, CS, Ga, Hf, Nb, Rb, Sn, Sr, Ta, Ta, Th, U, V, W, Y, and REE were analyzed using a Li borate fusion and ICP-MS finish. Ag, As, B, Be, Bi, Cd, Co, Cr, Cu, Cu, Ge, Hg, In, Li, Mn, Mo, Ni, Pb, Pd, Pt, Re, Sb, Se, Te, Tl, and Zn were analyzed using an Aqua regia digestion with an ICP-MS finish. Ni was additionally analyzed using a 4-acid digestion and ICP-ES finish. Au, Pd, Pt were analyzed by Pb collection fire assay with an ICP-MS finish. Samples with Au analysis over 10 ppm were re-analyzed by Pb collection fire assay with a gravimetric finish.

The samples chosen were two unaltered slate samples, individual samples of unaltered quartz dacite dike and diorite dike, five samples of Au1 vein ore, three samples of Au1-proximal altered quartz dacite, two samples of Au1-proximal altered slate hornfels, three samples of Au9 vein ore, one sample of Au9-proximal altered quartz dacite, four samples of Au9-proximal

altered slate hornfels, one sample of M9 vein breccia ore, one sample of M9-proximal altered quartz dacite, two samples of M9-proximal altered slate hornfels, and four samples from a surface ore outcropping discovery of which two samples are ore vein, and two samples are proximal altered slate hornfels.

The results of the analyses are reported in Table 1.1. Six samples exceeded the upper quantifiable limit for As analysis (10,000 ppm). Seven samples exceeded the upper quantifiable limit for Sb analysis (2000 ppm).

E.3 Shortwave Infrared (SWIR) spectrometry

All samples collected were analyzed using an ASD Terraspec 4 Hi-Res mineral analyzer (model TSP 350-2500), operated using ASD RS³ software package. Sample spectra were analyzed and interpreted to identify key alteration minerals in the deposit. Due to the extremely fine grain size of clay and sericite alteration minerals, SWIR spectrometry is an ideal method for acquiring quick and accurate alteration mineralogy reports. Very little sample preparation is required and analysis is inexpensive. SWIR is less useful for dark-colored minerals and minerals without OH hydroxyl groups. The Terraspec 4 measures visible near-infrared (VNIR) and short-wave infrared spectra in the following wavelengths:

VNIR-SWIR1-SWIR2: 350-2500 nm

SWIR1-SWIR2: 1000-2500 nm

SWIR2 only: 1800-2500 nm

Analyzed samples were first washed with tap water and scrubbed with a stiff nylon bristled brush and left to air dry 12 hours prior to analysis. Prior to sample analysis, the instrument is optimized using a standard white reference plate. During sampling, the instrument is recalibrated approx. every 30 minutes to maintain quality analysis. Due to the small spot size

of the analyzer, each sample was analyzed three times in different locations, ignoring all vein features where possible in order to ensure accurate measurement of zones of hydrothermal alteration. As SWIR spectrometry depends on the reflectance of analyzed material, it is necessary to analyze dark colored samples longer than light colored samples. Dark colored samples were analyzed using a 200-count measurement. Light colored samples were analyzed using a 30-count measurement, as recommended by Chang and Yang (2012). Analyzed spectra were exported to The Spectral Geologist™ software for interpretation of mineral species. Interpreted results of SWIR analysis are shown in Appendix 2.

E.4 Petrography, FE-SEM and QEMSCAN

Sixty samples were cut to make standard 30 µm polished thin sections at the Colorado School of Mines thin section lab. Samples were prepared and cut oblique to important geological features such as veins, bedding, and foliation so that movement sense indicators, mineral zonation patterns, and alteration profiles could be observed. Transmitted and reflected light petrography was performed on these samples prior to 10 samples being carbon coated for analysis on a field emission scanning electron microscope (FE-SEM).

Five ore vein samples (ZZG18-010, ZZG18-041, ZZG18-048, ZZG18-056, ZZG18-057, ZZG18-070) were chosen for analysis at Colorado School of Mines automated mineralogy lab using Field Emission Scanning Electron Microscopy (FE-SEM) and Quantitative Evaluation of Materials by Scanning Electron Microscope (QEMSCAN). QEMSCAN is a method of automated mineralogy using a TESCAN Integrated Mineral Analyzer (TIMA) equipped with a backscattered electron (BSE) detector and 4 energy dispersive X-ray spectrometers (EDS).

E.5 Hand-panning crushed samples

Three ore vein samples (ZZG18-041, ZZG18-055, ZZG18-057) with high Au results greater than 10 ppm were crushed using a steel mortar and pestle and were panned unclassified in a standard gold pan. Stibnite has a density of 4.63 g/cm^3 . Native gold has a density of 19.3 g/cm^3 . Gold panning is a quick, effective, inexpensive method of determining whether samples contain gold as free gold. Gold is significantly denser than any gangue minerals or sulfide ore minerals present in the samples.

Cursory hand-panning of selected samples which returned high Au values in bulk rock geochemistry resulted in the liberation of observable, fine-grained visible gold.



Figure E.1. Observable gold grains in hand-panned high-grade Au-Sb ore. Pictured is sample ZZG18-057 as viewed through binocular microscope. Approx. 40x magnification.